High Energy Studies of Astrophysical Dust

Lia Racquel Corrales

Submitted in partial fulfillment of the
requirements for the degree
of Doctor of Philosophy
in the Graduate School of Arts and Sciences

COLUMBIA UNIVERSITY

2015

ABSTRACT

High Energy Studies of Astrophysical Dust

Lia Racquel Corrales

Astrophysical dust – any condensed matter ranging from tens of atoms to micron sized grains – accounts for about one third of the heavy elements produced in stars and disseminated into space. These tiny pollutants are responsible for producing the mottled appearance in the spray of light we call the "Milky Way". However these seemingly inert particles play a strong role in the physics of the interstellar medium, aiding star and planet formation, and perhaps helping to guide galaxy evolution. Most dust grains are transparent to X-ray light, leaving a signature of atomic absorption, but also scattering the light over small angles. Bright X-ray objects serendipitously situated behind large columns of dust and gas provide a unique opportunity to study the dust along the line of sight. I focus primarily on X-ray scattering through dust, which produces a diffuse halo image around a central point source. Such objects have been observed around X-ray bright Galactic binaries and extragalactic objects that happen to shine through the plane of the Milky Way.

I use the *Chandra* X-ray Observatory, a space-based laboratory operated by NASA, which has imaging resolution ideal for studying X-ray scattering halos. I examine several bright X-ray objects with dust-free sight lines to test their viability as templates and develop a parametric model for the *Chandra* HETG point spread function (PSF). The PSF

describes the instrument's imaging response to a point source, an understanding of which is necessary for properly measuring the surface brightness of X-ray scattering halos. I use an HETG observation of Cygnus X-3, one of the brightest objects available in the *Chandra* archive, to derive a dust grain size distribution. There exist degenerate solutions for the dust scattering halo, but with the aid of Bayesian analytics I am able to apply prior knowledge about the Cyg X-3 sight line to measure the relative abundance of dust in intervening Milky Way spiral arms. I also demonstrate how information from a single scattering halo can be used in conjunction with X-ray spectroscopy to directly measure the dust-to-gas mass ratio, laying the ground work for future scattering halo surveys.

Distant quasars also produce X-rays that pierce the intergalactic medium. These sources invite the unique opportunity to search for extragalactic dust, whether distributed diffusely throughout intergalactic space, surrounding other galaxies, or occupying reservoirs of cool intergalactic gas. I review X-ray scattering in a cosmological context, examining the range and sensitivity of *Chandra* to detect the low surface brightness levels of intergalactic scattering. Of particular interest is large 'grey' dust, which would cause systematic errors in precision cosmology experiments at a level comparable to the size of the error bars sought. This requires using the more exact Mie scattering treatment, which reduces the scattering cross-section for soft X-rays by a factor of about ten, compared to the Rayleigh-Gans approximation used for interstellar X-ray scattering studies. This allows me to relax the limit on intergalactic dust imposed by previous X-ray imaging of a $z = 4.3$ quasar, QSO 1508+5714, which overestimated the scattering intensity.

After implementing the Mie solution with the cosmological integral for scattering halo

intensity, I found that intergalactic dust will scatter 1-3% of soft X-ray light. Unfortunately the wings of the *Chandra* PSF are brighter than the surface brightness expected for these intergalactic scattering halos. The X-ray signatures of intergalactic dust may only be visible if a distant quasar suddenly dimmed by a factor of 1000 or more, leaving behind an X-ray scattering echo, or "ghost" halo.

(This page left intentionally blank.)

Contents

(This page left intentionally blank.)

List of Figures

List of Tables

(This page left intentionally blank.)

ACKNOWLEDGMENTS

Thank you to my friends, peers, and mentors who have provided both emotional support and advice throughout my graduate school career: Kevin Hainline, Destry Saul, Joshua Schroeder, Gurtina Besla, and Kelle Cruz.

I would also like to thank the many researchers and senior scientists I have interacted with over the years, who have greeted me with open arms and welcome advice: Herman Marshall, Randall Smith, the MKI research staff, CXC staff, and more.

Thank you finally to my close friends and family both passed and present: Mom, Dad, Brian, Kyle, the D'Orazios, Noodle and Dalia, René, and friends of the Harlem Flophouse. Without your mark on my life the stars would not shine as bright.

2014, New York City

(This page left intentionally blank.)

Chapter 1

Introduction

Astrophysical dust acts as either a source of contamination or an essential piece of physics, in every subject from star and planet formation to galaxy evolution and cosmology. Dust is any particulate matter ranging from molecules tens or hundreds of atoms in size to minerals (usually graphite or silicate) a few microns wide. Metals dominate the cooling processes of the interstellar medium (ISM), leading to star formation. A fraction of the metals are in dust grains, providing a site for chemical reactions and shielding gas molecules from destruction by stellar radiation. The dust grains in stellar birth clouds are also the seeds for growing planetesimals, the building blocks of planets.

Dust absorbs more blue light than red, altering the apparent color of stars, star forming galaxies, and active galactic nuclei (AGN). The absorbed light heats the grains, which reemit the energy as infrared light. This fact is used to estimate dust mass and to calibrate the spectral energy distribution of distant galaxies and AGN hosts for star formation rate. Infrared emission from distant galaxies is also used to estimate dust

mass and extinction. In all cases, dust models that fit the *local* ISM are applied to dust *everywhere* in the Universe.

The canonical study of Milky Way dust by Mathis et al. (1977, hereafter MRN) attempted to fit the $\lambda = 0.1-1$ μm Galactic extinction curve with a mixture of grain materials. They found that a power law distribution of grain sizes with slope ≈ 3.5 was sufficient, requiring substantial amounts of graphite mixed with silicate or other common minerals. While this fiducial work certainly deserves improvement, the simplicity of the model and ease of implementation has caused the grain size power law to be used in everything from planetary science to extragalactic astrophysics. New models include infrared and microwave emission to constrain the abundance of polycyclic aromatic hydrocarbons (PAHs) in addition to Milky Way, SMC, and LMC extinction curves (Weingartner & Draine 2001). A set of models by Zubko et al. (2004) does the same, informed by elemental abundance constraints and including large "fluffy" dust grains with a low filling factor, which one might expect to grow in a diffuse environment.

I focus on dust scattering of X-rays over small angles, which produces a diffuse halo image around bright X-ray point sources (Overbeck 1965; Hayakawa 1970). The first X-ray scattering halo was imaged with the Einstein Observatory around GX399-4 (Rolf 1983). Since then, X-ray halos have been observed around Galactic X-ray sources (e.g. Witt et al. 2001; Smith 2008), anomalous X-ray pulsars (Tiengo et al. 2010), and gamma-ray bursts that pass through dusty regions of the Milky Way (Vaughan et al. 2006). The study presented here, like many before it, uses MRN as a starting point, attempting to push the limits of observations towards the large end of the grain size distribution.

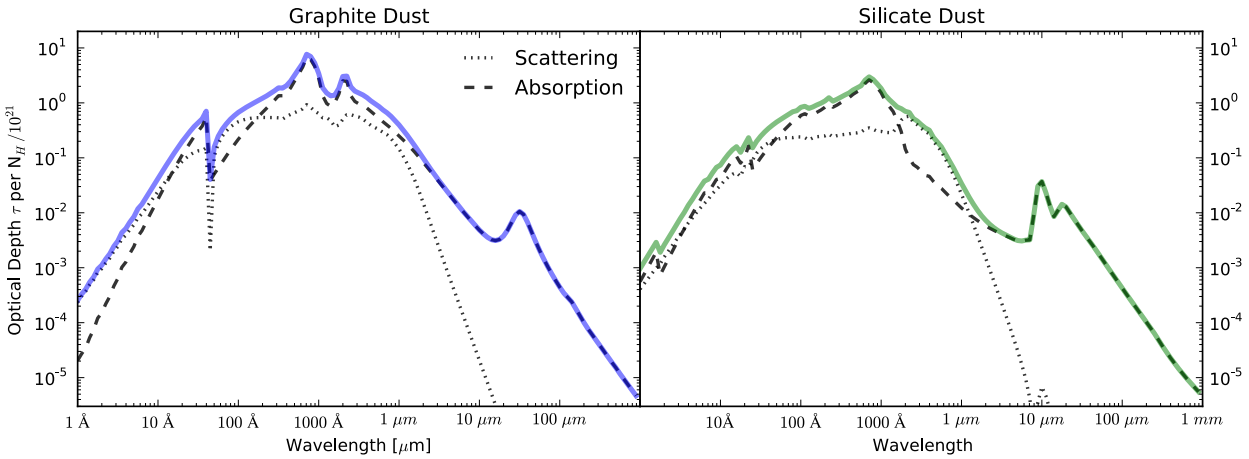

Figure 1.1 The optical depth per $N_H/10^{21}$ cm^{-2} for typical Milky Way dust (MRN) is shown for different suspected ISM dust grain compositions: (*left*) graphite grains (excluding PAHs), and (*right*) silicate grains. The total extinction is the sum of absorption (dashed lines) and scattering (dotted lines).

1.1 Dust Absorption and Scattering Across the Electromagnetic Spectrum

Dust can be studied through extinction (optical reddening), emission (from 100 μm – 1.3 mm), and scattering (in the UV and X-ray). Figure 1.1 shows typical Milky Way ISM extinction per 10^{21} hydrogen atoms, using an MRN distribution and optical constants from Draine (2003b). It illustrates how ISM dust is most absorptive at UV wavelengths, processing the captured energy into heat and reemitting light in the infrared (e.g. Draine & Li 2007). While infrared light provides a means to probe dust in emission, the extinction peaks, troughs, and slopes from all portions of Figure 1.1 are also broadly applied by researchers to understand the abundance and content of astrophysical dust.

The scattering and absorption properties of dust grains under different sources of illumination can be summarized by the relation between wavelength and grain size.

1. $a << \lambda$: When a dust grain is much smaller than the wavelength of light, the electric

field within the grain is relatively uniform. The result is an oscillating dipole, set up by the dielectric response of the grain to the changing electric field of incident radiation. This is the classic Rayleigh scattering regime,[1] and if the index of refraction does not change significantly with wavelength, $Q_{\rm sca} \propto \lambda^{-4}$ and $Q_{abs} \propto \lambda^{-1}$. Thus at very long wavelengths absorption dominates over scattering.

2. $a \sim \lambda$: For wavelengths on the order of the dust grain size, geometric resonances arise. For spherical grains, the Mie solution offers an exact formulation of the scattering and absorption cross-sections. Figure 1.2 shows how the extinction efficiency $Q_{\rm ext}$ changes with grain size. Scattering resonances are strongest when $\lambda \approx 1 - 3\ a$, leading to beautiful phenomena such as reflection nebulae and coreshine. When $\lambda \lesssim a$ the dust grain acts like a screen, where the efficiency of both absorption and scattering (diffraction) are about equal, yielding $Q_{\rm ext} \sim 2$. Dust that causes a relatively flat extinction across optical wavelengths is deemed "grey" because it lacks distinguishing spectral characteristics. Since the bulk of our understanding of the diffuse interstellar dust grain size distribution comes from the preferential absorption of blue light from wavelengths $0.1 - 1\ \mu$m, it should not be surprising that canonical size distributions tend to cut off around $0.2 - 0.5\ \mu$m (e.g. Mathis et al. 1977; Weingartner & Draine 2001).

3. $a >> \lambda$: This is the regime of X-ray scattering, discussed in the next section.

[1]There is an additional condition necessary for Rayleigh scattering – that the index of refraction is not so large that the time it takes the dielectric to establish a static electric field across the grain is longer than the period of the incident wave. The velocity of the electric field within the grain is c/m, so this condition requires $ma << \lambda/2\pi$ (van de Hulst 1957).

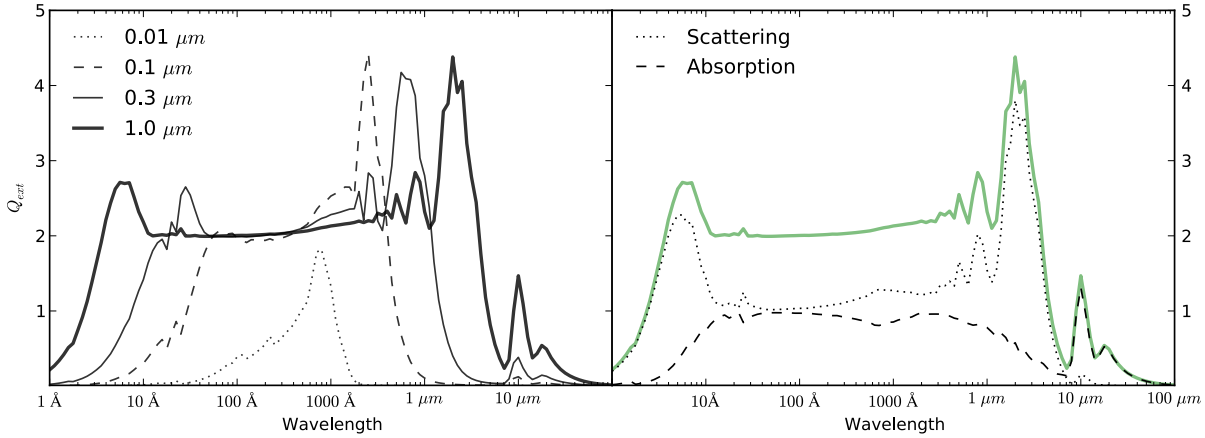

Figure 1.2 (*Left*) The spectrum of extinction efficiency $Q_{\rm ext}$, calculated for spherical silicate grains, changes shape depending on the grain radius. (*Right*) For wavelengths on the order of the grain size, scattering resonances (dotted line) greatly enhance the total extinction efficiency, shown here for grains of radius 1 μm. At shorter wavelengths the grain is effectively a screen, scattering and absorbing (dashed line) with equal efficiency ~ 1 until we get to the Rayleigh-Gans scattering regime around 1 keV.

1.2 X-ray scattering cross section

When the index of refraction is close to 1, the phase shift and attenuation of light is negligible as it enters a dust grain. When these conditions hold one can apply the Rayleigh-Gans (RG) approximation, which integrates the wavefront contributions from a dielectric sphere with uniform response to the incoming electromagnetic wave (van de Hulst 1957; Overbeck 1965; Hayakawa 1970; Martin 1970).

The scattering cross-section is

$$\sigma_{\rm RG} = 2\pi a^2 \left(\frac{2\pi a}{\lambda}\right)^2 |m-1|^2 \tag{1.1}$$

for spherical grains of radius a and complex index of refraction m (e.g. Mauche & Gorenstein 1986). I follow Smith & Dwek (1998) in applying the Drude approximation for the complex index of refraction, which treats each dust grain as a sphere of free electrons.

Assuming that there are on average two baryons in the atomic nucleus for every electron,

$$|m-1| \approx \frac{n_e r_e \lambda^2}{2\pi} \tag{1.2}$$

where r_e is the classical electron radius and n_e is the number density of electrons, which I will calculate from the mass density. For values characteristic of dust grains,

$$\sigma_{\rm sca} \approx 6.2 \times 10^{-7}\ \rho_3^2\ a_{\mu{\rm m}}^4\ E_{\rm keV}^{-2}\ {\rm cm}^2 \tag{1.3}$$

where $\rho_3 = \rho/3\ {\rm g\ cm^{-3}}$ is a typical grain material density, $a_{\mu{\rm m}} = a/1\ \mu{\rm m}$, and $E_{\rm keV} = E/1\ {\rm keV}$.

The RG differential scattering cross-section contains a first order Bessel function, which can be approximated with a Gaussian function (Mauche & Gorenstein 1986):

$$\frac{d\sigma}{d\Omega} = \frac{4a^2}{9}\ \left(\frac{2\pi a}{\lambda}\right)^4\ |m-1|^2\ \exp\left(\frac{-\theta_{\rm scat}^2}{2\tilde{\sigma}^2}\right) \tag{1.4}$$

where $\tilde{\sigma}$ the characteristic width of the scattering angle distribution:

$$\tilde{\sigma} = \frac{1.04\ {\rm arcmin}}{E_{\rm keV}\ a_{\mu{\rm m}}}. \tag{1.5}$$

Using the Drude approximation again,

$$\frac{d\sigma_{\rm sca}}{d\Omega} \approx 1.13\ \exp\left(\frac{-\theta_{\rm sca}^2}{2\tilde{\sigma}^2}\right)\ \rho_3^2\ a_{\mu{\rm m}}^6\ {\rm cm}^2\ {\rm ster}^{-1}. \tag{1.6}$$

Smith & Dwek (1998) have shown that the Drude approximation applied to the RG

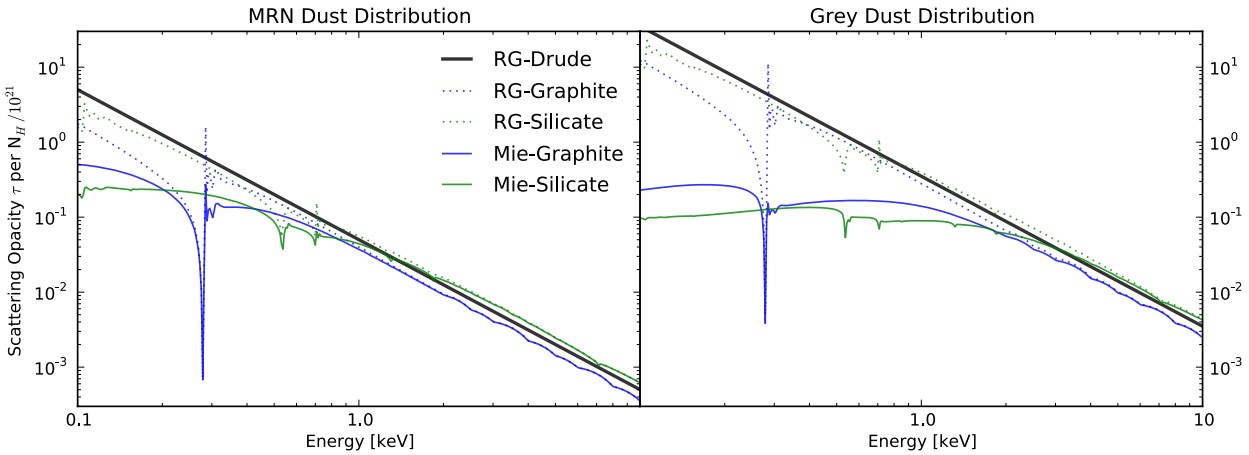

Figure 1.3 The scattering opacity of some typical astrophysical dust materials is shown for two grain size distributions: (*left*) that typical of the Milky Way with sizes ranging $0.005 - 0.25$ μm (MRN), and (*right*) a distribution of large 'grey' dust grains with sizes ranging $0.1 - 1.0$ μm. I apply the RG-Drude approximation (thick black lines) using the average dust grain material density (3 g cm^{-3}), well approximating a mix of graphite and silicate grains for $E > 1$ keV (*left*) and $E > 2$ keV (*right*). The RG approximation used in conjunction with the indices of refraction for graphite or silicate (dotted lines) reproduces scattering resonances at the photoelectric absorption edges, but still over-predicts the magnitude of scattering compared to the more exact Mie solution (solid lines).

scattering cross-section (RG-Drude, hereafter) agrees with the more exact Mie scattering solution in cases where $a_{\mu\mathrm{m}} \lesssim E_{\mathrm{keV}}$. Typical ISM dust has $a \leq 0.3$ μm, so the RG-Drude approximation holds for the majority of X-ray scattering studies. However, X-ray scattering is uniquely sensitive to large dust grains in comparison to studies at other wavelengths, and for this purpose one must consider interesting cases that depart from the Smith & Dwek (1998) rule-of-thumb, which breaks for softer X-rays.

Figure 1.3 (*left*) shows how the X-ray opacity of MRN dust ($dn/da \propto a^{-3.5}$ with $0.005 < a < 0.25$ μm) is overestimated by a factor of $2 - 10$ in the regime $E < 0.5$ keV. In cases where one is interested in detecting large 'grey' dust grains, e.g. $dn/da \propto a^{-3.5}$ with $0.1 < a < 1.0$ μm (Figure 1.3, *right*), RG-Drude overpredicts the amount of scattering by a factor of $5 - 100$ for $E < 1$ keV. Plugging more exact values for silicate and graphite indices

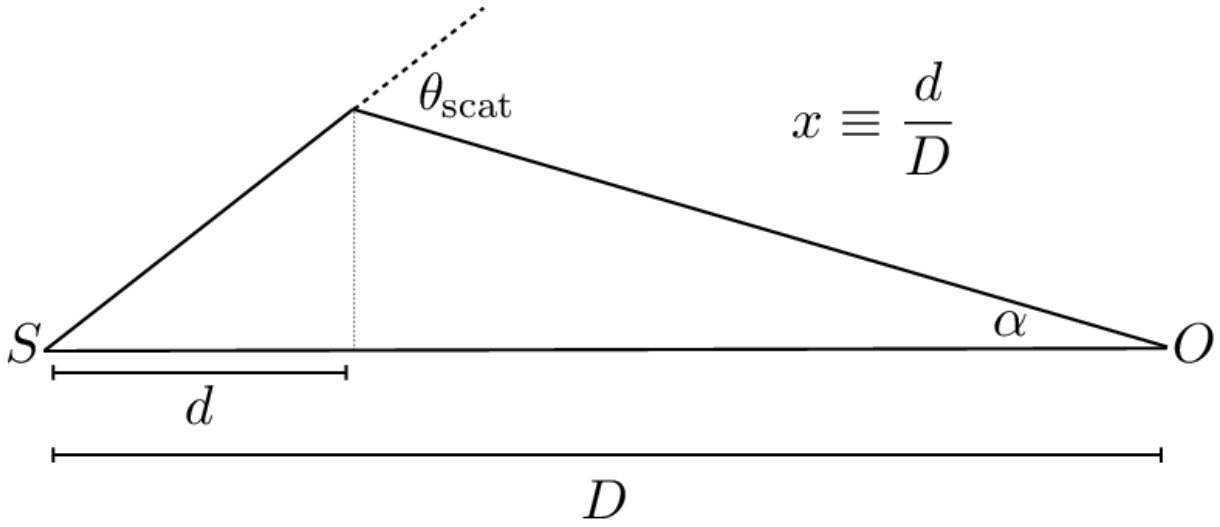

Figure 1.4 Geometry of X-ray scattering through the interstellar medium, with an X-ray point source at *S* and observer at *O*.

of refraction (Draine 2003b) into RG instead of the Drude approximation reproduces some absorptive effects and scattering resonances at the photoelectric absorption edges, but it does not completely compensate for the phase shifts incurred across the surface of the grain.

There is also a limiting angle beyond which the Gaussian approximation in Equation 1.4 no longer matches the exact Mie solution (Smith & Dwek 1998). For 2 keV photons and 0.1 μm (0.25 μm) grains, the solutions diverge around 500″ (200″). For soft X-rays < 1 keV, the Gaussian approximation matches the shape of the Mie solution out to at least 1000″. Whether or not the $a_{\mu\rm m} \lesssim E_{\rm keV}$ rule of thumb holds, Equation 1.4 reasonably describes the *shape* of the scattering halo image out to $\sim 200''$ and the brightness at energies > 1 keV.

1.3 Derivation of Scattering Halo Intensity

The intensity of the dust scattering halo is calculated by integrating the differential scattering cross-section at various angles along the line of sight (Figure 1.4). A patch of dust grains at $d \equiv xD$ away from the X-ray source will generally see a flux $L_S/4\pi d^2$. To be observed at angle α, the light must scatter onto $\theta_{\rm sca} = \alpha/x$. The amount of light scattered from point x onto α is therefore

$$\frac{dI(x,\alpha,a,E)}{D\,dx} = \frac{L_s\,n_d(a,x)}{4\pi D^2\,x^2}\frac{d\sigma}{d\Omega}\left(\frac{\alpha}{x},a,E\right) \tag{1.7}$$

where $n_d(a,x)$ is the number density of dust grains of radius a at x.

Note that scattered light reaching the observer will also be subject to extinction by intervening ISM, attenuated in total by $\tau_{SG} + \tau_{GO} = \tau_{SO} + \delta\tau$. Here $\delta\tau$ represents the additional extinction that scattered light incurs because it takes a longer path than the non-scattered light. Rewriting the luminosity in terms of F_a, the *apparent* flux at point O, yields $L_S e^{-(\tau_{SO}+\delta\tau)}/4\pi D^2 = F_a e^{-\delta\tau}$.

Using $N_d(a)$ to represent the total dust column and $\xi(x)$ to parameterize the density as a function of position along the line of sight, I integrate Equation 1.7 over the sight line and grain size distribution to get the scattering halo surface brightness as a function of energy:

$$I_h(\alpha,E) = \int_a\int_0^1 \frac{F_a}{x^2}\frac{d\sigma}{d\Omega}\left(\frac{\alpha}{x},a,E\right)e^{-\delta\tau}\,N_d(a)\,\xi(x)\,dx\,da. \tag{1.8}$$

I utilize two simplified cases for the form of $\xi(x)$: a uniform distribution of dust grains along the line of sight, $\xi(x) = 1$, and an infinitesimally thin screen of dust grains at

position x_s, so that $\xi(x) = \delta(x - x_s)$. Assuming that the ISM is homogeneous enough that the scattered light path does not differ significantly in extinction properites, $\delta\tau = \tau_{\rm SO}\delta x$. Small angle geometry yields

$$\delta x = \frac{\alpha^2(1-x)}{2x}. \tag{1.9}$$

The longest observable paths come from dust at intermediate distances, $x \sim 1/2$, yielding $\delta x \approx \alpha^2/2$. For the vast majority of sightlines, $\delta\tau$ is negligible because $\delta x \lesssim 10^{-5}$ for $\alpha < 1000''$. I therefore drop this term from all calculations of dust scattering through a homogenous medium. In cases of X-ray light scattering off compact dust clumps, $\delta\tau$ and its spatial dependence must be included.

1.4 Analytic Solutions for Dust Scattering Halos

The integral for the scattering halo intensity can be evaluated analytically under a few simple conditions. First, I assume that the grain size distribution is a power law function:

$$N_d \propto a^{-p} \tag{1.10}$$

Second, I use the Rayleigh-Gans differential cross section as described in the text:

$$\frac{d\sigma}{d\Omega} \propto a^6 \, \exp\left(\frac{-\alpha^2 a^2}{2\tilde{\sigma}_0^2 x^2}\right) \tag{1.11}$$

where $\tilde{\sigma}_0$ is the characteristic scattering angle for 1 μm size grains, $\tilde{\sigma}_0 = 1.04' \, E_{\rm keV}^{-1}$.

Finally, I assume that the medium along the line of sight is optically thin to dust

scattering. The single-scattering halo intensity, integrated over solid angle, is

$$\int I_h d\Omega = F_a \tau_{\rm sca} \tag{1.12}$$

For more information on second or third order scattering see Mathis & Lee (1991).

Plugging Equation 1.8 into Equation 1.12, I use A as a normalization factor that absorbs the proportionality constants from the dust grain size distribution and differential cross-section, described above.

$$F_a A \int a^{6-p} \int x^{-2} \xi(x) \int_0^\infty \exp\left(-\frac{\alpha^2}{2\tilde{\sigma}_0^2}\frac{a^2}{x^2}\right) 2\pi\alpha \, d\alpha \, dx \, da = F_a \tau_{\rm sca} \tag{1.13}$$

Integrating over α first will contribute an $(x/a)^2$ term. This yields

$$A = \frac{\tau_{\rm sca}}{2\pi\tilde{\sigma}_0^2 \, G_p(a,p)} \tag{1.14}$$

where G_p is:

$$G_p(a,p) \equiv \int_{a_{\rm min}}^{a_{\rm max}} a^{4-p} da \tag{1.15}$$

Under the above simplifying notation, Equation 1.8 becomes

$$I_h(\alpha) = \frac{F_a \, \tau_{\rm sca}}{2\pi\tilde{\sigma}_0^2 \, G_p(a,p)} \int a^{6-p} \int x^{-2} \xi(x) \, \exp\left(-\frac{\alpha^2}{2\tilde{\sigma}_0^2}\frac{a^2}{x^2}\right) dx \, da \tag{1.16}$$

1.4.1 An Infinitesimally Thin Dust Screen

In the case of an infinitesimally thin screen at position x_s, Equation 1.16 becomes

$$I_h(\alpha) = \frac{F_a\ \tau_{\rm sca}}{x_s^2\ 2\pi\tilde{\sigma}_0^2\ G_p(a,p)} \int a^{6-p} \exp\left(\frac{-\alpha^2 a^2}{2\tilde{\sigma}_0^2 x_s^2}\right) da \tag{1.17}$$

which produces the solution

$$I_h(\alpha) = \frac{F_a}{x_s^2}\ \frac{\tau_{\rm sca}}{2\pi\tilde{\sigma}_0^2}\ \frac{G_s(a,p,\alpha,x_s)}{G_p(a,p)} \tag{1.18}$$

where

$$G_s(a,p,\alpha,x_s) \equiv -\frac{1}{2}\left[\left(\frac{\alpha^2}{2\tilde{\sigma}_0^{\ 2} x_s^2}\right)^{\frac{p-7}{2}} \Gamma\left(\frac{7-p}{2}, \frac{\alpha^2 a^2}{2\tilde{\sigma}_0^{\ 2} x_s^2}\right)\right]_{a_{\rm min}}^{a_{\rm max}} \tag{1.19}$$

1.4.2 Uniformly Distributed Dust

In the case that the dust grains are uniformly distributed along the line of sight, Equation 1.16 becomes

$$I_h(\alpha) = \frac{F_a\ \tau_{\rm sca}}{2\pi\tilde{\sigma}_0^2\ G_p(a,p)} \int a^{6-p} \int x^{-2}\ \exp\left(-\frac{\alpha^2 a^2}{2\tilde{\sigma}_0^2 x^2}\right) dx\ da \tag{1.20}$$

The x term of the integral evaluates to

$$\sqrt{\frac{\pi}{2}}\ \frac{\tilde{\sigma}_0}{\alpha a}\left[1 - {\rm erf}\left(\frac{\alpha a}{\tilde{\sigma}_0\ \sqrt{2}}\right)\right] \tag{1.21}$$

Plugging this in, I get

$$I_h(\alpha) = \frac{F_a\ \tau_{\rm sca}}{\alpha\tilde{\sigma_0}\ \sqrt{8\pi}\ G_p(a,p)} \int a^{5-p} \left[1 - {\rm erf}\left(\frac{\alpha a}{\tilde{\sigma_0}\sqrt{2}}\right)\right] da \tag{1.22}$$

The solution is

$$I_h = \frac{F_a}{\alpha\tilde{\sigma_0}} \frac{\tau_{\rm sca}}{\sqrt{8\pi}} \frac{G_u(a,p,\alpha)}{G_p(a,p)} \tag{1.23}$$

where

$$G_u(a,p,\alpha) \equiv \frac{1}{6-p}\left[a^{6-p}\left(1 - {\rm erf}\left(\frac{\alpha a}{\tilde{\sigma_0}\sqrt{2}}\right)\right) - \frac{1}{\sqrt{\pi}}\left(\frac{\alpha}{\tilde{\sigma_0}\sqrt{2}}\right)^{p-6} \Gamma\left(\frac{7-p}{2}, \frac{\alpha^2 a^2}{2\tilde{\sigma_0}^2}\right)\right]_{a_{\rm min}}^{a_{\rm max}} \tag{1.24}$$

Both the error function (erf) and incomplete gamma function (Γ) are implemented with widely available and standard computing tools such as *Mathematica* and *scipy* for Python. The advantage to using erf and Γ functions over numerically integrating Equation 1.4 is a dramatic increase in computing efficiency, reducing hour-long calculations to seconds, making the Bayesian fitting techniques used in Chapter 3 feasible.

1.5 Motivation for Studying Dust in the X-ray

X-ray scattering is capable of calibrating our understanding of the local Milky Way ISM for grey dust, which extincts background light without altering its color. It also provides a means of searching for extragalactic dust reservoirs in the intergalactic (IGM) and circumgalactic medium (CGM). X-ray spectroscopy can also probe the constituent elements of dust grains, directly measuring the depletion of gas phase metals into dust. I outline here

the various ways in which high energy studies of astrophysical dust compliment science at other wavelengths.

1. X-rays can probe dense regions of the ISM that are inaccessible at other wavelengths. While the Milky Way disk is completely dark in UV and optical, 100 μm dust maps (Schlegel et al. 1998) and 21-cm HI emission surveys (Kalberla et al. 2005) are saturated and thereby considered unreliable for any sightline within a few degrees of the Galactic plane. However Figure 1.1 illustrates that the X-ray end of the curve is equally transparent to the infrared end of the spectrum, which is often used to look through dusty regions of space. Thus X-rays can be used to peer deep into the Milky Way disk, at column densities $N_H > 10^{22}$ cm^{-2}, from which dust still provides signatures of scattering and absorption.

2. The optical depth to X-ray scattering is uniquely sensitive to large dust grains. While stars are considered the primary source of dust, the grain destruction timescale in the ISM is shorter than the timescale of grain replenishment by stars (Jones et al. 1996). This means that the ISM must process grains significantly, both through destruction by shocks and by growth processes that are still highly uncertain. A search for large dust grains with X-ray scattering is thereby important for understanding essential processes and underlying physics of the ISM.

I have argued that the differential absorption of color – causing the typical 'reddening' of background stars – is due predominantly to grains that are smaller than the wavelengths being observed ($a \lesssim 0.3$ μm). Even MRN acknowledged that their study was particularly insensitive to dust grains ~ 1 μm. These large, grey grains effectively increase

the normalization of extinction curves without changing the slope. This leads to a larger extinction per unit reddening (R_V) and alters the brightness of background light without changing its color. Therefore understanding the abundance of large dust grains is also fundamental for calibrating luminosity and distance measurements.

Infrared and sub-millimeter wavelengths, which are commonly used to study dust, are also ineffective for probing the large end of the dust grain size distribution. Alterations to grain distributions formulated to match extinction curves in conjunction with observed emission in the infrared tend to affect the small end of the distribution (Weingartner & Draine 2001). This is because the smallest grains (PAHs and graphite $\lesssim 0.01$ μm) heat more efficiently and thus are responsible for the majority of the near infrared emission and spectroscopic features (Draine & Li 2007). At sub-mm wavelengths where larger grains radiate, the slope of the spectral energy distribution (β) is more sensitive to grain composition and optical constants than their size (Ossenkopf & Henning 1994).

3. X-rays have sufficient energy to eject deep electrons from the heavy elements comprising dust grains, making X-ray spectroscopy an essential tool for probing the chemical composition of interstellar dust. When an $n = 1$ or $n = 2$ electron is ejected from an atom, it causes a marked increase in the ISM absorption cross-section, called the photoelectric absorption edge. The bulk of ISM grains (by number) are transparent to X-rays, leaving absorption edge features on the spectrum of intervening light (Wilms et al. 2000). The depth of an X-ray absorption edge is therefore directly proportional to the column density of the respective element, allowing X-ray spectroscopy to probe contributions from *both* the gas and solid phase. If combined with spectroscopy of gas

phase elements at other wavelengths, we have a direct measurement of ISM depletion that avoids assumptions about the mixture of ISM metals. In contrast, the depletion of heavy elements into dust has historically been inferred by comparing the abundance of gas phase ions to the assumed near-solar abundance of the Milky Way ISM (Draine 2011).

Currently the vast majority of our knowledge concerning the composition of astrophysical dust comes from infrared spectroscopy, where features associated with molecular stretching and bending modes of common minerals occur. The most successful mineralogical identifications today are for *circumstellar* dust, which is produced in the atmospheres of dying stars; the identification of infrared absorption features from the diffuse ISM (DIBs) remains ambiguous (Molster et al. 2010). However, X-ray light scattered by dust in the diffuse ISM should be subject to resonances associated with the photoelectric absorption edges. Figure 1.5 shows the theoretical X-ray opacity of dust grains using optical constants from Draine (2003b), illustrating how a high resolution spectrum of scattered light can differentiate between various dust grain compositions proposed for the diffuse ISM. Each dip in the scattering spectrum directly reveals an elemental comprising the dust grains, complementing efforts to identify minerals responsible for infrared features.

While *Chandra* and the XMM Reflection Grating Spectrometer provide the best X-ray spectroscopic resolution available currently in space, it is achieved by passing the X-ray light through a grating. This smears the scattering halo image across the detector, making it incredibly difficult to differentiate the various scattering order images. The next generation of X-ray instrumentation – micro-calorimetry – is capable of providing similar resolution for *imaging* spectroscopy. The joint JAXA/NASA mission, Astro-H (Takahashi

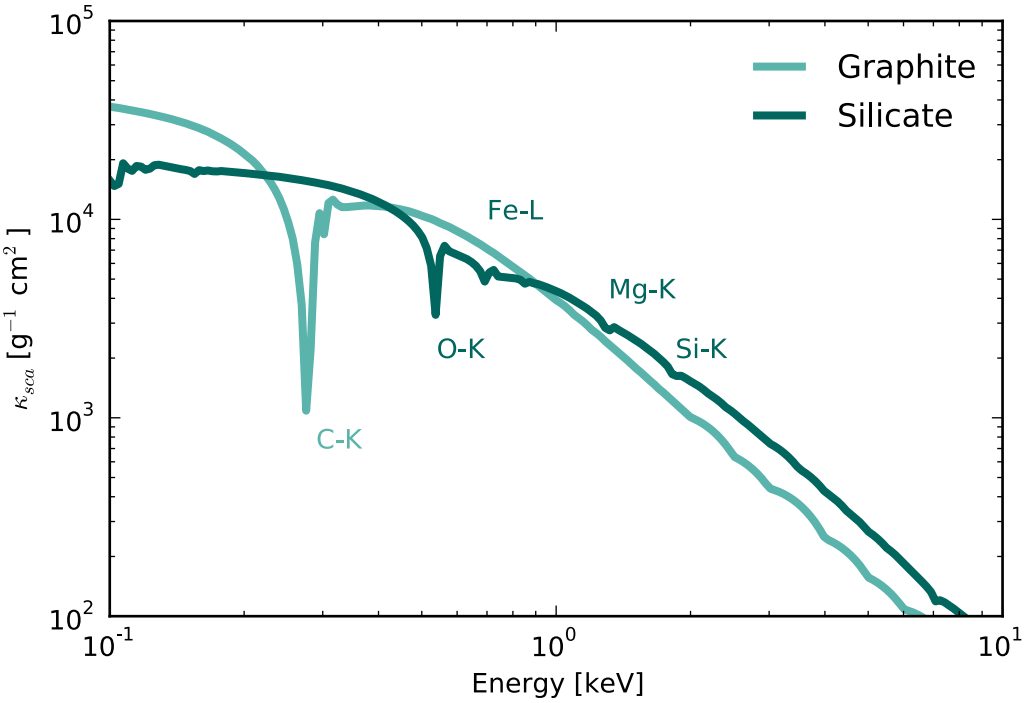

Figure 1.5 The scattering opacity for an MRN distribution of dust grains is shown for grains composed of astrosilicate (*dark green*) or graphite (*light green*). The scattering resonances complimentary to the photoelectric absorption edges are labeled.

et al. 2010), will contain such an instrument and is scheduled to launch in the near future. This instrument will be more suitable for measuring the high resolution spectrum of a scattering halo.

Future X-ray missions may also be able to resolve X-ray absorption fine structure (XAFS), which is the alteration of a photoelectric absorption edge that occurs when the absorbing material is in a solid (crystalline) form. Current X-ray observatories are just barely capable of resolving such structure, and future missions with larger effective areas and energy resolution $E/\Delta E \gtrsim 1000$ will open up the field of condensed matter astrophysics (Lee et al. 2009; Lee 2010).

(This page left intentionally blank.)

Chapter 2

Observationally Determined *Chandra* HETG Point Spread Function

The *Chandra* X-ray Observatory, a satellite launched by NASA in 1999, was the first X-ray telescope to offer superior grating resolution ($E/\Delta E \sim 1000$ at 1 keV) and remains unsurpassed in X-ray imaging resolution (0.5″ per pixel). *Chandra* is sensitive to 0.1 – 10 keV photons with an effective area around 500 cm^2, yielding a limiting flux 4×10^{-15} erg cm^{-2} s^{-1} for 10 ks of observation. Bright objects, which might register around one X-ray event per second, have fluxes $\sim 10^{-11}$ erg cm^{-2} s^{-1}.

The point spread function (PSF), describing the response of an instrument to illumination from a point source, is knowledge essential for treating extended features in the vicinity of a bright object. I will discuss the *Chandra* PSF in terms of the radial surface brightness profile for on-axis sources imaged by the Advanced CCD Imaging Spectrometer (ACIS). Off-axis sources are known to have extended and asymmetric radial profiles

and will not be covered in detail. The PSF is characterized by two main features: the *core*, where the majority of light is focused, and the *wings*, where light is spread diffusely due to scattering off fine surface features in the mirror.

The supreme focusing power of *Chandra*, obtained with a series of nested parabolic mirrors called the High Resolution Mirror Assembly (HRMA), confines around 90% of point source light to a 2-3 pixel region. The PSF tends to be more extended for higher energy X-rays. This is because micro-abrasions on the mirrors, which scatter light away from the focal point, have a larger effect on the shortest wavelengths of light. The radius enclosing 90% of point source light is 1″ and 2″ for 1.5 keV and 5 keV, respectively (*Chandra* Proposers' Observatory Guide,[1] hereafter CPOG).

Since the telescope mirrors reflect X-rays at grazing incidence angles, ground based efforts to determine the PSF wings were hindered by the fact that calibration sources are not an infinitely large distance away, hence the incoming light rays are not parallel to eachother. As the photon energy increases, smaller angles are required to maintain reflection efficiency. Compounded by the fact that high energy light is easily scattered by micro-abrasions, the PSF wings are generally considered uncertain on a level $\sim 10\%$,[2] which is comparable to the total brightness of an astrophysical X-ray scattering halo. Thus scattering halo observations require careful accounting of the *Chandra* PSF. There are two common approaches to constructing a PSF for observations that require it.

Simulation: The *Chandra* PSF can be simulated through a suite of publicly available

[1] http://cxc.harvard.edu/proposer/POG/
[2] Personal communication with *Chandra* X-ray Center staff.

tools, Chandra Ray Tracer (ChaRT)[3] and Marx.[4] SAO maintains a ray-trace simulation of the *Chandra* mirror optics (SAOTrace), version 1 of which is accessible through a web interface (ChaRT), used in this work. The ray-trace simulates the PSF from the HRMA only; the results must be processed by Marx to account for the behavior of the instrument, including a ray-trace simulation of the HETG if needed. Marx can also be run with a pileup model (see Section 2.1). Several scattering halo studies have used simulated PSFs to extract the inner regions ($\leq 50''$) of scattering halos (Xiang et al. 2007; Ling et al. 2009b; Xiang et al. 2011). For regions outside of 50″, it has been shown that the SAOSAC ray trace underpredicts the PSF brightness by a factor of 2-10 (Smith et al. 2002).

Observational Templates: To bypass the uncertainty in simulated PSF wings, researchers have occasionally turned to making observationally derived templates using bright point sources with relatively dust free sight lines. Such efforts are greatly hindered by pileup, which affects bright sources capable of producing high signal-to-noise wings (see Section 2.1). A PSF calibration effort by Gaetz et al. (2004, hereafter G04) coupled an HETG observation, needed to sample the PSF core, with a grating free observation, which has a piled up core but a good sampling of the PSF wings. The radial profiles from each observation are patched together to produce a single contiguous PSF, binned over a broad energy range. Using a patchwork PSF can be problematic, since the manufactured transition between PSF core and wings may increase systematic uncertainty in that region. The HETG effect on the PSF core shape is also unknown, but generally ignored. Several scattering halo studies have taken the piecewise approach by combining the simulated

[3]http://cxcoptics.cfa.harvard.edu/SAOTrace/Index.html
[4]http://space.mit.edu/ASC/MARX/

inner PSF with observationally derived wings from Her X-1 or other bright sources (Xiang et al. 2005; Mao et al. 2014). Most simply ignore the inner portion of the halo (Smith et al. 2002, 2006; Valencic et al. 2009). A calibration memo by Gaetz (2010, hereafter G10)[5] provides the most comprehensive review of the PSF wings (outside of 15″, or $r > 30$ pixels) to date using the same grating free observation of Her X-1 (ObsId 3662) used in G04.

A third option, parametric models of the energy dependent *Chandra* PSF, was explored in G04 and G10. However, some dust scattering papers have also used fits to a template object profile, in lieu of subtracting the raw surface brightness profile (Smith 2008; Valencic & Smith 2008; Valencic et al. 2009). An approach that includes the PSF core is rarely used due to the non-linear effects of pileup. I will revisit the work of G04 by examining pileup in the core of Her X-1 (ObsId 2749), which was initially assessed to be minimal (less than 5%). I revisit the work of G04 to examine the appropriateness of using Her X-1 and other bright point sources with relatively dust free sight lines for modeling the *Chandra* PSF. I seek here to provide a definitive, energy dependent model for the *Chandra* HETG PSF that will improve resolution of dust scattering halos close to their respective point sources.

I identified candidate PSF template observations by searching TGCat (Huenemoerder et al. 2011) for X-ray sources that satisfied a few conditions: (i) being bright (≥ 0.3 counts per second), with (ii) a long exposure time ($\geq$ 30 ks), and (iii) a low ISM column, as determined from Schlegel et al. (1998) maps. I took $N_H/E(B-V) \approx 5.8 \times 10^{21}$ cm^{-2} mag^{-1} (Bohlin et al. 1978), and chose a cut off of $N_H \lesssim 10^{20}$ cm^{-2}, i.e. $E(B-V) \leq 0.02$ mag. Table 2.1 lists all the candidates I found that meet these criteria. I chose three out of the five objects

[5]http://cxc.harvard.edu/cal/Acis/detailed_info.html

Table 2.1. Candidate PSF template sources from TGCat

Object	ct/s	ks	E(B-V)	Notes
Her X-1	0.4	50	0.014	LMXB, used by Gaetz et al. (2004)
QSO B1028+511	0.5	69	0.014	Quasar, smooth power law
HR 5110	0.5	39	0.007	CV, power law with emission lines
Xi Uma	0.6	72	0.021	Spectroscopic binary, spectral lines
3C 273	3	39	0.021	Quasar with jet, smooth power law

(listed in Table 2.1) for this study: Her X-1, which was used in G04; QSO B1028+511, for its smooth power law; and 3C 273, which also follows a smooth power law and has been used as a PSF template in past X-ray scattering halo experiments (Smith 2008; Mao et al. 2014; Corrales & Paerels 2013).

By using HETG observations only, I am able to directly measure the degree of pileup by comparing the grating dispersed spectrum with that extracted from the CCD (Section 2.1). I then create normalized PSF templates for each of my template objects to examine the stability of the PSF wings across different observations (Section 2.2). I develop a parametric model of the energy (and pileup) dependent PSF core and wings, using 0.5 keV wide energy bins from 0.5-8 keV (Section 2.3). I compare the models derived here to that of G04 and G10 in Section 2.4. The results and their relevance to future work are summarized in Section 2.5.

2.1 Pileup

Pileup poses the most crucial difficulty for studying the *Chandra* PSF observationally. Incident photon energies are estimated from the charge accumulated in 3×3 pixel islands,

allowing a low resolution spectrum to be extracted from the ACIS instrument. Pileup occurs when more than one X-ray photon hits the same region of a CCD chip within one readout time (typically 3.2 seconds), causing multiple events to register as a single photon of higher energy or get discarded. Bright sources with $\gtrsim 0.3$ X-ray events per second, especially those bright enough to produce high signal-to-noise PSF wings within a reasonable telescope integration time, are subject to pileup.

Pileup changes the shape of the PSF core by decreasing the total number of counts and alters the CCD extracted spectrum, leading to an incorrect PSF normalization. A third pileup effect, called grade migration, causes information to be lost as some X-ray events will be filtered out. When an X-ray interacts with the CCD, it liberates a number of electrons proportional to the energy in the photon. The resulting electron cloud can span more than one pixel, so X-ray events are examined using a 3×3 pixel island and assigned a 'grade' based on the shape of the cloud. This filters cosmic ray interactions, which often produce large and asymmetric electron clouds ("blooming"), from valid X-ray events. When two X-rays hit the same region of a CCD chip, the resulting electron cloud is more likely to vary from the ideal (grade 0) and will be assigned a larger number. For multiply piled up events, the chances that the resulting electron cloud receives a passing grade (0, 2, 3, 4 or 6) diminishes. Examining event grades provides one method for diagnosing pileup, used by G04 and others (Smith et al. 2002, 2006; Valencic et al. 2009). In the most severe cases of pileup, piled events will be interpreted as cosmic rays and are removed during on-board processing. In these cases a bright point source will appear to have a dark, "hollowed out" core. Cases of severe pileup also exhibit a CCD readout streak,

which occurs when the point source is bright enough to produce a large number of X-ray events while charge is being moved from the exposed portion of the chip to the framestore.

Pileup can be mitigated with the High Energy Transmission Grating (HETG), whose zeroth order effective area is smaller by a factor of 5-10 than ACIS alone. The HETG almost always eliminates the problem of pileup from spectroscopic measurements by dispersing the point source light across the image. Another way to mitigate pileup is to reduce the frame readout time by storing only a subarray of CCD pixels, reducing the frame exposure times to 1.4 or 2.5 seconds. I will use HETG observations of bright, nearly dust-free point sources to compare the spectrum of grating dispersed light to the CCD spectrum extracted from the zeroth order image. This yields a direct measurement of the pileup fraction, described below. The formalism presented here provides a more robust method of gauging pileup, as opposed to grade migration.

2.1.1 Formulation of Pileup Effects

Excluding emission from the Sun, the brightest of high energy phenomena in the Universe reach Earth with a flux of a few $\times 10^{-3}$ photons cm^{-2} s^{-1}. With current technology, X-ray astronomy is a photon counting game requiring small number statistics. In the case of the *Chandra* ACIS instrument, photons incident on the same 3×3 pixel region cannot be easily distinguished if they occur within a single CCD readout time. Since *Chandra* has such a compact PSF, I will consider the idealized case that all point source photons hit the exact same spot on the detector. If I take μ to be the true (expected) value of photon events interacting with the CCD within one frame time, the probability that n events will occur

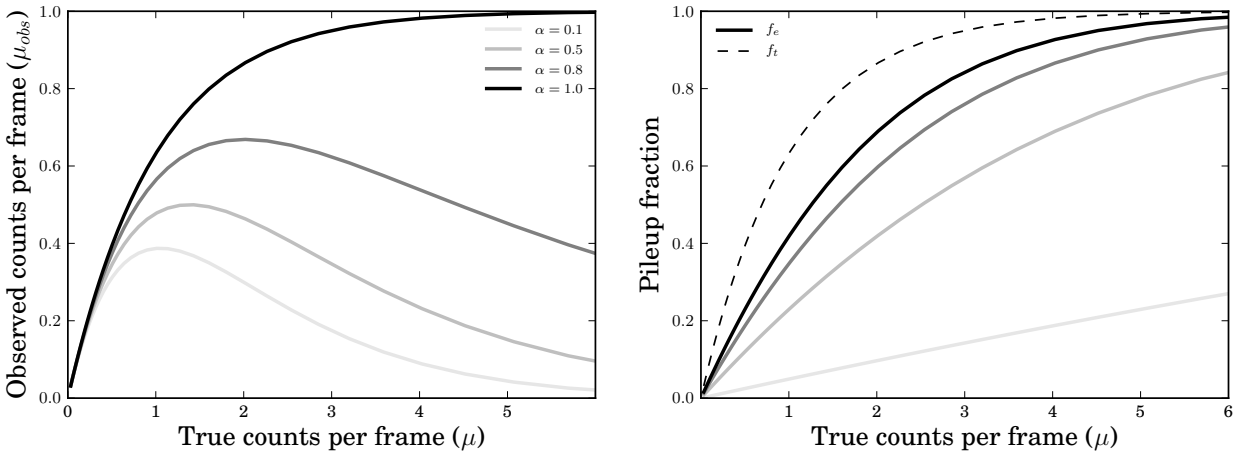

Figure 2.1 Pileup reduces the observed count rate relative to the true number (*left*). The number of photons (events) affected by pileup define the true (observed) pileup fractions (*right*). Some representative values for α, the average probability that incidences of two or more photon events receive a passing grade, are shown with differing shades of grey. Note that the count rate is just μ divided by the frame exposure time, so the center of each horizontal axis represents roughly 1 count per second for standard ACIS observations.

is described by the Poisson distribution:

$$p(n) = e^{-\mu} \frac{\mu^n}{n!} \tag{2.1}$$

In principle, only one count will be registered per frame, so the total number of counts observed in a single 3×3 pixel island is $N_{\rm obs} = N_f \; p(n \geq 1)$, where N_f is the total number of frames read in the observation. However as more photons hit the focal point, there is a larger the chance that the resulting electron cloud will be rejected due to grade migration. Davis (2001) introduced the parameter α to represent the probability that piled events receive a passing grade. The value for α should be highly dependent on n and the energies of each photon involved. Since we lack sufficient information to predict α, it will

be treated on average, noting that α can vary among observations. This yields

$$N_{\rm obs} = N_f \, \Sigma_{n=1}^{\infty} \alpha^{n-1} p(n) \tag{2.2}$$

for the total number of counts observed. Substituting the Taylor expansion formula $e^x = \Sigma_0^{\infty} x^n/n!$, the expectation value for number of observed counts per frame is:

$$\mu_{obs} = \frac{e^{-\mu}}{\alpha}(e^{\alpha\mu} - 1) \tag{2.3}$$

shown in Figure 2.1 (*left*) for varying degrees of α. This figure illustrates that any source observed with $\gtrsim 0.3$ counts per frame has suffered some degree of pileup. Even if the true value of μ is 1 count per frame, a lower rate (up to 0.6 counts per frame) will be observed due to the statistically likelihood of receiving $n \geq 2$ photons in one readout time.

A useful diagnostic is the pileup fraction, which can be written in a few ways.[6] I define the *true pileup fraction* by the true number of events that were subject to pileup effects:

$$f_t = 1 - \frac{N_f \, p(1)}{N_f \mu} = 1 - e^{-\mu}. \tag{2.4}$$

It is possible to measure f_t directly from HETG images because the grating dispersed light is not typically subject to pileup, yielding μ. The *observed pileup fraction*, characterized

[6]See *The Chandra ABC Guide to Pileup*, http://cxc.harvard.edu/ciao/download/doc/pileup_abc.pdf For consistency I have adopted their subscripts f_t and f_e for Equations 2.4 and 2.5.

Table 2.2. *Chandra* observations used for PSF templates

Object	Coordinates l, b	ObsId	Exposure time [ks]	Frame time [s]	Off-axis angle [arcmin]
QSO B1028+511	161.44, +54.439	3472	69.0	2.5	0.135
Her X-1	58.15, +37.523	2749	49.8	2.5	0.133
3C 273	289.95, +64.360	459	38.7	3.2	0.294

by the number of *detected* events that were subject to pileup,

$$f_e = 1 - \frac{N_f\, p(1)}{N_{\rm obs}} = 1 - \frac{\alpha\mu}{e^{\alpha\mu} - 1} \tag{2.5}$$

is a more pragmatic definition, but relies on the unknown value of α.

Figure 2.1 (*right*) shows the true and observed pileup fraction as a function of μ and α. Even when the expected count rate is one photon per frame, 70% of the photons will be piled and up to 40% of the *observed* events will have been assigned incorrect energies. In cases where α is small, the observed pileup fraction is low because so few piled events are accepted.

2.1.2 Pileup Measurements

Table 2.2 lists properties of the observations used in this study, including the frame exposure time and off-axis angle. Smaller frame times help reduce μ, thereby reducing the likelihood of pileup. Sources that are imaged far from the telescope's focal point (off-axis) will have a more extended and asymmetric PSF, but sources imaged within $1-2'$ of the focal point should be stable (CPOG).

I used standard calibration procedures with CIAO 4.5 and CALDB 4.5 to find the zeroth order point source position (`tg_findzo`) and to extract an HETG spectrum. A CCD spectrum was also extracted from a circular region of 5 pixel radius, centered on the `tg_findzo` coordinates. Figure 2.2 shows the resulting HEG (*blue*), MEG (*red*), and zeroth order spectrum with CCD resolution (*green*). The MEG has a more widely spaced grating (4000Å), which leads to smaller dispersion angles compared to the HEG grating (2000Å spacing). Thus the MEG extracted spectrum is more susceptible to pileup. The fact that the HEG and MEG spectra agree within each observation indicates that the dispersed light is free from pileup. The HETG spectrum thereby represents the true flux incident on the telescope.

I fit the continuum of each HETG spectrum using a power law, or sum of two power laws in the case of Her X-1. I measure the pileup by freezing the flux model parameters from the HETG fit, and then fit the CCD spectrum with the `jdpileup` model (Davis 2001) included. Figure 2.2 plots the model HETG spectrum, i.e. the true continuum flux (*solid grey line*), and the fit to the CCD spectrum (*dashed grey line*). I used the HETG model flux to estimate the number of zeroth order photon events per frame time μ integrated over 0.5-8 keV. The observed number of counts per frame time, $\mu_{\rm obs}$, is calculated by integrating the total number of photon events in the 0.5-8 keV range from the CCD extracted spectrum. Table 2.3 lists these values along-side the results of `jdpileup`, which also returns an estimate of the pileup fraction f_e. The observations are labeled I-III in order of increasing pileup fraction.

It is unclear why the dimmest object (QSO B1028+511) exhibits the smallest α. Perhaps

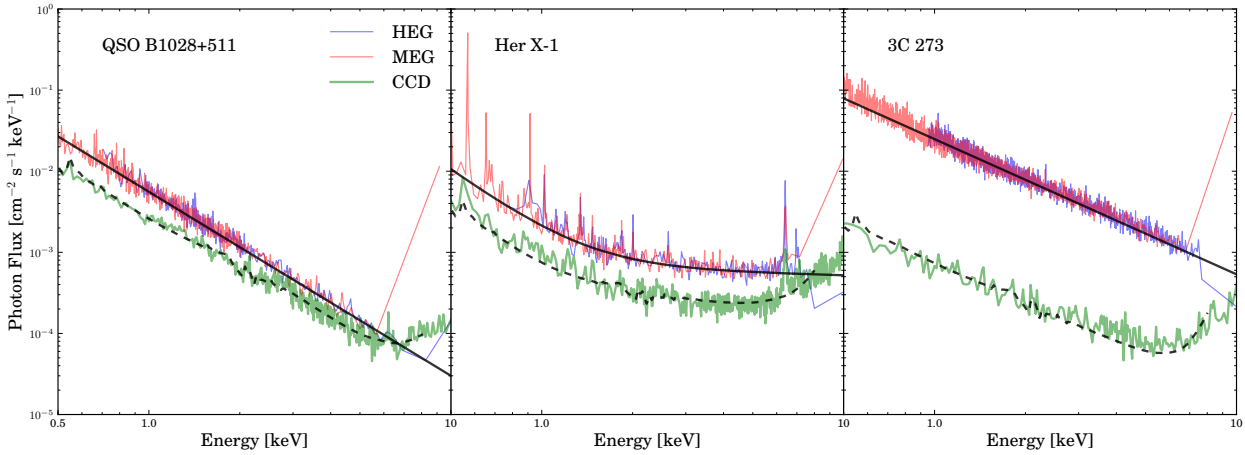

Figure 2.2 Spectra are shown for each observation in Table 2.2. The spectrum extracted from the HEG dispersed light (*blue*) is less subject to pileup than that dispersed by the MEG (*red*). The flux measured from the CCD extracted spectrum (green) is affected by pileup in all the observations. The true apparent flux, fit with the solid black line, requires a pileup model to fit the CCD spectrum, marked with a dashed black line.

Table 2.3. Results of `jdpileup` model

Object	Flux [erg cm^{-2} s^{-1}]	μ	$\mu_{\rm obs}$	α	Pileup fraction f_e
I. QSO B1028+511	1.9×10^{-11}	0.98	0.55	0.50	0.21
II. Her X-1	3.3×10^{-11}	1.2	0.51	0.81	0.39
III. 3C 273	1.4×10^{-10}	6.5	0.22	0.97	0.998

electron clouds resulting from two to three X-ray events are more asymmetric than those resulting from a larger number of compounded events, which might blend together to form a symmetric cloud. As long as the total energy deposited is lower than the threshold for cosmic ray flagging, such events may receive a passing grade. This could explain why 3C 273, by far the brightest object used in this study, exhibited $\alpha \approx 1$.

G04 looked for pileup in ObsId 2749 (II in Table 2.3) by examining the number of counts per frame ($\mu_{\rm obs}$) per pixel, concluding that the core was subject to around 5% pileup. They also examined grade ratios: the total number of grade 0 (best) or grade 6

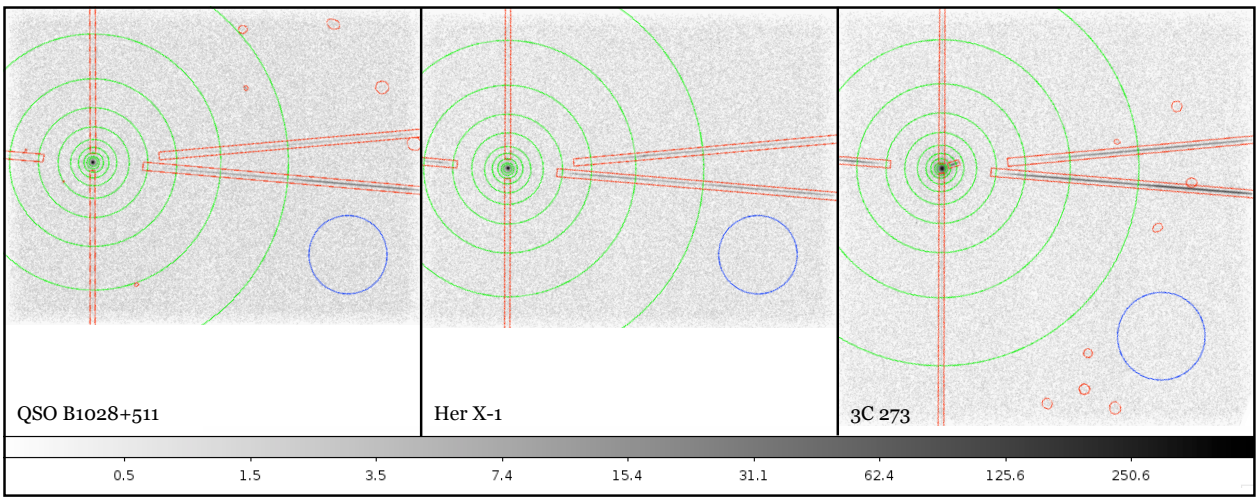

Figure 2.3 The images and their respective masks (*red*), background (*blue*), and annular regions (*green*, shown here for only $r > 11$ pixels) used to produce the *Chandra* PSF templates.

(least acceptable) events divided by the sum of acceptable events (grade 0, 2, 3, 4, and 6) as a function of radius. This also led them to conclude that pileup in the core of ObsId 2749 was mild. Unfortunately, sources subject to moderate or extreme pileup can sometimes appear well behaved because the observed count rate is significantly reduced. My analysis, comparing the spectrum extracted from the HETG dispersed light versus the CCD, has shown that approximately 40% of the observed zeroth order counts in ObsId 2749 were piled events. This would undoubtedly affect their parametric models and attempts to observationally determine the pristine, pile-up free *Chandra* PSF.

2.2 Templates

To test the validity of using individual observations as PSF templates, I will compare the normalized surface brightness profiles of Her X-1 (used in Smith et al. 2002; Valencic et al.

2009; Xiang et al. 2005), 3C 273 (used in Smith 2008; Mao et al. 2014, and Chapter 3), and QSO B1028+511. I created masks for the readout streak, HETG dispersed light, and extraneous sources found with `celldetect`. Readout streaks were not readily apparent in ObsIds 3472 and 2749, but their targets are bright enough to produce one. Masks for these two observations were chosen using Marx simulated images as a guide. Masks for the HETG dispersed light were constructed with a width of 20 pixels – two times the size of the default source extraction region. The HETG masks cover all dispersed light up to 10 keV on the MEG arm and 15 keV on the HEG arm, corresponding to regions > 128 pixels (MEG) and > 169 pixels (HEG) from the point source center. The image of 3C 273 also contained a jet, which was masked out.

Figure 2.3 shows the ACIS-S3 chip from each observation. The masks excluded from the radial surface brightness profiles are shown in red. I selected background regions far from the point sources, shown in blue. The profile annuli for $r > 11$ pixels, which are logarithmically spaced out to 500 pixels, are shown in green. I used annuli with 1 pixel spacing ($0 < r < 3$) and 2 pixel spacing ($3 < r < 11$) to maximize signal in the area of the PSF core-wing transition. Background subtracted surface brightness profiles were created using `dmextract`.

I will first compare the simulated and observed PSF to determine where the two diverge and by how much. I used ChaRT to simulate the HRMA PSF, then Marx to simulate an image. The `marxpileup` tool was run using the α value measured from each observation (Table 2.3). The zeroth order of the Marx simulated images was also centered using `tg_findzo` before extracting a surface brightness profile. Figure 2.4 compares the

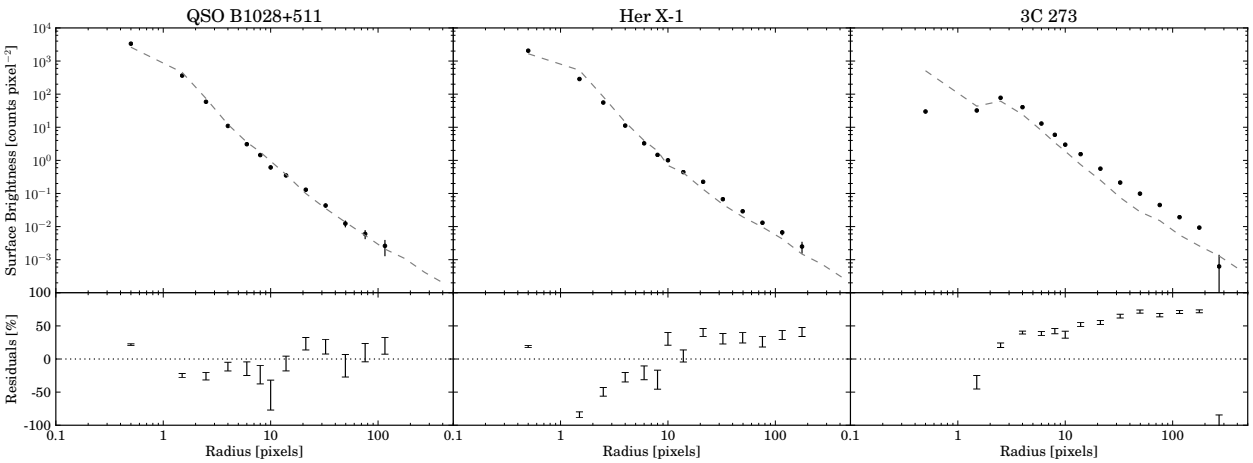

Figure 2.4 *Top:* The 0.5-8 keV surface brightness profiles for each object in this study (*black points*) are plotted with the profiles from a simulated image using `marxpileup` (*dashed grey line*). *Bottom:* The residual counts for each annulus are plotted in units of percent.

simulated and observed 0.5-8 keV surface brightness profiles. The brightest object, 3C 273, produces the most signal and makes it clear that simulated PSFs under-predict the amount of light that will scatter onto $r > 10$ pixels. This result was also confirmed by Smith et al. (2002) using a grating free observation of Her X-1 (ObsId 3662).

The bottom portion of Figure 2.4 plots the residual profile counts in units of percent, showing that the `marxpileup` simulation is missing 25-80% of the light from the brightest PSF wings. I suspect that the Marx simulated surface brightness profile for QSO B1028+511 is in relative agreement with the observed data because, as will become more apparent in Section 2.3, QSO B1028+511 is dim at high energy and thus produces relatively little signal where scattering from fine surface features in the mirror should be more prevalent.

Next I created normalized templates to examine the stability of the observationally determined wings. I divided each image into 0.5 keV wide energy bins from 0.5-8 keV. Normalizing the surface brightness profiles by the point source flux and effective area

produces a sufficient PSF template,

$$\Psi_t(r) = \frac{\mathcal{SB}_{ps}(r)}{F_{ps}\mathcal{A}_{ps}} \tag{2.6}$$

where $\mathcal{SB}_{ps}(r)$ is the background subtracted surface brightness profile (counts pixel^{-2}) from the template point source, $\mathcal{A}_{ps}$ is the exposure map effective area (counts photon^{-1} cm^2 s) at the point source center, and F_{ps} is the HETG determined point source flux (photon cm^{-2} s^{-1}). To measure $\mathcal{A}_{ps}$, I created weighted exposure maps with $\Delta E = 0.1$ and measured the mean value for the same 5 pixel radius region used to extract the CCD spectrum. This method is also used in Chapter 3.

Since $\Psi_t(r)$ is affected by pileup, it will not necessarily integrate to one. $\Psi_t(r)$ also does not account for spatial variations in the exposure map, which are due either to changes in the effective exposure times (on the edge of the chips) or to inherent variations in the CCD efficiency (e.g. bad pixel columns). Because the *Chandra* PSF wings originate from scattering off the HRMA, variations in the exposure time should be ignored while variations in the chip sensitivity should not. I examined the mean exposure map value for each annular region, finding less than 5% variation in the mean effective area for $r < 200$ pixels. Outside of this region, the effective area falls by about 50% because the annuli overlap with the chip edges, which have a lower effective exposure time. Regardless, there are very few data points with $r > 200$ pixels that meet the signal requirements described below, so the chip edges are not a concern. I therefore expect the $\Psi_t(r)$ template profiles to be accurate to within 5% for other objects imaged on-axis and for $r < 200$ pixels.

Figure 2.5 plots $\Psi_t(r)$ for each energy bin. Data points that met the following criteria were rejected:

(i) any value of $\mathcal{SB}_{ps}$ that was consistent with zero,

$$\mathcal{SB}_{ps} < \sigma_{ps}$$

(ii) or with a signal-to-noise less than three

$$C_{ps} < 3\sqrt{C_b}$$

where C is the number of counts in each annulus, coming from either the point source (C_{ps}) or the background (C_b).

QSO B1028+511 (ObsId 3472) had the fewest data points that met these criteria, perhaps because it also had the highest background. 3C 273 (ObsId 459) had the lowest background and brightest PSF wings, making it the most reliable object for estimating a PSF out to 200 pixels. The fact that the majority of the template wings are consistent within 1-2σ of each other gives good indication that the PSF wings are stable. There are only a few noticeable inconsistencies in the PSF templates for 2-2.5 keV and 6-6.5 keV bins (Figure 2.5). This may be due to non-uniformities in the background level or underestimates of the point source flux in the region of bright emission lines, which is particularly relevant in the case of Her X-1.

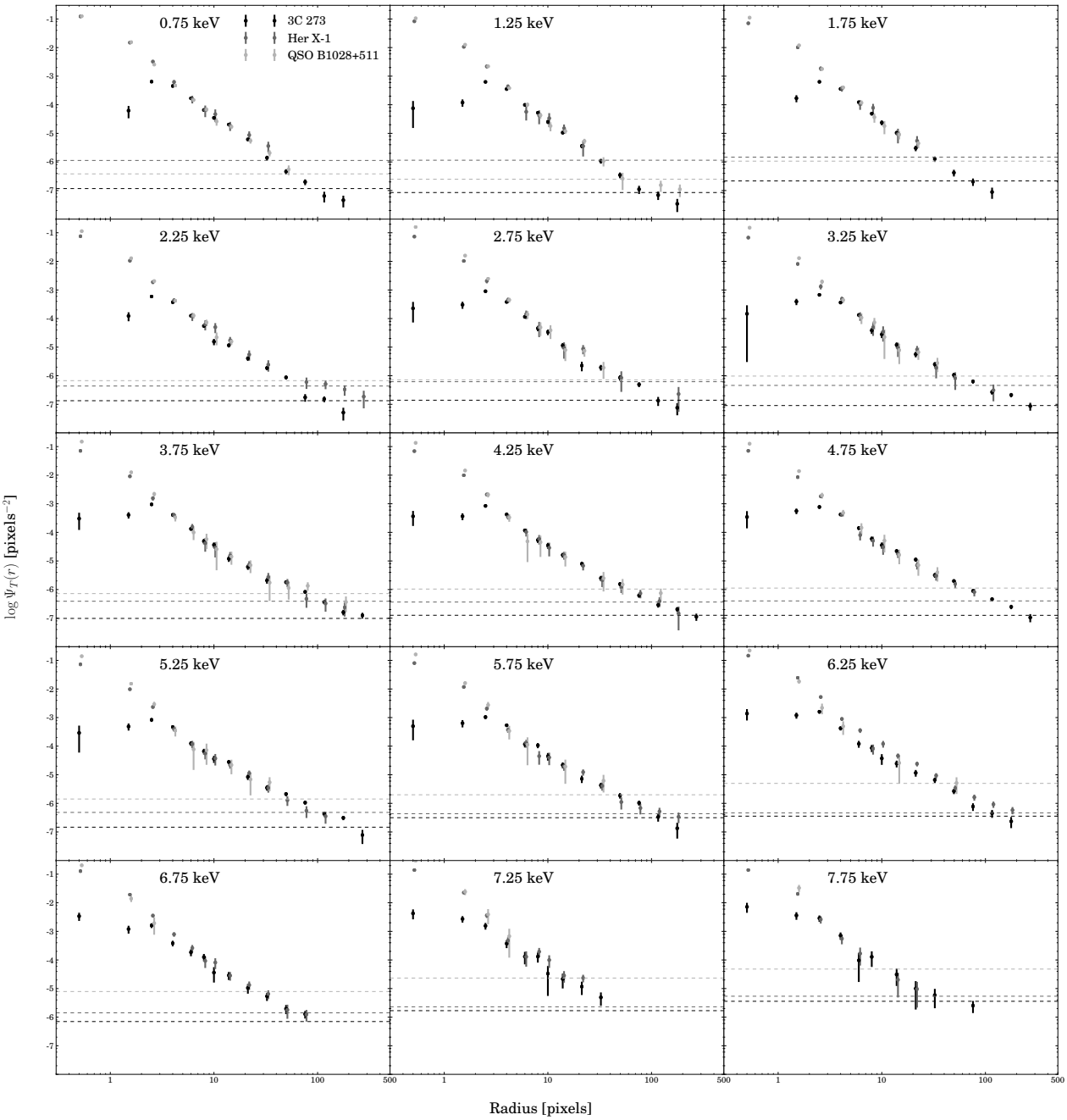

Figure 2.5 PSF templates normalized by point source flux and effective area according to Equation 2.6. The respective background levels are marked with dashed lines. In general, the normalized profile wings overlap within 1-2σ, suggesting that the instrument PSF wings are stable even when the core is subject to pileup. The data points are slightly offset horizontally from each other to make them more visible.

2.3 Paramaterized Model of *Chandra* PSF

I have shown that the outer *Chandra* PSF remains stable for on-axis observations, even in the event of pileup. I will now use a parametric model to describe the average PSF, which will help avoid spurious signal that may arise from statistical fluctuations in a template object.

Using the weighted exposure maps described in Section 2.2, I created surface flux profiles $I(r)$ with units of photons cm^{-2} s^{-1} pixel^{-2} for each 0.5 keV wide energy bin. No background subtraction was used so that it could be incorporated into the profile fit. Define the observationally determined PSF Ψ_o, which is subject to pileup (f_e):

$$I(r, E, f_e) = F_{ps}(E)\ \Psi_o(r, E, f_e) + B(E). \tag{2.7}$$

B represents the background surface flux, which I assume is uniform across the field of view. The PSF can be broken into two parts,

$$\Psi_o(r, E, f_e) \equiv \Psi_c(r, E, f_e) + \Psi_w(r, E) \tag{2.8}$$

the piled core, estimated with a beta profile:

$$\Psi_c(r, E, f_e) \equiv C(f_e)\left(1 + \frac{r^2}{R(f_e)^2}\right)^{-\Gamma_c} \tag{2.9}$$

where R describes the characteristic width of the core. I use a power law to describe the

wings:

$$\Psi_w(r > 1, E) \equiv W r^{-\Gamma_w}. \tag{2.10}$$

which is truncated at $r = 1$. This cut off allowed for a smooth core-wing transition in most cases; only the $0.5 - 1.5$ keV profiles contained noticeable discontinuities. The parameters r and R are in units of pixels, and C and W have units of pixels^{-2}. With increasing pileup fraction, one can generally expect flatter, dimmer cores (lower C and larger R). An attempt to derive a formula as a function of f_e is beyond the scope and capabilities of this work, so each profile is treated on a case-by-case basis.

I fit all three observations simultaneously using the formulation:

$$I_n(r) = C_n F_{ps,n} \left(1 + \frac{r^2}{R_n^2}\right)^{-\Gamma_c} + W F_{ps,n}\, r^{-\Gamma_w} + B_n \tag{2.11}$$

where the subscript n denotes values corresponding to the three observations (I-III, of Table 2.2). W and Γ_w are assumed to be constant for all objects, since the normalized PSF wing profiles are stable across all observations (Figure 2.5). The core-wing transition ($3 - 10$ pixels) is not typically subject to pileup,[7] so I also hold Γ_c fixed.

In instances of extreme pileup, such as that observed for 3C 273, a beta profile is no longer appropriate for the core. Using the `pileup_map` tool and theoretical cut off for 1% pileup,[8] I found that annuli with $r > 5$ pixels should be free of pileup. Several of

[7]The wings of non-grating ACIS observations of bright point sources, including the objects used in this study, often exhibit grade migration out to 10 pixels and $\sim 5\%$ pileup more than 20 pixels away from the point source (G04, Smith et al. 2002; Valencic et al. 2009). The observations used in this study exhibit less extended pileup because inclusion of the HETG along the line of sight significantly reduces the effective area.

[8]http://cxc.harvard.edu/csc/memos/files/Davis_pileup.pdf

the included data points span the core-wing transition, so I used the core least subject to pileup (QSO B1028+511) in order to constrain the 3C 273 fit by assigning $R_{III} = R_I$ and $C_{III} = C_{II}$. This parameter choice had little effect on on the QSO B1028+511 fit and was highly successful across all energy bins.

Table 2.4 lists the fit results for each energy bin, and Figures 2.6–2.10 plot them. As expected, cores with greater pileup are flatter ($R_{II} > R_I$) and have lower amplitudes ($C_{II} < C_I$). However pileup can artificially increase C at higher energies, since multiple lower energy events are interpreted as single events of higher energy, evidenced by the sudden increase in C_{II} for $E > 6$ keV.

Table 2.5 lists properties of the PSF fit, starting with the percent of point source flux (as measured from the HETG) distributed into the core and wings. Since the effects of pileup are folded into the definition of the observational PSF, Ψ_o does not integrate to one. Note also that the core of QSO B1028+511 exceeds 100% of the source flux at higher energies. Looking back to Figure 2.2, one can see that this should be expected, since pileup has caused the CCD measured flux to exceed the HETG flux when $E > 7$ keV.

Table 2.5 also lists the transition radius, defined as the innermost radius where $\Psi_c \leq 0.05\ \Psi_w$, and outside of which the PSF can be described by a single power law. The relatively large transition radius ($\sim$ 30 pixels) for $1.75 - 4.75$ keV bins emphasize the importance of modeling the core-wing transition. Since the surface brightness profiles are relatively unaffected by pileup for $r > 5$ pixels, a simultaneous fit to all of the objects, enforcing a single Γ_c, was highly successful. Future observers who need an accurate representation of the on-axis PSF for highly piled sources could use two power laws (with

slopes $2\Gamma_c$ and Γ_w) to model the core-wing transition or simply use the cores presented here as a best guess. Note that in Figures 2.6–2.10, a single Ψ_c fits both QSO B1028+511 and 3C 273 surprisingly well, lining up well with a few of the 3C 273 data points that were excluded (shown in grey).

Finally, the radius of 90% encircled fraction (ECF) is calculated for the PSF (independent of the true point source flux) and listed in Table 2.4. At intermediate energies, this value is alarmingly large compared to that expected from the HRMA PSF.[9] The `specextract` tool in CIAO contains the `correctpsf` option to account for this effect. The ECF results indicate that these corrections are likely underestimated, at least in the case of moderately piled sources. This also means that the α measurement in Section 2.1.2 is likely biased towards smaller values, since I extracted a low resolution spectrum from a region five pixels in radius.

By examining several bright point sources, this work is able to fit a parametric model to the *Chandra* PSF wings that appears stable across all observations. I find similar power law slopes to G04 for the asymptotic behavior of the wings ($\Gamma_w \sim 2$). However, I also find that for regions a distance $3 - 30$ pixels ($1.5'' - 15''$) from the point source center will require summing two power laws:

$$\Psi_O(r > 3) \approx C\left(\frac{r}{R}\right)^{-2\Gamma_c} + Wr^{-\Gamma_w} \tag{2.12}$$

to account for the core-wing transition. Table 2.4 can be used for these purposes.

[9] See the encircled energy fraction, Section 4.2.3 of the *Chandra* Proposer's Observing Guide

Table 2.4. Results of PSF fitting

Energy	PSF Core					PSF Wings		Background [10^{-10}]			
[keV]	C_I	C_{II}	R_I	R_{II}	Γ_c	W	Γ_w	B_I	B_{II}	B_{III}	$\bar{\chi}^2$
0.75	0.22	0.21	1.03	1.06	1.03	0.0157	2.62	20.19	20.53	18.83	1.1
1.25	0.18	0.14	0.99	1.02	0.99	0.0078	2.54	5.74	6.0	7.05	1.0
1.75	0.22	0.12	0.8	0.92	0.8	0.0016	2.05	6.52	6.82	7.7	0.8
2.25	0.21	0.13	0.81	0.92	0.81	0.0012	1.93	2.76	2.97	3.67	1.6
2.75	0.3	0.12	0.84	1.01	0.84	0.0018	2.02	2.26	2.59	3.5	0.9
3.25	0.32	0.12	0.74	0.87	0.74	0.0015	1.88	1.66	1.74	3.03	0.6
3.75	0.33	0.12	0.7	0.87	0.7	0.0008	1.64	1.34	1.46	1.73	1.0
4.25	0.24	0.11	0.92	1.07	0.92	0.0012	1.74	1.0	1.19	1.62	0.9
4.75	0.24	0.12	0.84	0.9	0.84	0.0014	1.72	0.97	0.99	1.4	0.6
5.25	0.25	0.11	0.95	1.07	0.95	0.0021	1.8	1.03	1.18	1.47	0.6
5.75	0.28	0.12	1.04	1.19	1.04	0.0028	1.88	1.25	1.52	1.68	0.6
6.25	0.5	0.21	0.76	1.18	0.76	0.0035	1.86	1.78	2.11	2.08	1.3
6.75	0.52	0.2	0.68	1.03	0.68	0.0041	1.91	2.62	3.27	3.04	0.4
7.25	0.5	0.2	1.21	1.51	1.21	0.0059	2.06	5.6	6.25	6.6	0.5
7.75	0.67	0.2	1.33	1.6	1.33	0.0083	2.3	11.78	13.03	13.11	0.7

(This page left intentionally blank)

Table 2.5. Properties of PSF fit

Energy [keV]	% Core I	% Core II	% Wings	Transition r I	Transition r II	90% ECF I	90% ECF II
0.75	43	43	7	7.5	7.8	4.7	4.7
1.25	39	31	3	13.1	12.4	3.7	4.5
1.75	44	32	3	38.1	37.4	5.0	8.2
2.25	46	34	3	41.1	39.9	6.1	11.2
2.75	60	33	4	27.5	25.3	4.1	12.5
3.25	54	28	6	27.0	23.4	11.0	61.4
3.75	54	31	9	30.0	28.1	70.2	164.3
4.25	52	31	10	18.1	17.4	59.7	134.4
4.75	49	30	12	21.9	18.7	107.1	184.7
5.25	54	31	13	14.8	13.6	81.5	156.4
5.75	59	34	13	10.5	10.1	49.9	114.8
6.25	72	72	18	12.1	18.3	67.3	66.5
6.75	64	58	17	12.4	17.7	62.6	74.8
7.25	99	61	14	6.6	7.4	8.0	27.0
7.75	130	56	9	5.7	5.8	2.1	7.1

(This page left intentionally blank)

2.4 Comparison to Previous Calibration Efforts

Section 2.1.2 described how the observation of Her X-1 used in G04 is significantly more piled up than initially presumed. G10 revisited the PSF wings with the grating-free ACIS observation of Her X-1 (ObsId 3662), which has a larger effective area and thereby contains significantly brighter wings than those imaged with HETG. The ACIS observation subtends larger angles, going out to 500″ (1000 pixels), but the extreme pileup in the core forces G10 to limit their fit to angles > 15″ (30 pixels). This work is complimentary to G10 by filling in information about the PSF core and core-wing transition.

G10 uses non-standard calibration procedures, making their models accurate for understanding the diffuse scattering wings from the HRMA. My work uses standard calibration procedures, since in practice there is no unique way to determine whether an X-ray event comes from mirror scattering, extended emission, or background; each technically requires a separate treatment of the effective area. However, G10 acknowledged this problem and provided separate fits for data normalized by more standard calibration products of `mkexpmap`. Using wider bins (ΔE = 1 keV), G10 fit the extended PSF wings (30 − 1000 pixels) with a power law modified by an exponential term:

$$\Psi(r) \propto r^{-\gamma} \exp(-r/c) \tag{2.13}$$

where $c \sim 2000$ pixels. The Γ_w results listed in Table 2.4 agree roughly with the γ values listed in Table D.1 of G10 for $E > 3$ keV.

G10 experiences difficulty finding the proper normalization for the PSF core, because

pileup is so severe. They use the CCD transfer streak to extract a nearly pileup-free spectrum, acknowledging that calibration for this procedure is uncertain. This work uses the high resolution HETG extract spectrum, which is pileup free. If a PSF wing model is needed beyond 200 pixels (100″), I suggest using the amplitudes in Table 2.4, coupled with the G10 models. The amplitudes from Table D.1 of G10 will require modification to account for units and systematic errors from the transfer streak spectrum.

2.5 Summary and Conclusions

Detector pileup, which occurs when two or more X-ray photons hit the same region of the CCD, is a particularly difficult problem for determining the *Chandra* point spread function. Moderately piled sources will exhibit a flatter PSF core and will be erroneously bright at higher energy. This makes it difficult to properly normalize a PSF so that it can be used to extract extended features of low surface brightness from other observations.

I examined three HETG observations of bright point sources with well behaved spectra in order to observationally determine the pileup fraction. Taking the HETG dispersed spectrum as a measure of the true point source flux, I fit the CCD spectrum extracted from the zeroth order image using the `jdpileup` model (Davis 2001). This yielded a measurement for the essential model parameter, α, the probability that a piled event receives a passing grade. The resulting trends outlined in Table 2.2 – that objects with smaller pileup fractions (f_e) also exhibited smaller values of α – is not intuitive. One has to remember that when a large fraction of the piled events are being rejected, the observed pileup fraction f_e, defined as the number of *observed* events that were subject

to pileup, is relatively low.

Simulated data (ChaRT and Marx) under-predicts the brightness of PSF wings by 20-80%, so templates made from sources with relatively dust free sightlines offer an alternative. I examined surface brightness templates, normalized by the true point source flux and effective area, as a means of reconstructing the PSF for other observations. The template technique outlined here is used in Chapter 3, and other publications have also used 3C 273 and Her X-1 as templates (e.g. Smith et al. 2002; Valencic et al. 2009; Mao et al. 2014). The cores from each normalized profile ($r < 3$ pixels) vary, but the wings agree within 1-2σ, showing that they are stable across observations (Figure 2.5). Due to a lack of signal, QSO B1028+511 does not make a particularly good PSF template, but the HETG image of 3C 273 has enough signal to cover the wings out to 200 pixels.

Parametric models of the PSF provide a useful method for predicting the wing brightness reduces errors from the natural statistical variation that comes with using a single object as a template. I used a beta function to describe the PSF core (Equation 2.9) and a power law to describe the PSF wings (Equation 2.10), simultaneously fitting the surface flux profiles of all three *Chandra* observations. This method reduces uncertainty as compared to examination of a single object, which could lack signal in certain energy or radial bins, thereby ensuring that the average behavior of the PSF wings are being captured. The wing amplitude, power law slope, and asymptotic slope of the core are assumed to be constant across all observations. Despite fluctuations in the core brightness and width due to pileup, the values from Table 2.4 can be used to model the PSF wings and core-wing transition (Equation 2.12) for other on-axis *Chandra* HETG observations.

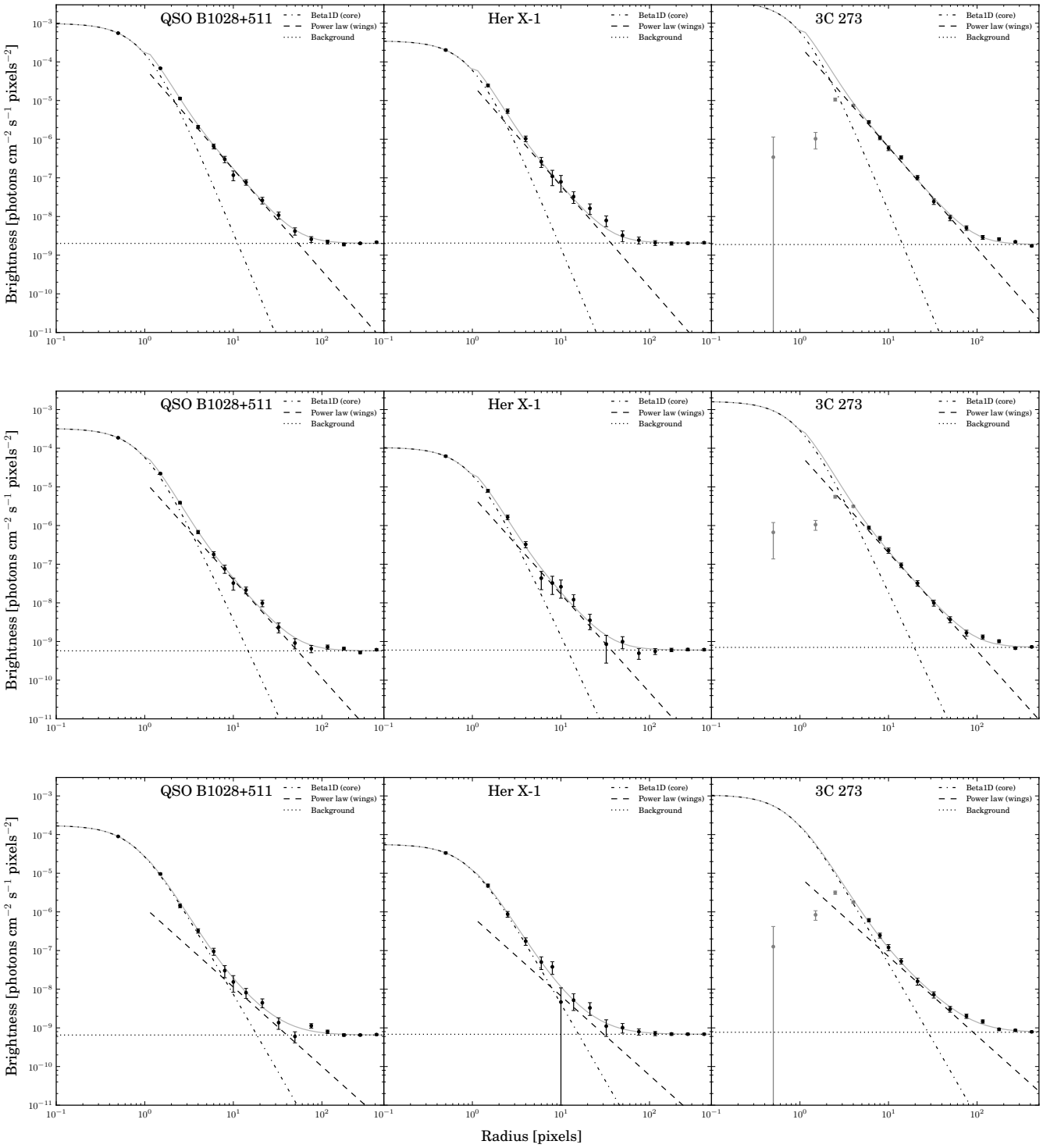

Figure 2.6 Surface flux profiles and fits for 0.75 keV (*top*), 1.25 keV (*middle*), and 1.75 keV (*bottom*). The grey 3C 273 data points, shown here for reference, were excluded from the fit.

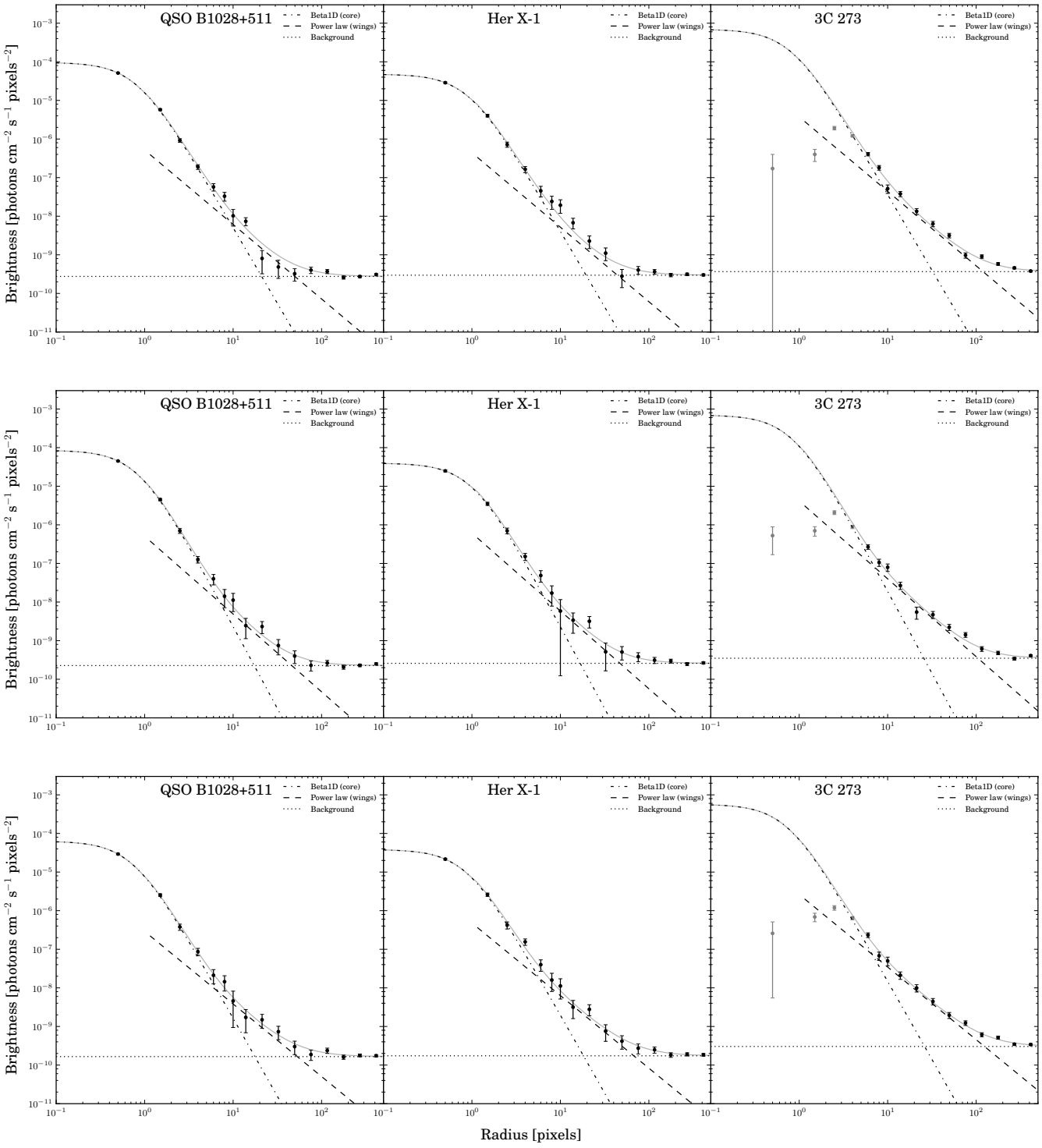

Figure 2.7 Surface flux profiles and fits for 2.25 keV (*top*), 2.75 keV (*middle*), and 3.25 keV (*bottom*). The grey 3C 273 data points, shown here for reference, were excluded from the fit.

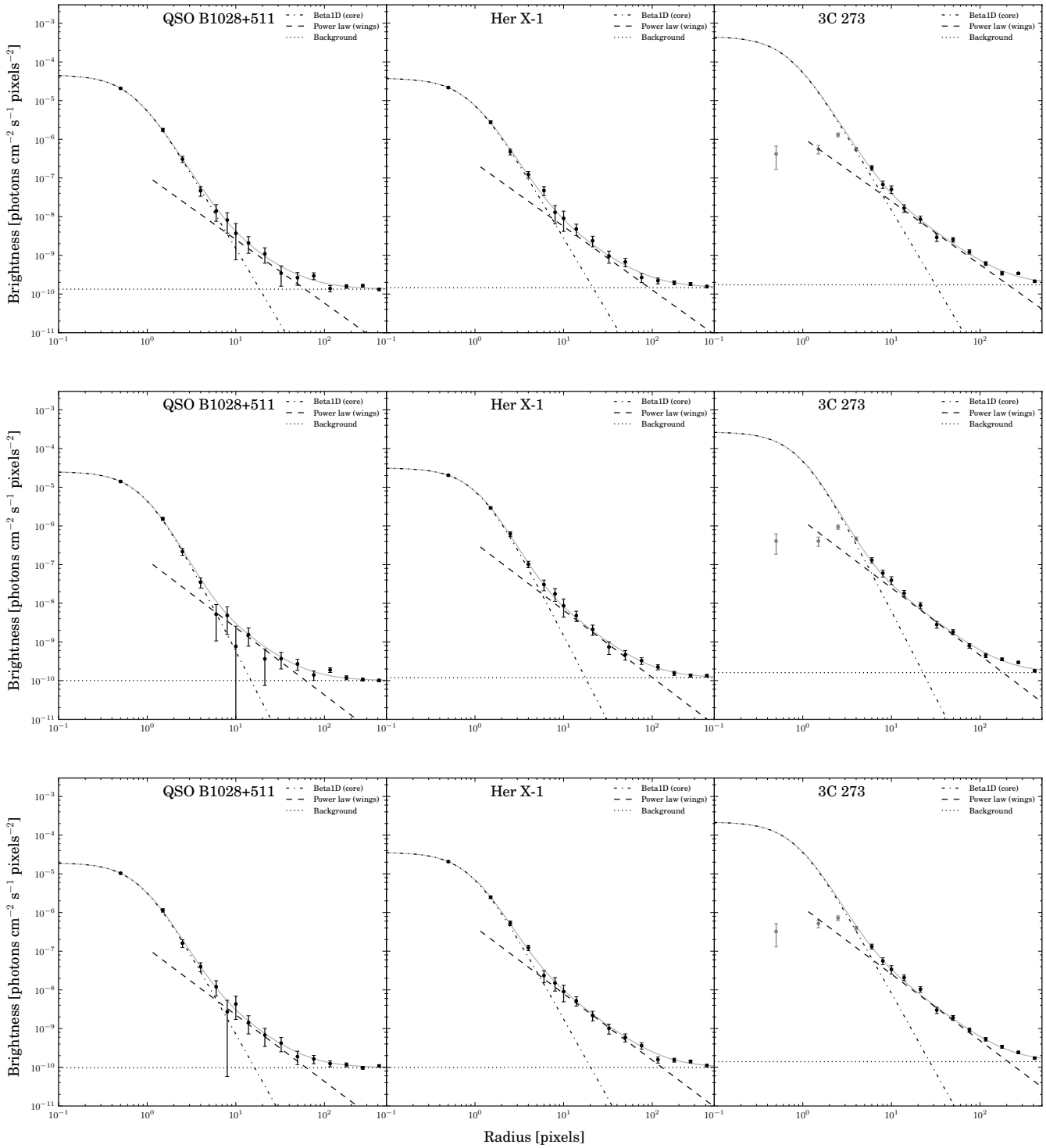

Figure 2.8 Surface flux profiles and fits for 3.75 keV (*top*), 4.25 keV (*middle*), and 4.75 keV (*bottom*). The grey 3C 273 data points, shown here for reference, were excluded from the fit.

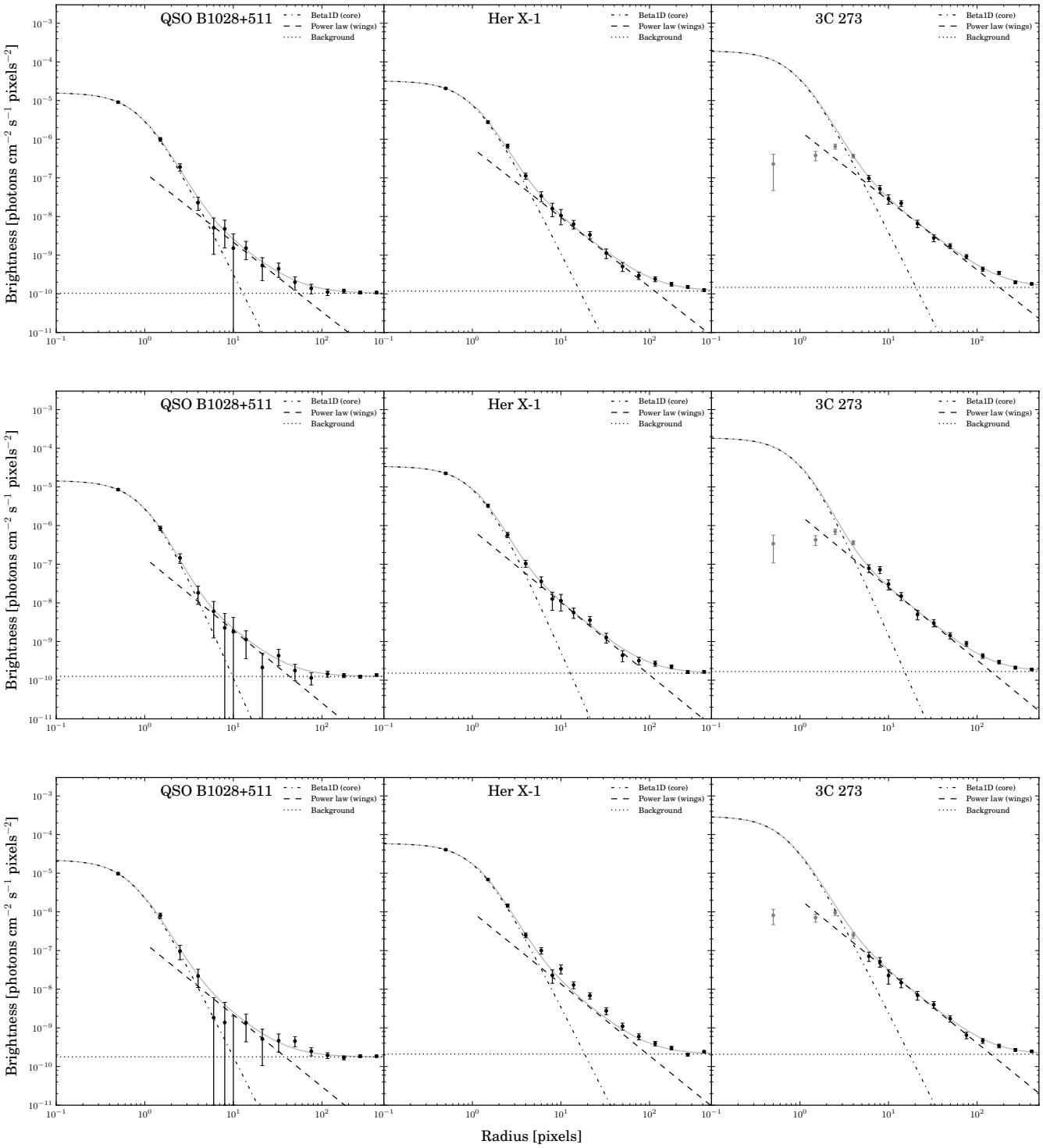

Figure 2.9 Surface flux profiles and fits for 5.25 keV (*top*), 5.75 keV (*middle*), and 6.25 keV (*bottom*). The grey 3C 273 data points, shown here for reference, were excluded from the fit.

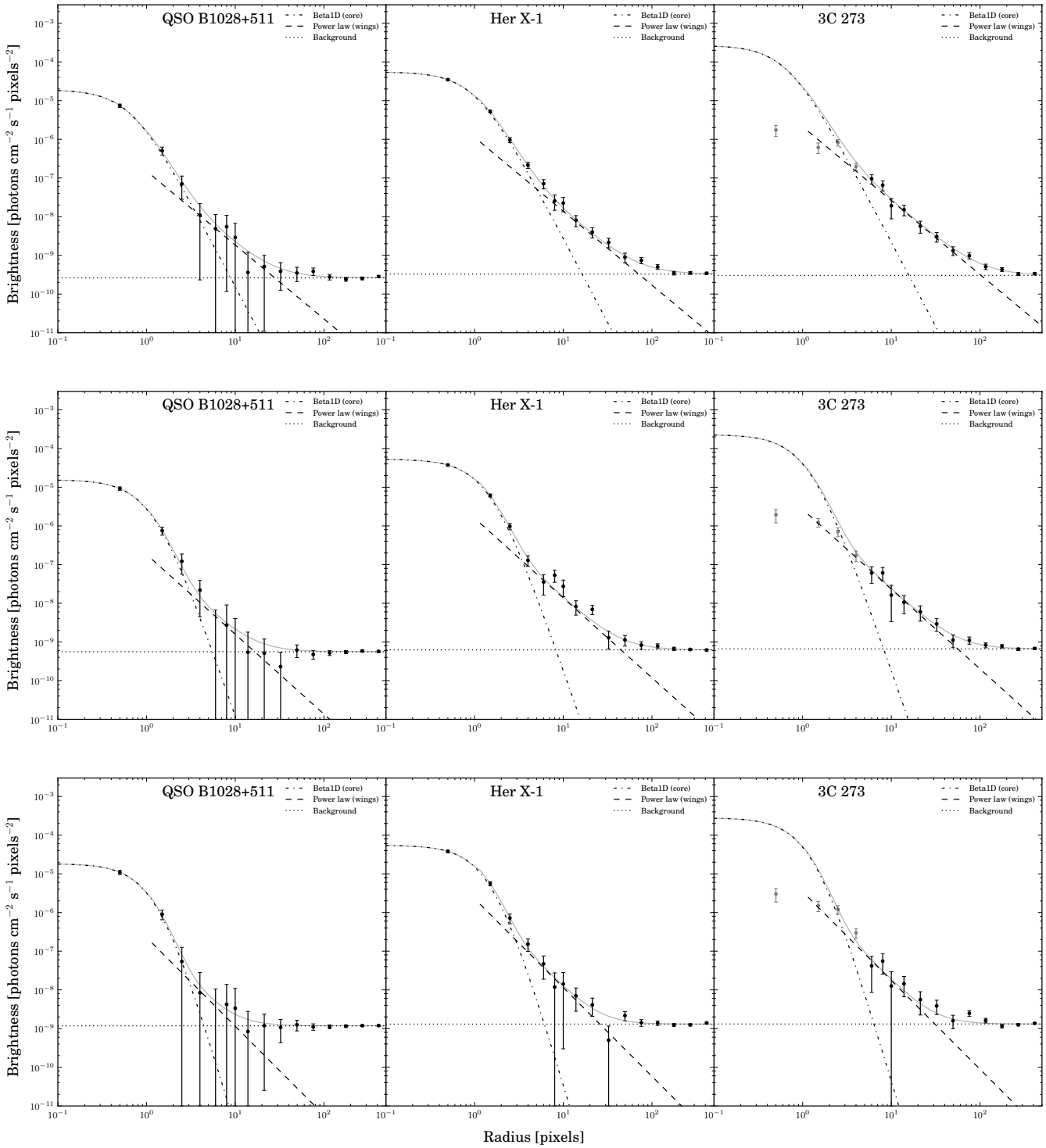

Figure 2.10 Surface flux profiles and fits for 6.75 keV (*top*), 7.25 keV (*middle*), and 7.75 keV (*bottom*). The grey 3C 273 data points, shown here for reference, were excluded from the fit.

Chapter 3

The Dust Scattering Halo of Cygnus X-3

One of the brightest X-ray scattering halos available in the *Chandra* archive is associated with the high mass X-ray binary (HMXB) Cygnus X-3. Section 3.1 describes the environment along the Cyg X-3 sight line. The observation and PSF subtraction method is described in Section 3.2. A Bayesian approach to fitting the dust grain size distribution is described in Section 3.3, using two models for the spatial distribution of dust along the line of sight. In one case I assume dust is uniformly distributed; in the other I model the halo with two infinitesimally thin dust screens. Section 3.4 presents flux measurements and model residuals from energy resolved scattering halos. Section 3.5 shows how an ISM dust to-gas mass ratio can be calculated from X-ray spectroscopic data. In Section 4.6, I discuss the model implications and compare the results to other papers that study ISM on the Cyg X-3 sight line.

3.1 ISM column

Cyg X-3 is located in the galactic plane at $(l, b) = (79.8, +00.7)$. At a distance of 7-13 kpc from the Sun (Dickey 1983; Predehl et al. 2000), the HMXB is located behind one or two spiral arms of the Milky Way – Perseus and the outer arm (e.g. Russeil 2003). The Cyg X-3 sightline also passes through the star forming Cygnus X region, which offers a complex laboratory for ISM dust physics.

Radio surveys give a lower limit to the neutral hydrogen column near the Galactic plane, $N_{\rm HI} \gtrsim 10^{22}$ cm^{-2} (Kalberla et al. 2005). However, Cyg X-3 is situated behind the massive star cluster Cyg OB2 and its associated molecular clouds (Knödlseder 2003). The Milky Way CO survey shows that the Cyg X-3 sightline is particularly patchy, but contains a total proton density $N_{\rm H} \approx 10^{22}$ cm^{-2} in the form of molecular hydrogen (Dame et al. 2001). In sum, radio survey in the direction of Cyg X-3 give a lower limit to the total ISM column: $N_{\rm H} > 2 \times 10^{22}$ cm^{-2}.

X-ray spectroscopy offers another means to measure the total ISM column. Absorption by neutral hydrogen via the photoelectric effect dominates below 1 keV, but the metal content of the ISM accounts for a considerable fraction of the total absorption above 1 keV (Wilms et al. 2000). Predehl & Schmitt (1995) used ROSAT observations of Cyg X-3 to estimate $N_{\rm H} \sim 3 - 4 \times 10^{22}$ cm^{-2}, which is consistent with the above radio surveys. However, the absorption measurement is highly dependent on the source model for soft X-ray emission. I will discuss this in the context of the high resolution HETG spectrum of Cyg X-3, which covers a wider bandpass than ROSAT (Section 4.6).

3.2 Observation

With 0.5″ per pixel resolution and a low background, *Chandra* is the best X-ray observatory available for imaging dust scattering halos. ObsId 6601 is the longest observation (50 ks) of Cygnus X-3 taken with the High Energy Transmission Grating (HETG), which also provides 1-2 eV spectral resolution. The High Resolution Mirror Assembly (HRMA) on *Chandra* focuses about 90% of the X-ray light into a few pixel (2″) region. The point spread function (PSF) is composed of two parts: the core, where the majority of light is focused, and the wings, where light is spread diffusely due to scattering off of fine surface features in the mirror. Correctly subtracting the PSF from the image is of utmost importance for determining halo brightness, which is on the order of the PSF wing brightness. I will use the techniques set forth in Section 2.2 to do so.

To get an accurate shape of the PSF wings, I chose 3C 273, which has a smooth power law spectrum and very low ISM column ($N_H \sim 10^{20}$ cm^{-2}, inferred from Schlegel et al. 1998). I built a PSF template from ObsId 459, a 39 ks exposure of 3C 273 imaged with HETG[1]. A surface brightness profile of the zeroth order image was made with 0.5 keV wide bins between 1-6 keV. I created weighted exposure maps from a power law fit to the HETG spectrum, using 0.1 keV bins. The average background level for each image was estimated from a region of the chip around 5.5′ from 3C273. Each surface brightness profile was exposure map corrected using `dmextract`, background subtracted, then normalized by the flux of 3C273 as measured by the HETG fit. To construct the PSF for Cyg X-3, each template was scaled by the grating dispersed flux of Cyg X-3 for the respective bin.

[1]3C 273 has a small jet feature, which was masked out of the surface brightness profile.

The surface brightness profile of Cyg X-3 was also corrected with a weighted exposure map created from a *diskpn* (Gierliński et al. 1999) plus an ISM extinction model. The typical 0.5-7 keV background[2] for a 50 ks observation is 0.02 counts pix^{-2}, two orders of magnitude below the dimmest portion of the surface brightness profile. Since the majority of light around Cyg X-3 likely comes from X-ray scattering, I scaled up the background surface brightness from ObsId 459 to match the exposure time of ObsId 6601 and added it to the PSF template.

There is a Bok globule located 16″ from Cyg X-3, observed from X-ray scattering (McCollough et al. 2013). A 3″ by 4.5″ region covering the globule contains 7120 counts, which accounts for 20-30% of the total brightness at that radius. I removed the globule from the measurement, because the halo model assumes azimuthal symmetry.

The scattering halo measured from the zeroth order image might also be contaminated from the first order halo dispersed by the HETG. To test this, I extracted a radial surface brightness profile from a rectangular region oriented in the MEG dispersion direction. I found significant contamination from the MEG first order scattering halo in regions > 100 pixels away from the point source center. There is plenty of signal in the outer edges of the halo, which are covered by annuli of larger surface area. I therefore chose to confine the surface brightness profiles to a rectangular region perpendicular to both the MEG and HEG arms.[3] Utilizing this region reduced the outermost profile data point by 4σ and significantly altered some of the fit results (e.g. $a_{\rm max}$ in Table 3.1 increased by 50%), demonstrating how remarkably sensitive X-ray scattering is to grain size distributions.

[2] *Chandra* Proposer's Observing Guide, Table 6.10, http://cxc.harvard.edu/proposer/POG/
[3] Surface brightness measurements with annuli $r < 40$ pixels receive full azimuthal coverage.

Figure 3.1 shows the residual 1-6 keV surface brightness profile of Cyg X-3, extracted from the region described above. There is a great deal of systematic error in the PSF core, because the zeroth order image of Cyg X-3 is much more piled up than 3C 273, which does not have a hollowed out core. I threw out data points from bins where the PSF template exceeded the observed surface brightness and kept data points with a signal to noise > 1. ObsId 6601 used only half of the CCD chip, limiting the measurement to the inner regions of the dust scattering halo, 5 – 100''.

3.3 Fit to 1-6 keV halo profile

It has been shown that a power law distribution ($N_d \propto a^{-p}$ with $p \approx 3.5$) of graphite and silicate grains reproduce extinction curves in the UV and optical (Mathis et al. 1977, hereafter MRN). For the RG-Drude scattering regime, the composition of the grains is not very important because they are approximated as spheres of free electrons. I use the average grain density $\rho = 3$ g cm^{-3} (Draine 2011).

Updated grain size distributions beyond the simple power law regime have been developed to better reproduce infrared and microwave emission features. Weingartner & Draine (2001, hereafter WD01) produced a distribution that mainly modified the lower end of the grain size distribution, which shines brightest in the infrared. Zubko et al. (2004, hereafter ZDA) did the same, but aimed to preserve elemental abundance constraints. They developed a series of models with varying mixtures of silicate, graphite, amorphous carbon, PAH, and composite material sometimes referred to as "fluffy" dust. Several authors have shown that ZDA models fit X-ray scattering halos comparatively

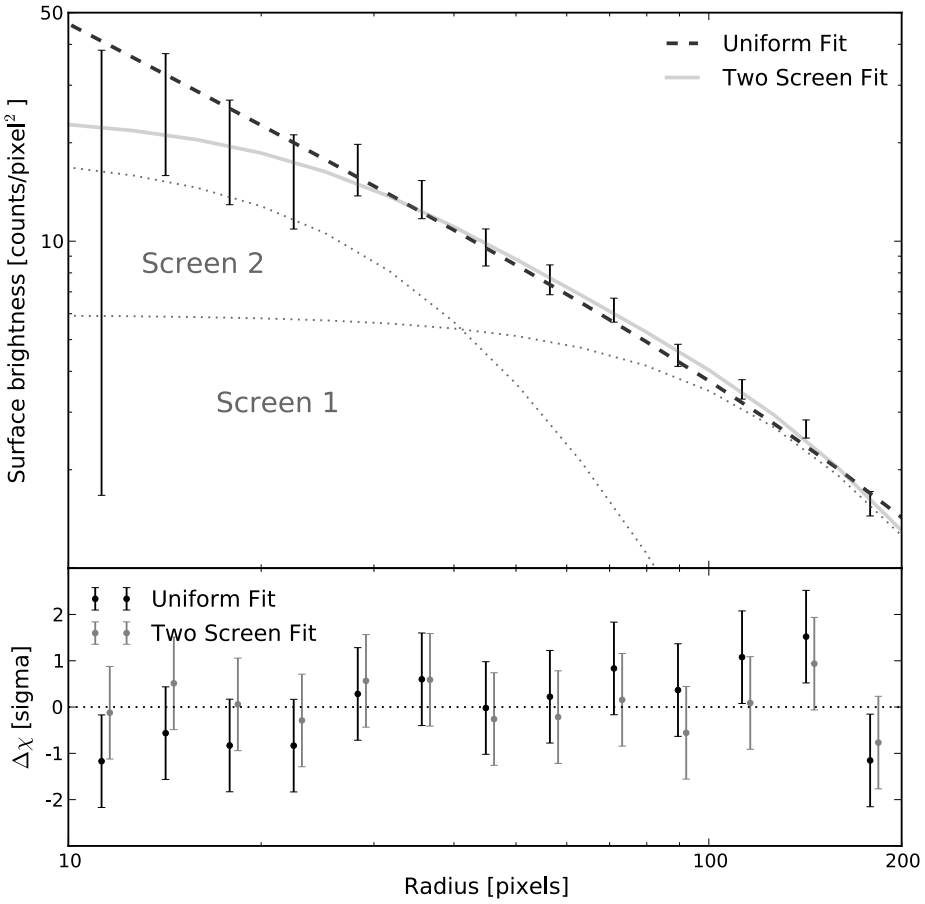

Figure 3.1 *Top:* ObsId 6601 surface brightness profile (1-6 keV) after subtracting the PSF template. One pixel corresponds to 0.5″. The best *emcee* fits for dust uniformly distributed along the line of sight (dark dashed line) and for dust contained in two screens (light dotted and solid lines) are overlaid. *Bottom:* The residuals are plotted in units of sigma. The two screen fit residuals are offset horizontally to aid visibility.

well or slightly better than MRN and WD01 size distributions (Smith et al. 2006; Smith 2008; Valencic et al. 2009). However, the best fitting ZDA models tended to be BARE-GR and BARE-AC, which are more similar to MRN than the ZDA COMP (fluffy grain) models. Moving forward with the simplifying assumption that a power law is a good approximation for the dust grain size distribution, I fix the low end of the distribution at 0.005 μm and fit for $a_{\rm max}$ and p.

Using $N_d \propto a^{-p}$ also allows for an analytic solution to the integral for scattering halo

intensity (Equation 1.8). For dust distributed uniformly along the line of sight ($\xi = 1$),

$$I_h(\alpha, E) = \frac{F_a}{\sqrt{8\pi}} \frac{\tau_{\rm sca}}{\alpha \tilde{\sigma}_0(E)} \frac{G_u(a, p, \alpha, E)}{G_p(a, p)} \tag{3.1}$$

where $\tilde{\sigma}_0(E) = 1.04' \, E_{\rm keV}^{-1}$, G_p is an integral over a power law, and G_u is a function of erf and incomplete gamma functions as defined in Section 1.4. For an infinitesimally thin dust screen, where $\xi = \delta(x - x_s)$,

$$I_h(\alpha, E) = \frac{F_a}{x_s^2} \frac{\tau_{\rm sca}}{2\pi \tilde{\sigma}_0^2(E)} \frac{G_s(a, p, \alpha, x_s, E)}{G_p(a, p)} \tag{3.2}$$

which is also described in Section 1.4. Screens produce a flat surface brightness profile, and a uniform distribution produces a cuspy profile.

I use the publicly available MCMC code *emcee* to explore the parameter space in a Bayesian analysis of possible halo fits (Foreman-Mackey et al. 2013). At a fixed energy, the dust grain distribution parameters $a_{\rm max}$ and p mainly affect the scattering halo shape. The optical depth to scattering controls the halo normalization, which scales with the total dust mass column, $\tau_{\rm sca} = \kappa_{\rm sca}(a, p) M_d$.

3.3.1 Uniform fit

I start with uniformly distributed dust because it has the least number of free parameters and will most likely match the shape of the halo profile, which is cuspy. Guess values of $M_d = 5 \times 10^{-4}$ g cm^{-2}, $a_{\rm max} = 0.2$ μm, and $p = 3.5$ yield a reasonable fit by eye.[4]

[4]The initial dust mass column was estimated using $N_{\rm H} = 3.5 \times 10^{22}$ cm^{-2} (Predehl & Schmitt 1995) and assuming a dust-to-gas mass ratio typical of the Milky Way (0.009, Draine 2011).

Table 3.1. Uniform fit to dust scattering halo (1-6 keV)

	Best	Median	(1σ C.I.)	Units
M_d :	6.7	8.3	(5.8, 13)	10^{-4} g cm^{-2}
$a_{\rm max}$:	0.13	0.14	(0.12, 0.17)	μm
p :	2.9	3.5	(3.0, 3.9)	
$\tau_{\rm sca}E^2$:	2.4	2.4	(2.2, 2.8)	keV^{-2}

I assigned uniform priors to $\log(M_d)$ from -11.8 to -1.8 cgs[5] and $a_{\rm max}$ from 0.01 – 0.5 μm. I found that, if p was allowed to take on large values, the halo fit solution becomes highly degenerate for grain sizes above 0.3 μm. Larger $a_{\rm max}$ values require increasingly large dust column and $p > 5$, so that the small end of the size distribution dominates. To suppress the uninformative degenerate solutions, I assigned a Gaussian prior to p with mean 3.5 and standard deviation 0.5.

I used 100 walkers in *emcee* to obtain 900 independent samples of the posterior distribution, shown in Figure 3.2. The bottom row of histograms shows the optical depth, calculated from each sample of the posterior distribution. The vertical dashed lines indicate the 16th, 50th, and 84th quantiles – corresponding to the median and 1σ confidence interval. Two-dimensional histograms comparing each parameter against the others illustrates that they are highly covariant.

Figure 3.1 plots the best model halo, corresponding to the smallest χ^2, obtained from 100 samples of the posterior distribution. The best fit, median fit, and 1σ confidence intervals are listed in Table 3.1. The covariant nature of the posterior distribution explains why the median parameters listed in Table 3.1 don't give the best possible fit.

[5]Corresponding approximately to $14 \leq \log(N_{\rm H}) \leq 24$.

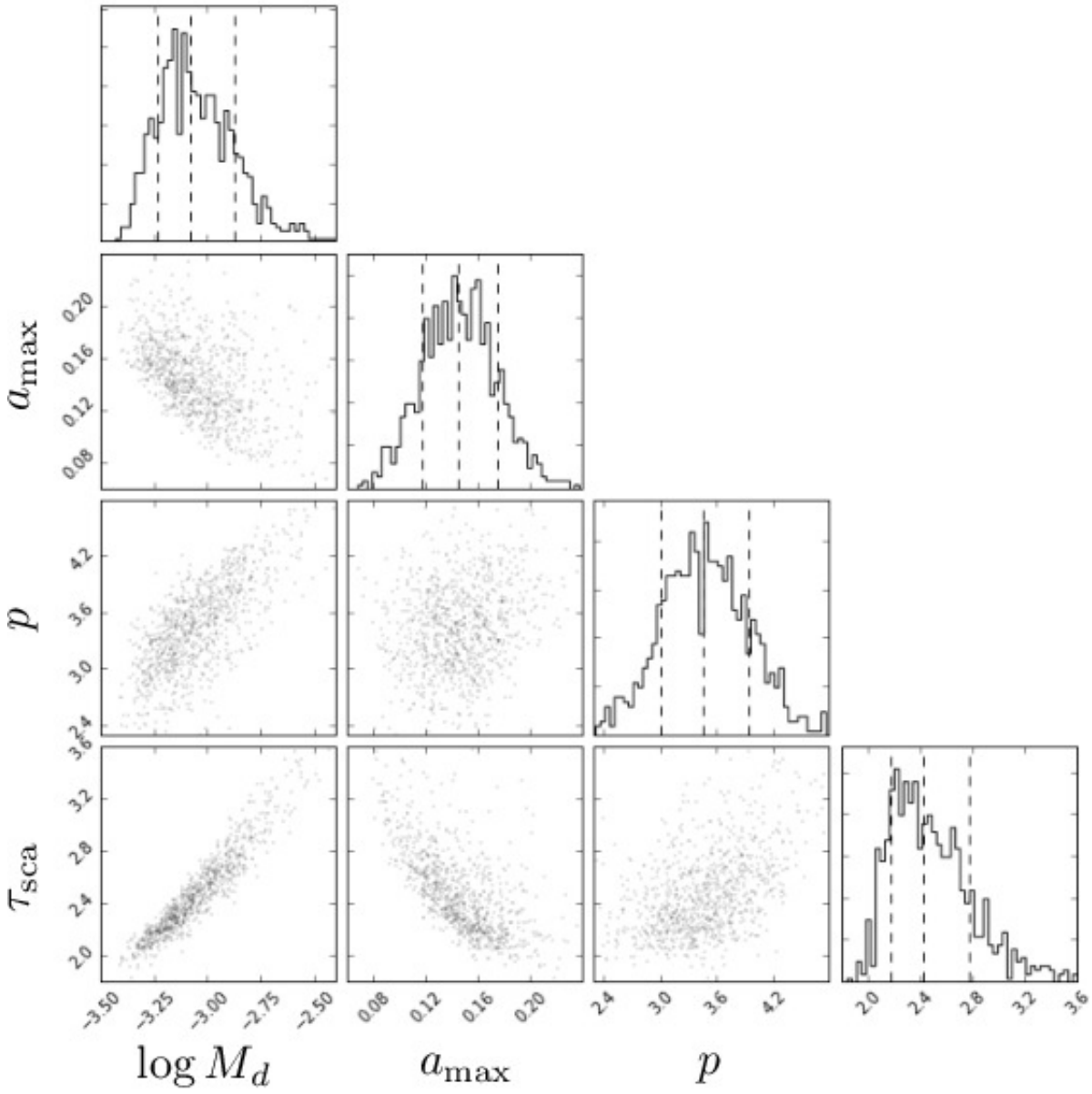

Figure 3.2 The posterior distribution from *emcee* is plotted with two-dimensional histograms comparing each pair of free parameters (M_d, p, and $a_{\rm max}$) and each fits' $\tau_{\rm sca}$. There is particularly strong covariance between power-law exponent p and dust mass M_d, making $\tau_{\rm sca}$ covariant with both these parameters. The vertical dashed lines in each one-dimensional histogram mark the median and 1σ confidence interval for each parameter.

Table 3.2. Two screen fit to dust scattering halo (1-6 keV)

	Best	Median	(1σ C.I.)	Units
Screen 1				
x_1 :	0.28	0.44	(0.34, 0.54)	
M_{d1} :	5.6	4.5	(2.7, 8.0)	10^{-4} g cm^{-2}
Screen 2				
x_2 :	0.07	0.11	(0.08, 0.15)	
M_{d2} :	1.2	1.1	(0.5, 4.0)	10^{-4} g cm^{-2}
Dust distribution				
$a_{\max}$:	0.12	0.21	(0.13, 0.29)	μm
p :	3.3	3.6	(3.1, 4.3)	
Total M_d :	6.8	5.6	(3.7, 10)	10^{-4} g cm^{-2}
$\tau_{\rm sca}E^2$:	1.9	1.9	(1.7, 2.4)	keV^2

3.3.2 Scattering from Dust Screens

X-ray scattering can probe galactic structure in the direction of Cyg X-3, which might include features such as those associated with Cyg OB2 or Galactic spiral arms (§3.1). When applying the infinitesimally thin screen model, it should be kept in mind that while the total integrated halo flux will be fixed according to the optical depth of the screen, the surface brightness profile will vary according to the screen's position. For screens closer to the observer (large x, see Figure 1.4), the scattered flux will be spread over a large area, reducing the overall surface brightness profile. When a screen is close to the X-ray source (small x), the halo surface brightness profile will be more compact and thus brighter at small observation angles.

Taking 9 kpc as the best estimate for the distance to Cyg X-3, I expect the Perseus arm, about 5 kpc away, to correspond to a screen with $x_s \approx 0.4$. The outer spiral arm, if in the foreground of Cyg X-3, will be at $x_s \leq 0.1$ and would therefore contribute most to

the surface brightness profile. The Cyg OB2 association, 1.7 kpc away (Knödlseder 2000), corresponds to $x_s \approx 0.8$ and would contribute to the outermost portion of the profile. However, an MRN distribution of dust associated with the Cyg OB2 region would create a halo intensity ~ 1 count per pixel^2, which is too dim. I therefore chose to fit the dust scattering surface brightness profile with a model containing only two screens.

In the optically thin regime, the intensity of the halo from each screen can simply be added to get the total observed halo. I ran *emcee* with a six parameter model containing two screen positions (x_1, x_2) and their respective dust mass (M_{d1}, M_{d2}), assuming the same dust grain distribution for both screens ($a_{\rm max}$, p).

To model the Perseus arm, I chose a Gaussian prior with mean 0.4 and standard deviation 0.1 and applied it to x_1. To get at the inner portion of the scattering halo, I applied a Gaussian prior to x_2 with mean 0.05 and standard deviation 0.1, a screen most likely associated with the outer spiral arm. The spread in the Gaussian distributions were chosen to account roughly for the uncertainty in the distance to Cyg X-3, 9^{+4}_{-2} kpc (Predehl et al. 2000). The prior distributions on x_1 and x_2 are truncated at 0.23, so that x_1 always represents the screen closer to the observer. The priors on M_d, $a_{\rm max}$, and p are identical to those used in Section 3.3.1.

Figure 3.1 shows the best fit (*solid grey line*) out of 100 samples drawn from the posterior distribution. The relative contribution of each screen is also plotted (*dotted grey lines*). Table 3.2 lists the best, median, and 1σ confidence intervals for each parameter in the two screen fit, including the total dust mass and scattering optical depth.

3.3.3 Multiple scattering

The surface brightness profile models assume an optically thin ISM so that photons only scatter once, but the fits show that the Cyg X-3 sight line is optically thick to dust scattering. Since the spectral energy distribution (SED) of Cyg X-3 is highly absorbed, the point source flux peaks around 3 keV, where $\tau \sim 0.2$. However, weighted with the SED, around 60% of the total scattered light to come from $E < 3$ keV.

The model halo flux (F_h), calculated from the observed point source flux (F_{ps}), is described by the following relation:

$$\frac{F_h}{F_{ps}} \equiv \frac{F_a\,(1 - e^{-\tau_{\rm sca}})}{F_a\,e^{-\tau_{\rm sca}}} = e^{\tau_{\rm sca}} - 1 \tag{3.3}$$

where F_a is the apparent flux of the source, including the effects of ISM absorption. A simple Taylor expansion estimates the fraction of photons that will scatter twice ($\tau^2_{\rm sca}/2$) or three times ($\tau^3_{\rm sca}/6$). Using an upper limit of $\tau_{\rm sca} = 3.0$, less than 10% (5%) of the photons with $E > 2.5$ keV ($E > 3$ keV) to undergo multiple scattering events. Weighted with the SED, around 20% (5%) of photons in the 1-2.5 keV energy range scatter twice (three times).

Multiple scattering effects increase the brightness of a scattering halo with respect to the central point source as described in Equation 3.3. The second and higher order scattering halos contribute to the intensity at larger angles, significantly altering the shape of the outer halo when $\tau_{\rm sca} > 1$ (see Fig 7, Mathis & Lee 1991). The next section evaluates the impact of multiple scattering on the preceding fits by examining the energy resolved scattering halos.

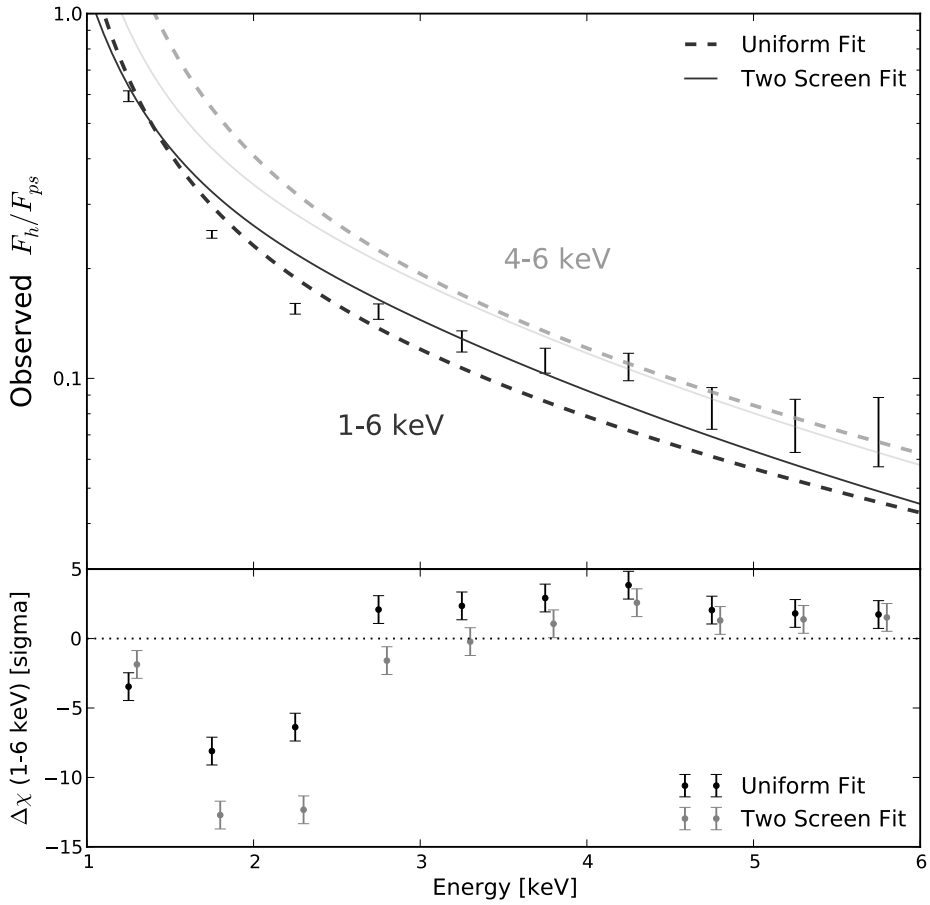

Figure 3.3 *Top:* The observed ratio of total integrated halo flux to point source flux. The values predicted fits to the 1-6 keV halo (*dark lines*) appear to do better than fits to the 4-6 keV halo (*light lines*). These curves take into account the fact that only a fraction f_{cap} of the scattering halo falls within the field of view of ObsId 6601, but do not correct for multiple scattering. *Bottom:* The 1-6 keV model residuals are plotted in units of sigma.

3.4 Energy Resolved Scattering Halos

3.4.1 Energy Resolved Halo Flux

I calculated F_h by summing the flux in each annular region, extracted from 0.5 keV binned images of ObsId 6601 using the same PSF and background subtraction methods described in Section 3.2. The point source flux F_{ps} was integrated from the fit to the HETG spectrum. Figure 3.3 plots the ratio F_h/F_{ps} as a function of energy. Since the field of view for ObsId

6601 is limited, a significant portion of the total halo flux is missing. I used the scattering halo surface brightness models to estimate the fraction of halo flux captured in the $5'' - 100''$ region covered by Figure 3.1:

$$f_{cap}(E) \equiv \frac{\int_{5''}^{100''} I_h(\alpha, E)\, 2\pi\alpha\, d\alpha}{F_a \tau_{\rm sca}} \tag{3.4}$$

which, by necessity, assumes an optically thin medium. I found $f_{\rm cap} \sim 0.2 - 0.8$. Multiplying this with Equation 3.3, Figure 3.3 shows how predictions for F_h/F_{ps} from the 1-6 keV models (dark lines) compare to the observed values.

It is surprising that the 1-6 keV models follow the shape of the F_h/F_{ps} curve until $E < 2.5$ keV. The residuals are shown in Figure 3.3 (bottom), revealing a marked decrease at 1.75 and 2.25 keV. The decreased halo brightness at these energies decreases the overall normalization, which explains why the $E > 2.5$ keV residuals are flat, but systematically offset. It is also curious that the trend causing the $E < 2.5$ keV points to turn away from the model does not continue at the lowest energy bin (1.25 keV). Pileup in the MEG arm, lack of signal, or the steep spectral slope at the lower end of the SED likely caused a slightly underestimate of F_{ps} in the lowest energy bin. I remeasured the photon flux using a power law fit to the 1.0-1.5 keV spectrum, finding a value 20% lower than the *diskpn* plus extinction model (§3.2). The 1.5-2 keV and 2-2.5 keV flux values were accurate to within a few percent. Thus the relatively good alignment of the 1.25 keV data point in Figure 3.3 with the 1-6 keV models is likely a coincidence brought about by systematic errors in the SED fitting.

Considering the optical depths implied by the 1-6 keV fit, the assumption of single

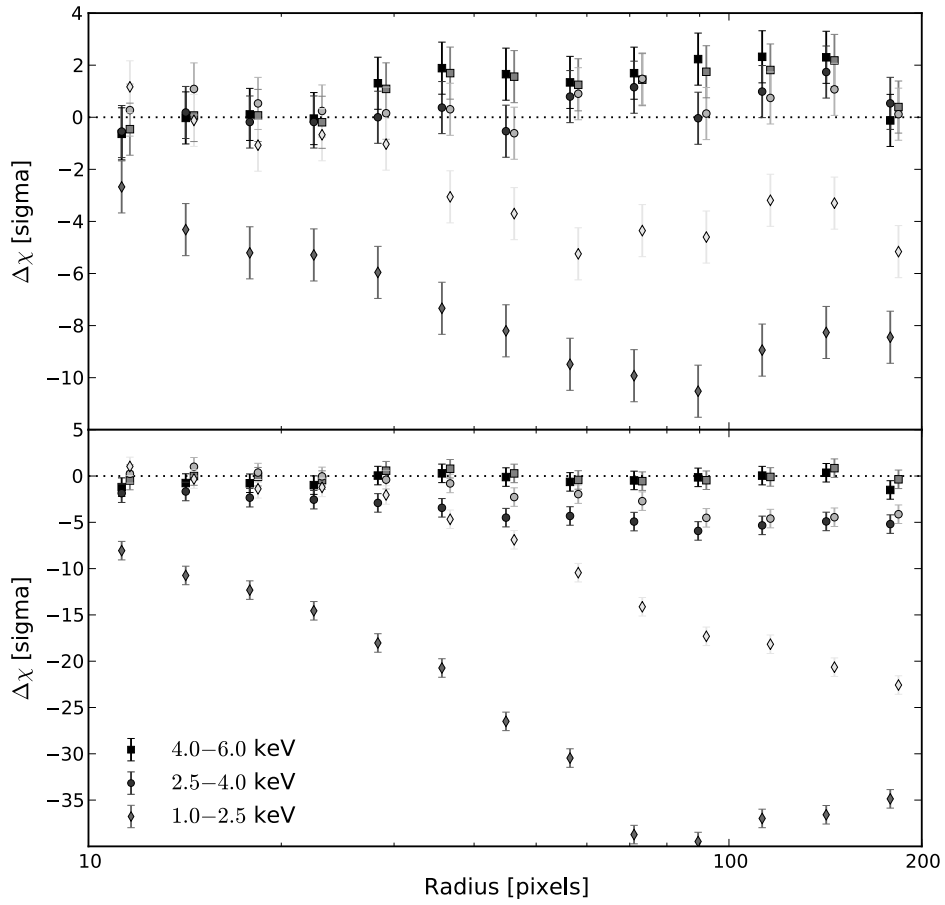

Figure 3.4 *Top:* The scattering halo residuals from three energy bins are plotted for the uniform fit in Section 3.3.1 (*darker points*) and two screen fit from Section 3.2 *lighter points*). *Bottom:* Residuals from the uniform and two screen fit obtained from the 4-6 keV scattering halo, extrapolated to lower energy bins.

scattering should only be applied at higher energies (Section 3.3.3). I fit the 4-6 keV scattering halo with a uniform and two screen model as described in Sections 3.3.1 and 3.3.2. The 4-6 keV models (Figure 3.3, light lines) significantly over-predict F_h/F_{ps} for $E < 4$ keV.

Without more detailed calculations, it is difficult to judge how multiple scattering should affect the predicted curve. Higher order scattering halos would increase the observed flux, but their profiles are more extended, reducing f_{cap}.

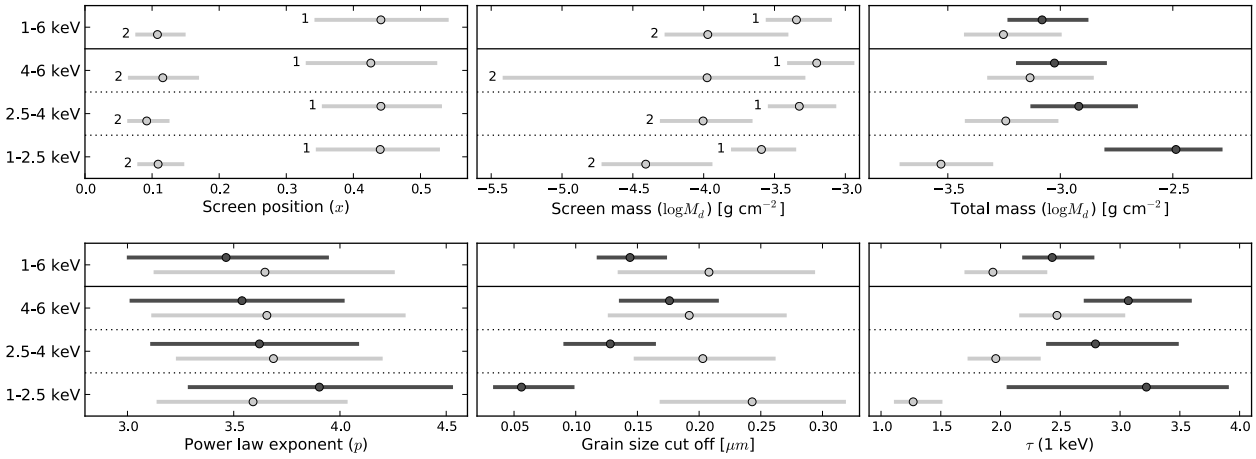

Figure 3.5 The posterior distribution medians (*circles*) and 1σ confidence intervals (*solid lines*) are plotted to compare the uniform (*dark*) and two screen (*light*) model fits from each energy resolved halo.

3.4.2 Energy Resolved Halo Residuals

I split the image of Cyg X-3 into three broad energy bins expected to exhibit comparable levels of scattering halo brightness: 1-2.5 keV, 2.5-4 keV, and 4-6 keV. Figure 3.4 (top) shows the residuals for the 1-6 keV fits from each energy resolved halo. The 1-2.5 keV halo is offset by $8 - 12\sigma$, and the model fit is increasingly worse towards the edges of the surface brightness profile. My models fit the data much better when $E > 2.5$ keV, though there is still systematic offset when $r > 30$ pixels.

Figure 3.4 (bottom) shows that when I extrapolate the 4-6 keV fit to the remaining energy resolved halos, the residuals are much worse. Note however that *both* the 1-6 keV and 4-6 keV two screen models fit appreciably well across all energy bins in the region $r < 30$ pixels. This lends credibility to the model of an optically thin screen close to Cyg X-3, which is responsible for the inner portion of the scattering halo.

The decreased brightness of the 1-2.5 keV halo with respect to the models is *not* the result of higher order scattering, which would increase the halo surface brightness beyond that estimated with single scattering alone (Mathis & Lee 1991). The apparent reduction in scattering efficiency is instead suggestive of micron-sized grains in the foreground of Cyg X-3. Throughout this study I apply the RG approximation, which holds for grains smaller than the photon energy such that $a_{\mu\mathrm{m}} \lesssim E_{\mathrm{keV}}$ (Smith & Dwek 1998). When grains become large enough to violate the RG approximation, the Mie scattering solution must be applied, which greatly decreases the scattering cross-section due to absorption by grain material. Unfortunately, calculating the halo intensity with Mie scattering is computationally intensive, preventing a Bayesian analysis of the low energy scattering halo at this time.

I attempted to fit the high energy component of the scattering halo with various combinations of spatial and size distributions and at least one dust population with $a_{\mathrm{max}} \sim 2\ \mu$m. I then computed Mie scattering halos for the lower energy halos. Since larger grains lead to more compact scattering halos, I was only able to improve residuals in the inner region across all energy bins. All of the fit attempts were unable to account for the reduced halo brightness in the region $r > 50$ pixels. I speculate that a population of large dust grains with $\tau_{\mathrm{sca}}(1\ \mathrm{keV}) \gtrsim 3$ may account for the reduced scattering brightness while creating a more extended halo due to multiple scattering effects. Testing this hypothesis is more computationally intensive, requiring both Mie and higher order scattering terms, and is reserved for future work.

3.4.3 Possible Sources of Systematic Error

I evaluated the data for systematic errors regarding the source flux and production of the PSF template. Energy ranges with underestimated point source photon fluxes would cause an overestimate of the residual scattering halo. The flux model described in Section 3.2, *diskpn* emission with ISM absorption and dust scattering, was used to scale the PSF. This model closely matches the shape of the continuum except in the region 3-5 keV. In this energy range, there is a discrepancy between the HEG and MEG extracted spectrum due to pileup, which occurs more easily for the MEG arm. However, the photon flux in the HEG arm is only 10% brighter than the flux calculated with my model. I also used the `pileup_map` tool in CIAO to estimate the degree of pileup in the HEG dispersed spectrum. This suggested that no more than 1% of the continuum and 5% of spectral line photons are piled. Thus the model spectrum is at most 15% too dim and does not account for the decreased brightness of the 1-2.5 keV halo relative to 2.5-6 keV.

The abrupt decrease in scattering halo flux may be partly due to instrumental effects. The Al-K and Ir-M absorption edges cause swift changes in the telescope effective area around 1.55 and 2.1 keV, respectively. Si-K and Au-M absorption (1.8 and 2 keV) can also remove or alter, through fluorescence, the observed energy of incoming photons in this range. I corrected for this by using weighted exposure maps (§3.2), which improved the 1.75 and 2.25 keV residuals (Figure 3.3) in comparison to measurements utilizing single energy exposure maps.

Finally, it is possible that the $E \gtrsim 4$ keV PSF was underestimated due to a lack of signal. The surface brightness of the PSF template edges are comparable to the background

region, suggesting that 3C 273 was not bright enough to bring out the PSF wings at 100''. The *Chandra* PSF broadens at higher energy, and thus the edges of the 4-6 keV halos may have been overestimated. However, the lack of PSF signal also contributes larger error bars at higher energies (e.g. in Figure 3.3), yielding acceptable $\Delta\chi$ residuals.

3.4.4 Energy Resolved Halo Fits

For completeness I fit the uniform and two screen models to each energy resolved halo of Section 3.4.2 using the methods described in Section 3.3.1 and 3.3.2. Figure 3.5 shows the median (*circles*) and 1σ confidence intervals (*bars*) for the posterior distribution of each parameter. In all cases the 1-2.5 keV fits differed significantly from the others. Since all fits point to $\tau_{\rm sca}$ being optically thick at 1 keV, higher order scattering effects need to be taken into account for objects with similar ISM columns to Cyg X-3. Ignoring the lowest energy bin, the 1-6 keV models are relatively consistent with the other two fits. I will move forward with the analysis using the models optimized for 1-6 keV.

3.5 Dust-to-gas mass ratio

The X-ray point source spectrum of Cyg X-3 can be used to fit the hydrogen column, assuming a near solar mix of ISM metals, which contribute significantly to the absorption of X-rays above 1 keV compared to neutral hydrogen by itself (Wilms et al. 2000). Along particularly dusty sight lines, it is also necessary to include the contribution of dust scattering to the total point source extinction. I fit the high resolution spectrum of Cyg

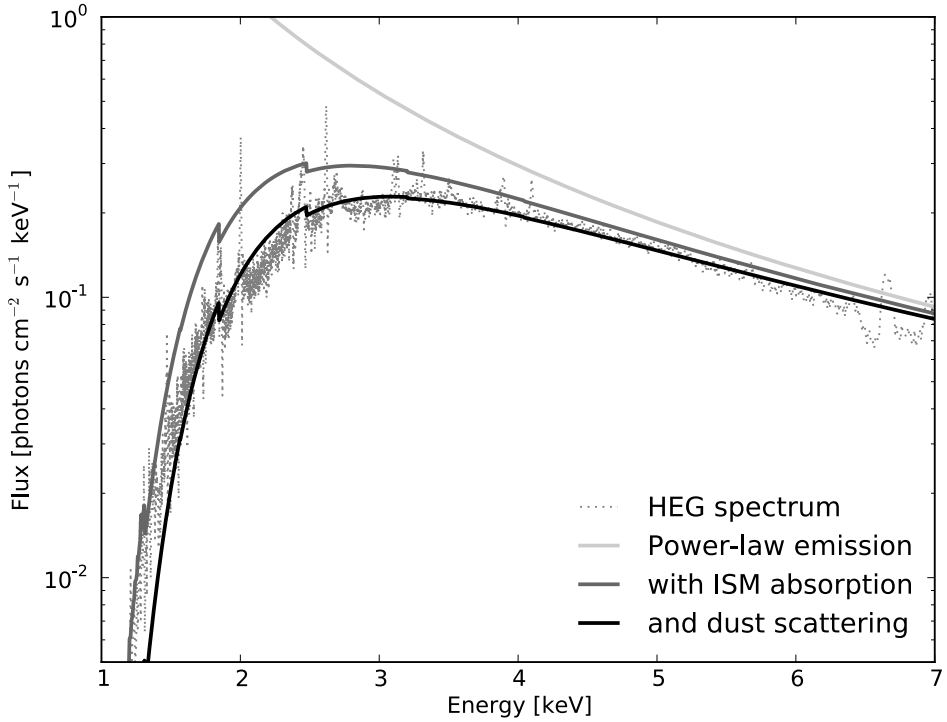

Figure 3.6 High resolution spectrum of Cygnus X-3 obtained from the grating dispersed light in *Chandra* ObsID 6601. The spectrum is modeled with an X-ray emission power law (*light grey*), modified by ISM gas absorption (*medium grey line*) and finally dust scattering (*dark grey*). The optical depth of the dust scattering component shown here is 2.2 at 1 keV.

X-3 with a three component model: (i) X-ray emission in the form of a power-law, (ii) ISM absorption using the metal abundances outlined in Wilms et al. (2000), and (iii) fixed extinction of the form $\tau_{\rm sca}\, E_{\rm keV}^{-2}$, with optical depths pulled from the posterior distributions of Sections 3.3.1 and 3.3.2.

Figure 3.6 shows an example X-ray spectral fit with $\tau_{\rm sca} = 2.2$. The model spectrum is systematically low for $E < 2$ keV, hinting again that the true scattering efficiency is reduced in comparison to RG expectations. The spectral fit requires a particularly large ISM column, $N_{\rm H} = 6{\times}10^{22}$ cm^{-2}. Since a large fraction of the X-ray absorption above 1 keV is accounted for by interstellar metals, the $N_{\rm H}$ value measured from the X-ray continuum

should more closely follow the abundance of metals (and dust) than hydrogen. This may explain why A_V is well correlated with X-ray absorption (Predehl & Schmitt 1995; Güver & Özel 2009). According to these studies, the ISM column of 6×10^{22} cm^{-2} suggests a large extinction, $A_V \sim 30$. This value is unusually high, given the average Galactic disk extinction rate of $A_V = 1.8$ mag/kpc (Whittet 1992), implying $A_V \approx 13 - 23$ for Cyg X-3.

The unique environment in the foreground of Cyg X-3 may explain the extinction implied by the rather large ISM column. The Cyg OB2 association exhibits a mean color excess of $E(B-V) \approx 1.2$ (i.e. $A_V \approx 3.7$ for typical Milky Way dust). The three cluster members closest to Cyg X-3 in angular distance, Cyg OB2 No 12, 3, and 9 (17′, 18′, and 20′ away) are significantly more extincted: $E(B-V) = 3.2$, 1.6, and 1.7 implying $A_V \approx 10$, 5, and 6 (Johnson 1965; Nicolet 1978). This accounts for an additional 3-7 magnitudes of extinction beyond average and implies that the sight line to Cyg X-3 is unique.

A final caveat, however, is that the ISM column fit is deeply sensitive to the choice of X-ray emission model. The power law does not produce a particularly good fit ($\bar{\chi}^2 = 4.0$), partly due to the strong emission lines distributed across the spectrum. The XSPEC model *diskpn*, a post-Newtonian accretion disk emission model appropriate for HMXBs such as Cyg X-3 (Gierliński et al. 1999), yields a lower ISM column ($N_{\rm H} = 4.8 \times 10^{22}$ cm^{-2}) and produces a slightly better fit ($\bar{\chi}^2 = 3.6$). Either way, absorption over the entire *Chandra* energy range is required to match the general shape of the spectrum. A multi-component model more accurately describes the X-ray emission of Cyg X-3, for which disk reflection tends to dominate the medium/high energy component around 6 keV (e.g. Szostek et al. 2008; Zdziarski et al. 2010). Since the soft model component is apparently dominated

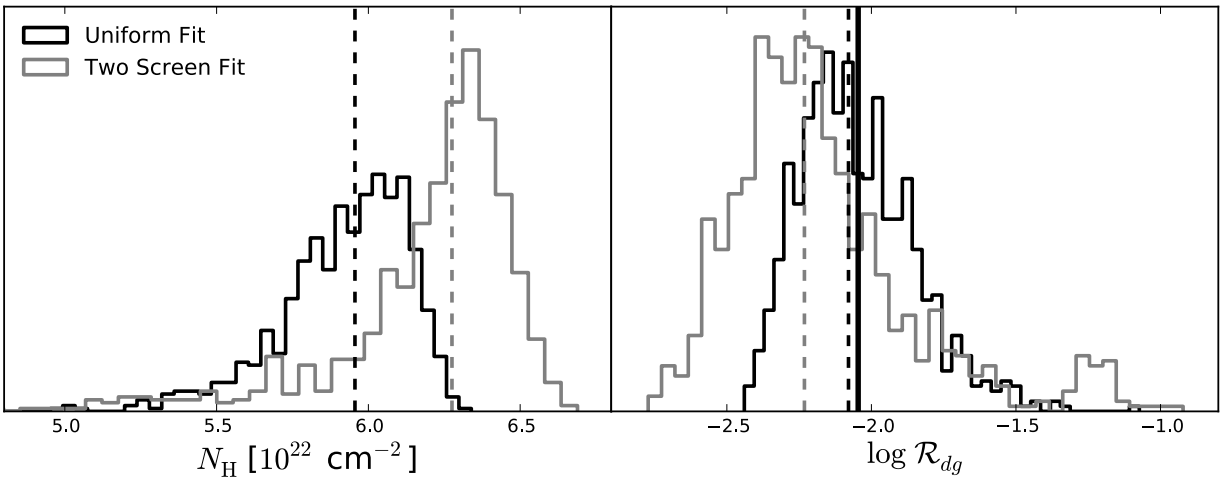

Figure 3.7 The ISM column $N_{\rm H}$ (*left*) and the inferred dust-to-gas mass ratio $\mathcal{R}_{dg}$ (*right*) are plotted by fitting the Cyg X-3 spectrum with points drawn from the posterior distribution of the uniform (*dark*) and two screen (*light*) model fits to the 1-6 keV dust scattering halo. The dashed lines mark the median of each distribution, and the solid black line marks the average Milky Way dust-to-gas mass ratio (Draine 2011).

Table 3.3. Spectral fits for dust-to-gas mass ratio

	Peak	Median	(1σ C.I.)	Units
Uniform Fit				
$N_{\rm H}$:	6.0	5.96	(5.73, 6.12)	10^{22} cm^{-2}
$\mathcal{R}_{dg}$:	0.68	0.83	(0.57, 1.4)	10^{-2}
Two Screen Fit				
$N_{\rm H}$:	6.3	6.28	(5.99, 6.43)	10^{22} cm^{-2}
$\mathcal{R}_{dg}$:	0.46	0.59	(0.36, 1.2)	10^{-2}

by absorption, there is little that can be said regarding the true nature of the soft X-ray spectrum. In the future, X-ray scattering physics could be applied to less obscured X-ray binaries within the Galaxy to yield more accurate dust-to-gas mass ratios along different ISM sight lines.

After fitting for the ISM column, I calculated the dust-to-gas mass ratio ($\mathcal{R}_{dg}$) using

the dust mass column (M_d) from the scattering halo fit.

$$\mathcal{R}_{dg} \equiv M_d / N_H m_p \tag{3.5}$$

Figure 3.7 plots the distribution of $N_{\rm H}$ and $\mathcal{R}_{dg}$ obtained from the posterior distributions of Sections 3.3.1 and 3.3.2. Table 3.3 lists the position of each histogram peak, the median, and 1σ confidence intervals drawn from Figure 3.7. The dust-to-gas mass ratio obtained from both fits is consistent with that assumed for the Milky Way ($\mathcal{R}_{dg} \approx 0.009$, Draine 2011), but tends to favor slightly lower values as determined by the peak and median values of the distribution.

3.6 Discussion

I have evaluated the Bayesian Information Criterion to find that a model implementing uniformly distributed dust along the line of sight (§3.3.1, BIC= 16.0) performs similarly to a model of two dusty screens associated with the Perseus and outer Milky Way spiral arms (§3.3.2, BIC= 18.4). The fact that a power law distribution of uniformly distributed dust can well describe the shape of the scattering halo attests to the survival of the MRN model, which has a noteworthy ability to describe Milky Way dust *on average*. This is surprising, considering the variety of interstellar environments expected along the Cyg X-3 sight line, which includes young stellar clusters and molecular material in addition to the diffuse ISM.

Bayesian analysis allowed me to incorporate and quantify prior knowledge about

the relative position of the two dusty foreground screens. While this model performs similarly to the uniform fit, I find that there is less discrepancy between the two screen fit and the 1-2.5 keV residuals for $r < 30$ pixels (§3.4.2). Thus an optically thin body of dust within 1 kpc of the Cyg X-3 best describes the inner portion of the scattering halo.

The two screen fit also yielded an $a_{\rm max}$ value more in line with the traditional grain size cut offs (0.21 μm) than the uniform fit (0.14 μm). Since X-ray scattering is incredibly sensitive to large dust grains, it probes the turn off points of more complicated grain size distributions such as WD01 and ZDA. My approach attempts to derive a grain size distribution from the data. In the future, a broken power law or exponential decay around the grain size cut-off should be implemented in order to contribute to, not just test, advanced grain size distributions.

3.6.1 Implications for optically thick sight lines

I have demonstrated in Section 3.4 that the sight line to Cyg X-3 is optically thick to dust scattering and departs significantly from the classic RG treatment of X-ray scattering. For MRN dust with $a_{\rm max} = 0.25$ μm, $\tau_{\rm sca} = 0.7$ per 10^{22} of hydrogen column. Multiple scattering effects should thereby be significant for a number of bright dust scattering halos. On the other hand, Smith et al. (2006) showed that the second order scattering halo with $N_{\rm H} = 4 \times 10^{22}$ cm^{-2} increases the intensity of the inner halo by about 5% but has little effect on the profile shape for angles < 100″. Multiple scattering should have a greater influence on f_{cap} (Equation 3.4), affecting analysis of the observed halo to point source flux ratio (§3.4.1).

This work also presents a wider range of energy resolved X-ray scattering halos than previously covered in the literature (e.g. Smith et al. 2006; Valencic et al. 2009). Fits utilizing the RG approximation and single scattering regime differ significantly when applied to 1-2.5 keV as opposed to those applied to higher energy bins, where the approximations are more appropriate. I also find that the 1-2.5 keV scattering halo intensity is significantly reduced with respect to models fit to higher energy halos. I encourage future works treating dust scattering along optically thick $N_{\rm H} \gtrsim$ few $\times 10^{22}$ sightlines to limit themselves to $E > 3$ keV scattering.

The dim 1-2.5 keV scattering halos cannot be explained by multiple scattering, which would increase the halo intensity with respect to the single scattering models. Mie scattering poses one solution. When $\gtrsim 0.5$ μm size grains make up a significant fraction of the grain size distribution, the total scattering cross-section is reduced. There is reason to believe that grains larger than a few tenths of a micron exist in the young stellar cluster Cyg OB2, which is in the foreground of Cyg X-3. Cold dense regions of molecular clouds are likely to be a location of grain growth (Draine 2003a).

Unfortunately, attempts to decrease the 1-2.5 keV scattering efficiency with $a_{\rm max} \sim 1 - 2$ μm only affects the core of the halo ($r < 50$ pixels); the outer edges of the 1-2.5 keV profile are still dimmer than expected. The inclusion of higher order Mie scattering halos might resolve this problem by boosting scattering intensity at larger angles, at considerable computational cost. I reserve this calculation for future work.

3.6.2 Comparison to other X-ray halo studies

The highly degenerate nature of X-ray scattering through dust makes the Bayesian approach to data analysis a powerful tool. The analytic solutions for the scattering halo surface brightness profile (presented in Section 1.4) allowed for fast computation and analysis that has not been applied in this field. The discussion presented here, however, is one of several differing conclusions regarding the nature of dust along the line of sight to Cygnus X-3.

Predehl & Schmitt (1995, hereafter PS95) included Cyg X-3 in a study of X-ray scattering halos visible with ROSAT. The halo around Cyg X-3, being 40% as bright as the central point source, had the largest optical depth in the study. They fit the surface brightness profile by integrating Equation 1.8 with dust uniformly distributed between some $x_{\rm min}$ and $x_{\rm max}$ values. Since the ROSAT PSF is much broader, only the outer part of the halo ($\alpha > 100''$) was visible, leading them to be more sensitive to dust close to the observer. Regardless, they got similar values for $a_{\rm max}$ (0.20 μm) and p (3.8) in comparison to the uniform fit.

My fit to the ISM column differs dramatically from PS95, because *Chandra* covers a broader energy range than ROSAT, which is sensitive to 0.3-2.4 keV X-rays. Since the power law slope is expected to match the SED slope near the high energy side, PS95 measured $N_{\rm H} = 3.3 - 4.1 \times 10^{22}$ cm^{-2}. It is apparent from Figure 3.6 that the slope you would get from examining the 2-3 keV spectrum is shallower than that from the 5-7 keV region, thus requiring a large amount of ISM absorption to account for the dramatic turn over around 3 keV.

The scattering halo of Cyg X-3 was also included in a study by Xiang et al. (2005). Using ObsID 425, they extracted the halo image from the 1-D projection of the halo data along the direction of MEG arm (see also Yao et al. 2003). This method of extraction produced surface brightness profiles that are steep in the inner 5″ (10 pixels) and less steep in the outer regions. This leads them to conclude that all of the objects in their study are embedded in molecular clouds, because all of the dust mass needs to be located very close to the X-ray point source. In the case of Cyg X-3, this required $N_H \sim 4 \times 10^{22}$ cm^{-2} within 100 pc of the HMXB. This study does not resolve the scattering halo within 10 pixels of the point source, but it is possible that the particularly indirect method used by Xiang et al. (2005) led to a systematic error in the inner regions of the halo. I measure the scattering halo directly from the zeroth order image of Cyg X-3 instead.

Cyg X-3 is an eclipsing binary with a 4.8 hour period (Brinkman et al. 1972), making it a good object for studying scattering in the time domain. Since the scattered light takes a longer path, there is a time delay between non-scattered and scattered light. Predehl et al. (2000) use the first *Chandra* observations of Cyg X-3 to determine a geometric distance of 9^{+4}_{-2} kpc without requiring many assumptions regarding the dust distribution. Ling et al. (2009a) perform a more in depth cross-correlation timing analysis of Cyg X-3. They find that dust associated with Cyg OB2 could explain time lags in the $\alpha > 65''$ halo, but that only accounts for 7% of the total dust along the line of sight. The remainder of the data is well fit with uniformly distributed dust. I did not perform a uniform plus screen fit because the screen contribution would be similarly negligible.

Depending on the Cyg OB2 distance, Ling et al. (2009a) measure 3.4, 7.2, and 9.3 kpc

to Cyg X-3. I put rather strict priors on the screen positions to correspond to the Perseus and outer spiral arms of the Milky Way, because the scattering halo from the nearby Cyg OB2 cluster would not be bright enough to substantially affect the fits. Note however that the most distant ($x \approx 0.1$) screen can be substituted with Cyg OB2 ($x \approx 0.8$) if the associated dust population has a large $a_{\rm max}$, which would lead to a brighter and more compact scattering halo. Nonetheless, for the sake of thought experiment, associating Screen 1 with the Cyg OB2 cluster at 1.7 kpc requires Cyg X-3 to be 3.1 kpc away. This is consistent with one measurement by Ling et al. (2009a), but the source of the Screen 2 dust would be a mystery. If Screen 1 is associated with the Perseus arm 5.4 kpc away, as I postulated, then the posterior distribution from Section 3.3.2 implies that Cyg X-3 is 9.6 ± 1.0 kpc away, consistent with Predehl et al. (2000).

ObsId 6601 covers three cycles of the Cyg X-3 eclipse. I used all of the light under the assumption that the average brightness of the point source describes the average brightness of the scattering halo. However, there is temporal variation in the scattering halo surface brightness for $r < 30$ pixels ($\alpha \lesssim 15''$). Since the error bars in this region are also significantly larger, the fits are more sensitive to the portion of the scattering halo that does not fluctuate dramatically in brightness.

3.7 Conclusion

The Bayesian approach is powerful because it allows us to adjust for degenerate solutions and to inject prior knowledge about the model (for example, the approximate positions of dust screens). I take this approach to analyze one of the brightest dust scattering halos

available in the *Chandra* archive, that associated with Cyg X-3. I find that a uniform distribution of dust along the line of sight fits the scattering halo profile for the region $\alpha < 100''$ (200 pixels). This suggests an MRN type grain size distribution with a smaller grain size cut off than typically assumed, around 0.14 μm. As an alternative, the scattering halo can also be fit with two infinitesimally thin dust screens placed in the foreground of Cyg X-3. About 80% of the dust would be close to the observer, most likely associated with the Perseus spiral arm of the Milky Way. The remaining 20% of the dust would have to be within 1 kpc of Cyg X-3, contributing most to the inner portion ($r < 30$ pixels) of the scattering halo. The grain size distribution suggested by the two-screen fit has a similar cut off to MRN (0.2 μm). The results are consistent with other published conclusions regarding the distance to Cyg X-3 and the dust grain distribution along its sight line.

I fit the continuum of the Cyg X-3 spectrum for ISM column ($N_{\rm H} \approx 6 \times 10^{22}$ cm^{-2}) and compare it with the dust mass measurement from the scattering halo to yield a dust-to-gas mass ratio. The results are consistent with the average Milky Way dust-to-gas mass ratio 0.009, but fits drawn from the posterior distribution of the Bayesian analysis favor slightly smaller values $0.005 - 0.007$.

The nature of the 1-2.5 keV scattering halo, which is dimmer than expected, might be explained by reduced scattering efficiency of $E < 2.5$ keV X-rays by micron sized grains. The abnormally large extinction of Cyg OB2 cluster members (No. 12, 3, and 9) in the angular vicinity of Cyg X-3 emphasizes the unique nature of this particular sight line, which might host dust grains of larger size or different composition than those in the diffuse ISM. However I were unable to resolve this issue in the single scattering regime.

A full Bayesian analysis with higher order Mie scattering is too computationally intensive to undertake for now and should be implemented in the future.

Fits to the energy resolved X-ray scattering halos yield dramatically different results for $E < 2.5$ keV in comparison to $E > 2.5$ keV. In the future, sight lines with $N_{\rm H} \gtrsim 3 \times 10^{22}$ cm^{22} cm^{-2} should restrict analysis to higher energy scattering halos > 3 keV. Otherwise, higher order scattering halos (e.g. Mathis & Lee 1991) need to be considered.

Chapter 4

Cosmological X-ray Scattering from Intergalactic Dust[1]

The existence of a population of intergalactic dust grains would have wide-reaching implications for our understanding of the universe. A population of grey intergalactic dust would affect extragalactic surveys that require precise optical and infrared photometry. X-ray astronomy provides a unique opportunity to detect and characterize dust that may be missed by traditional detection methods, which consider background object colors (e.g. Wright 1981; Ménard et al. 2010b). By looking at extragalactic X-ray point sources (quasars) well above the Galactic plane, observers can characterize the quantity of dust in the intergalactic medium (IGM) (Evans et al. 1985). I will derive the formulae for scattering in a cosmological context and discuss interesting topics for which X-ray scattering can yield insight into the high-z universe.

[1]This chapter is a reformatted version of an article by the same name by L. Corrales & Paerels that can be found in The Astrophysical Journal, Volume 751, Issue 2, pp. 93-104.

Stars create elements heavier than helium and thereby are the main contributors of dust building-blocks. The mass of intergalactic dust thus depends on the cosmic history of star formation and dust dispersal mechanisms. Aguirre (1999) estimated that about 50% of metals at $z \sim 0.5$ are present in the IGM, and if $\sim 50\%$ of those metals are locked up in dust, then $\Omega_{\rm dust}^{\rm IGM} \sim 10^{-5}$. More recent determination of cosmological parameters would only change these estimates $\sim 25\%$. Constraints on the amount of cosmic dust using the thermal history of the IGM agreed that $\Omega_{\rm dust}^{\rm IGM}(z = 3) \lesssim 10^{-5}$ for grain sizes $a \geq 0.01$ μm (Inoue & Kamaya 2003). Dijkstra & Loeb (2009) put an upper limit on $\Omega_{\rm dust}^{\rm IGM}$ from 7×10^{-5} to 1.5×10^{-4}, under the hypothesis that 10% of the soft X-ray background is the result of dust scattered light from AGN. From this assumption they also showed that the optical depth to X-rays must be $\lesssim 0.15$ at $z = 1.5$. A previous search for a cosmological scattering halo around QSO 1508+5714 at $z = 4.3$ by Petric et al. (2006) yielded a null result. They used this to place the constraint $\Omega_{\rm dust}^{\rm IGM} < 2 \times 10^{-6}$. I will show that our models are consistent with their observation and that the limits placed on the amount of intergalactic dust can be relaxed (§4.5).

In Section 4.1 I will examine the potential enrichment sources and the relative amounts of dust one might expect to find in the IGM. The first stars in the early universe (Pop III) and feedback from early star forming galaxies could have enriched the IGM with metals, creating a fairly uniform dust distribution that is comoving with cosmological expansion. I will use the X-ray scattering cross-section from Section 1.2 to derive the scattering halo intensity from a constant comoving density of dust grains (Section 4.2). Quasar absorption systems, caused by dense regions of neutral hydrogen – often with traces of ionized metals

– already contain signatures of dust extinction (Ménard et al. 2005; York et al. 2006). Of individual dust sources, Damped Lyman-α systems (DLAs) are the densest absorbers and thus have the highest probability of producing an X-ray scattering signature. I will evaluate this possibility in Section 4.3 by calculating the X-ray scattering profile from an infinitely large screen of dust with column densities typical of DLAs.

Due to the large distances associated with cosmological scattering and the nature of small angle scattering, the angular extent of an X-ray scattered halo can put limits on the uniformity of the IGM or the size of a dusty cloud. The halo image is sensitive to dust at redshifts $z \lesssim 2$ and is relatively insensitive to the redshift of the background point source. I will discuss the distances and timescales associated with cosmological X-ray scattering in Section 4.4. Observing a scattering halo, in addition to finding extragalactic reservoirs of dust, can provide information about the nature of star formation and galactic structure at high-z. In Section 4.5 I will reevaluate QSO 1508+4714, used by Petric et al. (2006), in the 1-8 keV band to show that large dust grains with $\Omega_{\rm dust}^{\rm IGM} = 10^{-5}$ cannot be ruled out. The implication of this result are summarized in Section 4.6.

4.1 Potential Sources of Intergalactic Dust

Intergalactic dust may be distributed uniformly as a result of star formation in the early universe. If that is the case, an azimuthally symmetric X-ray scattering halo may be observed around a background point-source at a distance large enough to provide sufficient column density for scattering. Dust may also be efficiently distributed into galactic halos or the IGM through pressure-driven feedback from galaxies. This effect may be partic-

ularly important at $z \sim 2-3$, during the epoch of star formation, and for small galactic halos from which outflows can more easily escape. Previous work has concluded that dust grains > 0.1 μm are more efficiently expelled than smaller grains because they are grey to optical light, hence receiving more radiation pressure, and are less susceptible to deceleration by gas drag (Davies et al. 1998a; Ferrara et al. 1991a). Finally, if very little dust ($\Omega_{\rm dust}^{\rm IGM} \lesssim 10^{-6}$) is evenly distributed throughout the cosmos today, one could potentially observe X-ray scattering from objects that are already known to have high column densities of gas and metals. Quasar absorption systems offer a convenient opportunity to observe X-ray scattering from dust that may be present in these gas reservoirs.

4.1.1 The Earliest Star Formation

Population III stars formed from the near-pristine primordial hydrogen gas originating from the Big Bang, are typically $\sim 40-100 M_{\odot}$, and form in dark matter halos $\sim 10^6 M_{\odot}$ between $z \sim 20-30$ (Bromm & Larson 2004; Hosokawa et al. 2011). These stars are very large because cooling below 10^3 K can only proceed by collisional excitation of the rotational modes of H_2 molecules. Fragmentation into smaller clumps is possible once gas becomes enriched to a particular threshold, above which the cooling rate from metals dominates over H_2 cooling and exceeds the heating rate due to gravitational collapse: [C/H] ≈ -3.5 and [O/H] ≈ -3.1 (Bromm & Larson 2004). Many consider this critical metallicity to mark the transition between the era of Pop III and Pop II stars, which have low metallicity but are able to form smaller ($\sim 1\ M_{\odot}$) stars that are observed today in globular clusters, dwarf spheroidal galaxies, and galactic halos. The large characteristic mass-scale of Pop III stars

indicates that the majority of stars ended their lives as supernovae, distributing metals. If some of these metals are locked up in dust, it would contribute to cooling and allow gas to fragment at metallicities well below the critical threshold for metal line cooling (Schneider et al. 2006). The recent observation of a low-mass, extremely metal poor star with [Z/H] ~ -5 (Caffau et al. 2011) supports the hypothesis that the first generation of stars produced dust.

Because Pop III stars are massive and form in small halos, feedback from radiation and thermal injection from supernovae are significant. Thus the first generation of stars can efficiently remove gas from mini-halos and mix metals into the IGM (Heger & Woosley 2002; Bromm et al. 2003; Abel et al. 2007; Wise & Abel 2008). In simulations by Wise & Abel (2008), the second generation of Pop III stars had metallicities $-5 <$ [Z/H] < -3 and formed around $z = 20$; the third generation reached metallicities [Z/H] $\gtrsim -3$. These serve as an upper limit, because the simulations assumed that every Pop III star ended in a pair-instability supernova (PISN). At solar metallicity, the mass ratio of metals versus H and He is ≈ 0.02 (Draine 2011). Using this value to scale the metal mass by metallicity, the total dust-to-gas mass ratio of the Pop III enriched IGM is

$$\left(\frac{M_d}{M_{\rm H}}\right)_{\rm III} = 0.02\ f_{\rm dep}\ \left(\frac{Z}{Z_\odot}\right) \tag{4.1}$$

where $f_{\rm dep}$ is the mass fraction of metals locked in dust. Dust models suggest that $f_{\rm dep}$ can be rather high for both PISNe (0.3-0.7) and Type-II SNe (0.2-1) (Schneider et al. 2004; Todini & Ferrara 2001). Taking the metallicity threshold above which hydrogen clouds fragment, I can make a reasonable guess that the first stars may have enriched the IGM to

a uniform background level of [Z/H]~ -4. Equation 4.1 then implies $(M_d/M_{\rm H})_{\rm III} \leq 2\times10^{-6}$.

Compare this to the ratio implied by assuming a particular value for the dust mass density in the IGM:

$$\left(\frac{M_d}{M_{\rm H}}\right)_{\rm IGM} \approx 7 \times 10^{-6}\ \Omega_{\rm dust}^{\rm IGM}\ \bar{n}_{\rm H}^{-1}\ h_{75}^2 \tag{4.2}$$

where h_{75} is H_0 in units of 75 km/s/Mpc, and $\bar{n}_{\rm H} \sim 10^{-7}$ cm^{-3} is the average baryon density of the universe today. If $\Omega_{\rm dust}^{\rm IGM} \sim 10^{-5}$, the first generation of stars would have contributed ~1/350 of that dust. If Pop III stars were responsible for the entirety of IGM dust, they would have to pollute the universe to [Z/H]~ -1.5, and all of those metals must be locked up in dust. This is not likely to occur before the onset of smaller stellar populations and galaxy evolution. Feedback from the second generation of stars and early galaxies is therefore required to bring the overall dust density of the IGM to a threshold detectable via X-ray scattering.

4.1.2 Feedback from Galaxies at High and Low-z

There is direct evidence that L* galaxies today can expel dust out to a few kpc at least. Polarized light, a consequence of scattering, was observed around the disk of the starburst galaxy M82 well before its dusty outflows were imaged by *Hubble* and *Spitzer* (Schmidt et al. 1976). The outflows are fueled by starburst activity and can host super-solar abundances, a result of supernovae enrichment, effectively contaminating the IGM with metals (Konami et al. 2011).

In theory, dust grains can be efficiently expelled from a galactic disk when the forces of radiation pressure, gravity, and gas drag are weighed. Large grains (≥ 0.1 μm) can be

expelled completely from optically thin disks, while small grains are either retained close to their formation sites or trapped in layers within the galactic halo (Davies et al. 1998a; Greenberg et al. 1987a). The expulsion is also more efficient for graphite grains ~ 0.1 μm, which absorb more light across the visual spectrum than silicate grains of comparable size, and can reach velocities of several hundred km/s. The smaller timescale for exiting the halo allows graphite grains > 0.1 μm to survive sputtering processes compared to silicate grains, which exit slowly and are thus more likely to be destroyed (Barsella et al. 1989; Ferrara et al. 1991a). On the other hand, graphite grains can accumulate more charge than silicate grains as they exit a galactic disk. Coulomb forces prevent graphite grains from traveling as far as silicate grains with the same starting velocity, an effect that may allow silicate grains to populate a galactic halo or the IGM (Bianchi & Ferrara 2005). Regardless, enrichment processes suggest that an IGM dust population is likely to contain grains $\gtrsim 0.1$ μm in size and is consequently grey to optical light.

Dust grain expulsion is not just a side-effect, but may be *necessary* for galactic outflows to occur. Murray et al. (2005) argued that the Faber-Jackson relation between an elliptical galaxy's luminosity and velocity dispersion can be explained by the balance between momentum driven winds and stellar luminosity. They also showed that, for radiation pressure to act efficiently, dust is required to contribute to the total ISM opacity. As material is expelled, the gas may become sufficiently diffuse for the dust to decouple and migrate outwards alone. They estimated the radius at which this occurs (R_{dg}), with respect to the velocity dispersion (σ), gas fraction (f_g), and dust grain size (a):

$$R_{dg} \sim 150\, a_{(0.1\ \mu\mathrm{m})}\, \sigma^2_{(200\ \mathrm{km/s})}\, f_{g,0.1}\ \mathrm{kpc} \tag{4.3}$$

where 0.1 μm, 200 km/s, and 0.1 are fiducial values for a, σ, and f_g respectively. Dust grains $\sim$ 0.1 μm expelled from very small halo potentials ($\sigma \sim 50$ km/s) would decouple from the gas 10 kpc beyond the site of origin. Thus during the epoch of star formation, gas may not reliably trace the spatial distribution of intergalactic dust. If that is the case, the fraction of IGM metals locked up in dust may be rather large (~ 0.5).

An estimate for the total metallicity of the universe as a function of redshift can be obtained by integrating over the observed star formations rates, yielding $\Omega_Z = 2.5 \times 10^{-5}$ at $z = 2.5$ (Pettini 2006). The total mass of metals observed in Ly-α absorption systems and Lyman Break Galaxies (LBGs) at $z = 2.5$ differs by the amount predicted by a factor of few, coined the "missing metals problem" (Pagel 2002; Pettini 2004). The discrepancy may be due to uncertainty in the star formation rates between $z = 4 - 10$ or galaxies that have been missed by UV-selection (Pettini 2006). Bouché et al. (2007) used analytic calculations to conclude that around 50% of the total expected metal mass at $z = 2$ could have been ejected by sub-L* (the majority of which comes from L < 1/3 L*) galaxies. If 50% of intergalactic metals are locked up in dust, then $\Omega_{\rm dust}^{\rm IGM}(z \leq 2) \sim 8 \times 10^{-6}$ due to pollution by sub-L* galaxies during the epoch of star formation. X-ray scattering halos can help test whether or not metals really have been missing from observations of the $z = 2$ universe, and whether feedback mechanisms can account for the supposed deficiency.

4.1.3 Damped Lyman-α Absorbers

DLAs are dense regions of neutral hydrogen ($N_{\rm HI} \geq 2 \times 10^{20}$ cm^{-2}) observed via broad Lyman-α absorption features in quasar spectra. They account for the majority of neutral

hydrogen out to $z = 5$, making them likely candidates as the gas reservoirs for star formation. Mg II and other singly ionized metals are also found at redshifts coincident with DLAs – enrichment that supports the link to star formation. Past surveys have used Zn and other volatile elements (Si, S, and O), showing that the majority of DLAs have sub-solar metallicities. The median metallicity is $[Z/Z_{\odot}] \sim -1.2$ (Pettini 2006), which increases with decreasing redshift from [Z/H] = −2.5 to −0.5 (Wolfe et al. 2005). DLAs are also likely to contain dust, as the amount of Fe – a refractory element that condenses at low temperature – is observed to be depleted relative to Zn and Si with increasing metal abundance (Wolfe et al. 2005). The extinction profiles for Mg II and other metal absorbing systems also show significant evidence for reddening by dust (Ménard et al. 2005; York et al. 2006).

The link between DLAs and dust is strong, but the exact nature of these systems is unknown. If they are galaxies, observing their emission is difficult because they lie along the line of sight to quasars. Their sub-solar metallicities also make it difficult to reconcile the idea that DLAs are the progenitors to the galaxies we see today. They may be dwarf galaxies, inflow, or outflow gas associated with high-z bulges or star forming regions (Wolfe et al. 2005). X-ray scattering can test these hypotheses because (i) it requires a bright X-ray point source, which the background quasar can provide; (ii) the redshift to the dusty body is known, removing some of the degeneracy in interpreting the scattered image; and (iii) the dust distribution and size of the dusty region places limits on the observed angular size of the scattering halo (§4.3).

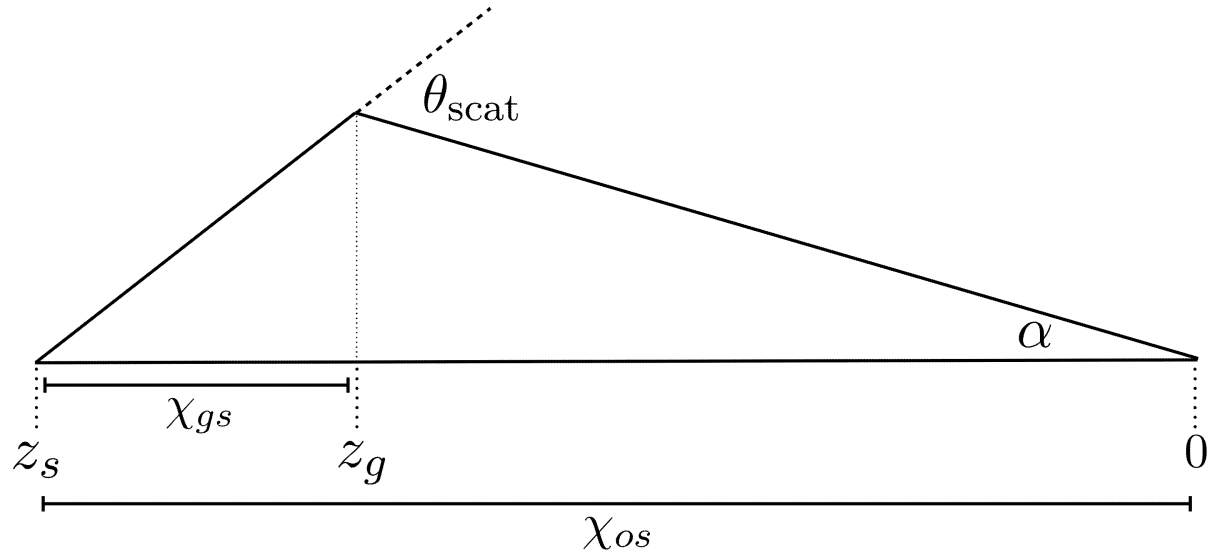

Figure 4.1 A diagram illustrating the scattering geometry in comoving coordinates. Photons that scatter through angle $\theta_{\rm scat}$ from a patch of dust grains at redshift z_g will be observed an angular distance α away from the center of the point source.

4.2 X-ray Scattering Through a Uniform IGM

Here I derive the integral for scattered light similar to Evans et al. (1985), but for an updated ΛCDM cosmology. The path taken by light scattered at cosmological distances can be traced over three events:

1. Light of frequency $\nu_{\rm em}$ is emitted from a point source at redshift z_s and reaches a patch of dust grains at redshift z_g.

2. A portion of the incident light is scattered by the dust grain patch.

3. Scattered light projected onto $\theta_{\rm scat}$ will reach the observer at $z = 0$ and be observed an angular distance α away from the center of the X-ray point source.

I use the notation $a_c = (1 + z)^{-1}$ to represent the cosmological scale factor throughout. Everywhere else, a denotes grain radius.

Figure 4.1 illustrates the geometry of the system using χ to represent the *comoving coordinate distance*:

$$\chi_{12} = \int_{z_1}^{z_2} \frac{cdz}{H(z)}. \tag{4.4}$$

I assume a flat ΛCDM universe such that $H(z) = H_0 \sqrt{\Omega_m(1+z)^3 + \Omega_\Lambda}$, where $H_0 = 75$ km/s/Mpc, $\Omega_m = 0.3$, and $\Omega_\Lambda = 0.7$.

In general, the specific flux from a source at cosmological distances is

$$F_\nu = \frac{L_\nu(\nu_{\rm em})}{4\pi R^2}\, a_c \tag{4.5}$$

where R is the *proper radial distance* between the observer and the source. In the reference frame of a dust grain at z_g, the radial distance to the light source is $R_{gs} = \chi_{gs}/(1+z_g)$. The scale factor of the universe, according to the dust grain, is $a_{c,g} = (1+z_g)/(1+z_s)$. The flux at the site of the dust grain is therefore

$$F^{\rm src}_{\nu,g} = \frac{L^{\rm src}_\nu(\nu_{\rm em})}{4\pi\chi^2_{gs}} \frac{(1+z_g)^3}{(1+z_s)}. \tag{4.6}$$

I use the subscript notation ν, g to represents the frequency of light at the dust grain site $[\nu_g = \nu_{em}(1+z_g)/(1+z_s)]$ and $\nu, 0$ for the frequency of light at the site of the observer $[\nu_0 = \nu_{em}/(1+z_s)]$.

When light interacts with the patch of dust grains, a small amount will be scattered, with intensity

$$dI^{\rm scat}_{\nu,g} = F^{\rm src}_{\nu,g}\, n(z_g)\, \frac{d\sigma_{\nu,g}}{d\Omega}\, dR \tag{4.7}$$

where $n(z_g)$ is the number density of dust grains at the scattering site and dR is the small length

$$dR = \frac{c\,dz}{H(z)(1+z_g)}. \tag{4.8}$$

Only light scattered onto the angle $\theta_{\rm scat} = \alpha/x$ will be received by an observer at $z = 0$, using the parameterization $x = \chi_{gs}/\chi_{os}$. Light from the scattering event will reach an observer at $z = 0$ with intensity

$$dI_{\nu,0} = \frac{dI_{\nu,g}}{(1+z_g)^3} \tag{4.9}$$

Combining Equations 4.6 through 4.9 gives the observed intensity of scattered light from the patch of dust grains at z_g:

$$dI^{\rm scat}_{\nu,0}(z_g,\alpha) = F^{\rm src}_{\nu,g}\,\frac{n(z_g)}{(1+z_g)^4}\,\frac{c\,dz}{H(z)}\,\frac{d\sigma_{\nu,g}}{d\Omega}\left(\frac{\alpha}{x}\right) \tag{4.10}$$

I can also substitute $n(z) = n_c(z)\,(1+z)^3$, where $n_c(z)$ represents the *comoving number density* as a function of redshift. Drop the subscript for integration over all z and substitute the flux of the source as observed at $z = 0$:

$$F^{\rm src}_{\nu,0} = \frac{L^{\rm src}_{\nu}(\nu_{\rm em})}{4\pi\chi^2_{os}(1+z_s)} \tag{4.11}$$

to get the total intensity of scattered light as a function of angular distance from the center of a point source.

$$I^{\rm scat}_{\nu,0}(\alpha) = F^{\rm src}_{\nu,0}\int_0^{z_s} n_c(z)\,\frac{(1+z)^2}{x^2}\,\frac{d\sigma_{\nu,z}}{d\Omega}\left(\frac{\alpha}{x}\right)\,\frac{c\,dz}{H(z)} \tag{4.12}$$

The differential cross-section must be evaluated at the frequency encountered by the dust grains [$\nu_z = \nu_0(1+z)$].

Equation 4.12 is missing the effects of attenuation along the path traveled by scattered light. For a sufficiently homogeneous IGM, the optical depth to extinction along the path of scattered light ($\tau_{gs} + \tau_{og}$) will be nearly identical to that encountered by light traveling in a straight line between the source and observer (τ_{os}). The extra distance traveled by scattered light, $\Delta\chi \sim 10$ kpc (§4.4.2), is not large enough to accumulate an appreciable column density for extinction.[2] Under this assumption, a factor of $e^{-\tau_{os}}$ should modify Equation 4.12. Then the source flux term can be replaced with the *apparent* flux $F^{\rm obs}_{\nu,0} = F^{\rm src}_{\nu,0}\, e^{-\tau_{os}}$. Thus throughout the paper I express the halo intensity as a fraction of the central point source apparent brightness.

I use the notation

$$\frac{d\Psi_\nu(\alpha)}{d\Omega} = \frac{I^{\rm scat}_{\nu,0}(\alpha)}{F^{\rm obs}_{\nu,0}} \tag{4.13}$$

to describe the normalized surface brightness as a function of angle. The total optical depth to scattering is

$$\tau_{\rm x} = \int_0^{z_s} \sigma_{\nu,z}\, n_c(z)\, (1+z)^2 \frac{c\, dz}{H(z)} \tag{4.14}$$

for a point-source at $z = z_s$. Approximately $\tau_{\rm x}^2$ of the source photons will scatter twice, but for the cases considered below, the optical depth to X-ray scattering is always $\tau_{\rm x} \lesssim 0.1$. Therefore I do not need to consider light that might be twice-scattered into or out of the observer's sight.

[2] A notable exception occurs if a galaxy happens to lie along the line of sight.

4.2.1 Dust Grain Distribution

I use $\Omega_{\rm dust} = 10^{-5}$ as the fiducial value of comoving IGM dust mass. The number density of dust grains for identically sized spherical particles is then

$$n_0 = 8.7 \times 10^{-24}\, h_{75}^2\, a_{\mu\rm m}^{-3}\, \rho_3\, (\Omega_{\rm dust}^{\rm IGM}/10^{-5})\ {\rm cm}^{-3} \tag{4.15}$$

where h is H_0 in units of 75 km/s/Mpc. The dust one might expect to find in the IGM would have been expelled as a consequence of galactic feedback on the ISM. I follow the interstellar dust models of Mathis et al. (1977, hereafter MRN) and Weingartner & Draine (2001, hereafter WD01) to choose a power law distribution of grain sizes.

The largest grains may be expelled from galaxies more efficiently because they contribute to the opacity of surrounding gas, receive more radiation pressure, and can withstand gas drag and sputtering processes that slow down or destroy small grains (§4.1.2). For the lower end of the size distribution, I choose 0.1 μm; dust grains smaller than this will be destroyed by $T \sim 10^5 - 10^6$ K halo gas (Ferrara et al. 1991a; Aguirre 1999). I choose an upper limit of 1 μm to balance the easy expulsion of large dust grains with the existence, but severe drop in number, of grains $\gtrsim 1$ μm. A power law with $p = 4$ matches the $R_V = 5.5$ WD01 graphite distribution in the region $0.1 \leq a \leq 1.0$ μm. To explore the possibility that the dust population resulting from outflow has a larger proportion of ~ 1 μm size grains, I also try a $p = 3$ power law throughout the paper. In the limiting case that all intergalactic dust is large, I compare the results to a dust population solely comprised of 1 μm sized grains.

Table 4.1. Optical depth to X-ray scattering for 1 keV photons

Dust Model		$d\tau_x/dR$	τ_x [%]			
Power	*Sizes* (μm)	[% Gpc^{-1}]	**z = 1**	**2**	**3**	**4**
–	1.0	1.68	5.2	8.1	9.9	11.2
($p = 3$)	0.1 - 1.0	0.92	2.8	4.5	5.5	6.2
($p = 4$)	0.1 - 1.0	0.66	2.0	3.2	3.9	4.4

The RG scattering cross-section as used in this study does not incorporate subtleties associated with different grain materials (silicate or graphite). The complex index of refraction m is calculated from the number density of electrons, which for convenience I assume is uniform regardless of grain material. Only the size range and power-law slope of the grain distribution affect the X-ray scattering intensities presented throughout this work.

4.2.2 The Surface Brightness of Scattered X-ray Light

As an X-ray photon travels between the distant quasar and the observer, its energy will shift towards the softer end of the spectrum. Thus the total RG scattering cross-section is $\sigma_{RG} \propto a^4\, E_0^{-2}\, (1+z)^{-2}$, where E_0 is the energy of the light observed at $z = 0$. The total optical depth of the universe to X-ray scattering by a uniform, comoving dusty IGM becomes

$$\tau_x(E_0) = \int_0^{z_s} \frac{c\, dz}{H(z)} \int_{a_{min}}^{a_{max}} \sigma_{RG}(a, E_0)\, \frac{dn_c}{da}\, da \tag{4.16}$$

where a is the grain radius. Table 4.1 shows the optical depth for each dust grain model and $E_0 = 1$ keV. All of them are significantly below the $\tau_x(z = 1) \lesssim 0.15$ limit set by Dijkstra

& Loeb (2009). For $p \leq 5$, the optical depth is dominated by the largest grains in the distribution, and the values in Table 4.1 scale roughly as

$$\tau_{\rm x}(E_0) \propto \Omega_{\rm dust}^{\rm IGM}\, a_{\rm max}^{5-p}\, E_0^{-2}.$$

Next, I calculate the scattering halo intensity from a power law distribution of dust grain sizes. The energy dependence of the RG differential cross-section cancels everywhere in Equation 1.4 except the Gaussian term. To account for the cosmological redshift of photon energy incident on a dust grain, I define the effective scattering angle:

$$\theta_{\rm eff} = \alpha(1+z)/x \tag{4.17}$$

where the $(1+z)$ terms comes from the Gaussian width $\tilde{\sigma} \propto E^{-1}$. The scattering halo intensity as a function of observation angle (Equation 4.12) becomes

$$\frac{d\Psi_\nu(\alpha)}{d\Omega} = \int_0^{z_s} \frac{c\,dz}{H(z)} \frac{(1+z)^2}{x^2} \int_{a_{\rm min}}^{a_{\rm max}} \frac{dn_c}{da} \frac{d\sigma_{\nu,0}}{d\Omega}(\theta_{\rm eff})\; da. \tag{4.18}$$

For very small optical depths, Equation 4.18 should equal $\tau_{\rm x}$ when integrated over solid angle.

Figure 4.2 shows the integrated halo profiles for 1 keV X-rays at $z = 1$ and 4. The total integrated fraction is shown next to each curve for the $p = 3$ dust grain model, and in each case agrees with the total optical depth to within a fraction of a percent. The increased halo intensity that results from using the $p = 3$ grain size distribution is not dramatic,

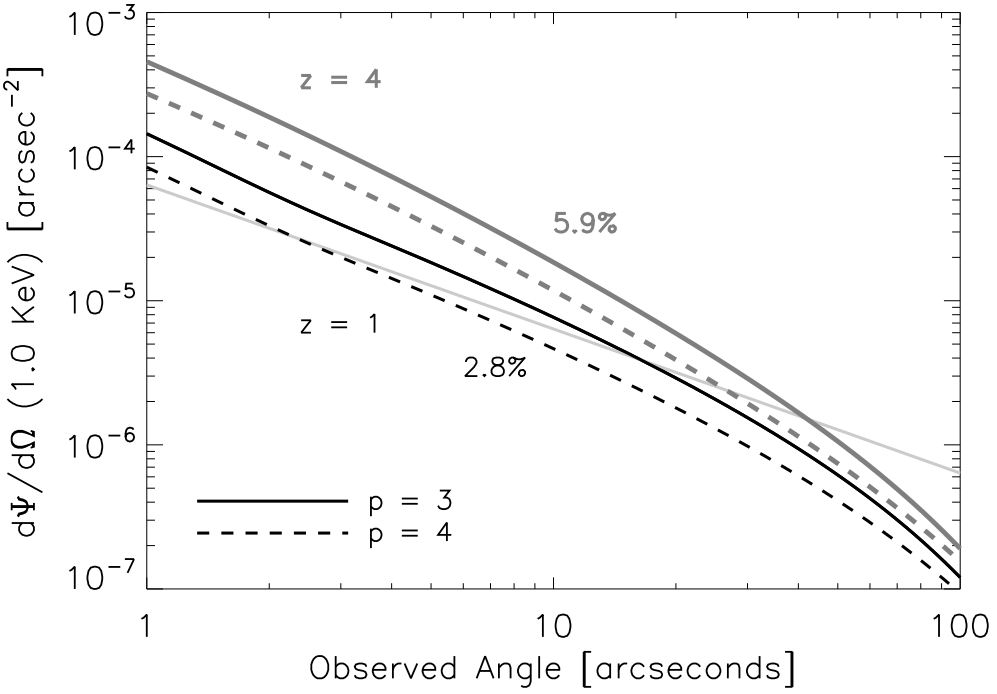

Figure 4.2 The normalized surface brightness of scattered X-ray light from a point source at $z = 1$ (black) and $z = 4$ (grey) using two dust grain distributions: $dn/da \propto a^{-3}$ (solid line) and $dn/da \propto a^{-4}$ (dashed line). The total integrated fractions for the $p = 3$ model are shown next to their respective curves. The light grey line illustrates the 100 ks *Chandra* flux limit, normalized by $F_{\rm src}^{\rm obs} = 10^{-11}$ erg/s/cm^2 and divided by solid angle.

around 50% brighter than the $p = 4$ case. This demonstrates that the halo brightness is more sensitive to the maximum grain size than the power-law exponent. The light grey line in Figure 4.2 corresponds to the radial profile that would arise if the brightness within 1″ spaced annuli summed to the 100 ks *Chandra* flux limit (4×10^{-15} erg/s/cm^2), normalized by a point source flux 10^{-11} erg/s/cm^2. This illustrates a rough threshold at which it becomes difficult to distinguish signal from background.

The scattering halo becomes more compact with larger source redshift, because the characteristic scattering angle decreases with increasing photon energy (Equation 1.5). For a fixed observed energy band, photons from a high-z source scattered at a higher energy than photons from a low-z source. Table 4.2 shows the half-light radius (containing 50%

Table 4.2. Half-light radius for 1.0 keV scattering halo around a source at varying redshift.

Dust Model	Half-light Radius (″)			
	z = 1	**2**	**3**	**4**
1 μm	22	18	16	15
$p = 3$	31	25	22	20
$p = 4$	35	29	26	24

of the total scattered light) for 1 keV X-rays. Across all grain-size models, scattering halos become more compact by 30% between redshift 1 and 4. This creates a dilemma for instruments lacking angular resolution ~ arcseconds. Point sources at high redshift may have considerably larger column density of dust, but the ability to resolve the resulting scattered halo image will become more difficult.

4.3 X-ray Scattering Through an IGM Clump

Though the universe is homogenous on a very large scale, observation along a single sightline is subject to fluctuations in baryon density, as evidenced by the Lyman-α forest and other absorption systems ubiquitous to quasar spectra. I investigate the possibility that an overdensity in the IGM can be observed individually via X-ray scattering through a screen at intermediate redshift. As before, Equation 4.6 describes the point source flux from z_s onto a screen of scattering particles at z_g. Equations 4.7 and 4.9, implemented with RG scattering (Equations 1.4 and 4.17), produce

$$\frac{d\Psi_\nu(\alpha)}{d\Omega} = \frac{N_d}{x^2}\,\frac{d\sigma_{\nu,0}}{d\Omega}\,(\theta_{\rm eff}) \tag{4.19}$$

I use the general properties of DLAs as a fiducial example because they are the densest baryon reservoirs observed along the line of sight to known X-ray point sources and are thus the most likely candidates to produce an individual scattering halo. In addition, I gauge which will contribute more to the brightness and shape of an X-ray scattering halo – the diffuse IGM or a dense cloud.

The extinction curves measured so far in quasar absorption systems best match the extinction by SMC-like dust. That is, there is no prominent 2175 Å feature, but smooth reddening when comparing the spectra of quasars with Mg II absorbers to those without (York et al. 2006; Ménard et al. 2005, 2008). Extinction curves for the SMC can be well-approximated by an MRN distribution composed purely of silicate grains – absent are the smallest graphitic grains (PAHs) responsible for the 2175 Å bump (Pei 1992). I therefore extend our study to include a distribution of SMC-like dust ($p = 3.5$ and $0.005 \leq a \leq 0.25$ μm), appropriate for star-forming dwarf galaxies. A distribution of large grains may be more appropriate for dusty regions produced by radiation pressure driven outflows. As I will show below, the brightness and the width of the X-ray scattering halo offers a diagnostic for differentiating between the two dust populations and their relation to quasar absorption systems.

The mass ratio of dust to gas in extragalactic systems may vary with metallicity and size distribution in comparison to that observed locally. I introduce the dust-to-gas number ratio, $k \equiv N_d/N_{\rm H}$, which absorbs the size distribution, metallicity, and dust-to-gas

Table 4.3. Potential dust distributions for the average DLA

Dust Model				
Name	Power	Sizes (μm)	k	τ_x[a]
SMC-like	($p = 3.5$)	$0.005 - 0.25$	3.2×10^{-10}	$\sim 0.5\%$
Large	($p = 4$)	$0.1 - 1.0$	1.7×10^{-13}	$\sim 2\%$
Large	($p = 3$)	$0.1 - 1.0$	6.6×10^{-14}	$\sim 3\%$

[a]Optical depth to X-ray scattering at 1 keV for the column density $N_{\rm HI} = 10^{21}$ cm^{-2} and $z = 0$. Note that $\tau_x \propto k\, E_0^{-2}\, (1 + z_g)^{-2}$.

mass ratio. If I assume that dust abundance is roughly proportional to metal abundance,

$$k = \frac{m_{\rm H}}{\langle m_d \rangle} \left(\frac{M_d}{M_{\rm H}}\right)_{\rm MW} \left(\frac{Z}{Z_\odot}\right) \tag{4.20}$$

where the dust-mass to hydrogen gas-mass ratio of reference is that of the Milky Way, $(M_d/M_{\rm H})_{\rm MW} \approx 0.009$ (Draine 2011). A relatively constant ratio of dust mass to metallicity is observed locally in studies of the Milky Way, LMC, and SMC (Pei 1992). I apply this finding liberally as a means of estimating the magnitude of X-ray scattering by dust reservoirs; it may not well apply for dust in outflows, halo gas, or the IGM. If DLAs are primordial galaxies, dust detection via X-ray scattering provides a check on dust evolution models (e.g. Inoue 2003). Table 4.3 shows the dust-to-gas number ratio and corresponding optical depth for several dust size distributions, assuming $Z = 1/15\ Z_\odot$. Note that the total optical depth to X-ray scattering,

$$\tau_x \propto k\, E_0^{-2}\, (1 + z_g)^{-2}$$

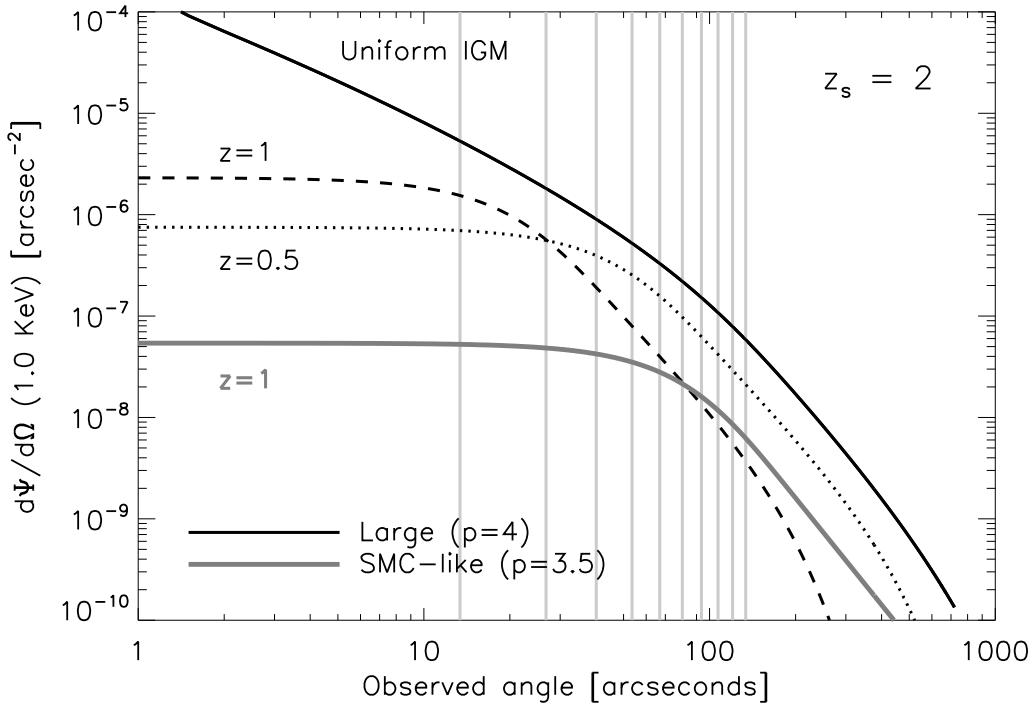

Figure 4.3 Surface brightness profiles for X-ray photons scattered from a DLA-type screen of dust particles and a point source placed at $z_s = 2$. The large dust distributions are shown for screens at $z = 1.0$ (dashed black line) and $z = 0.5$ (dotted black line). For angles $< 10''$, both profiles are flatter than that expected from X-ray scattering through uniformly distributed $\Omega_{\rm dust}^{\rm IGM} = 10^{-5}$ (solid black line). The SMC-like dust distribution is shown for a screen at $z = 1$ (solid grey line). The light grey vertical lines mark the radial size (D_A) of an object at $z = 1$, ranging from 0.1 to 1 Mpc using 100 kpc sized steps.

will scale proportionally with metallicity and gas-to-dust mass ratio.

For 1 keV photons and a source at $z_s = 2$, the scattered surface brightness profiles from an infinitely large screen with the hypothesized dust column densities are shown in Figure 4.3. For comparison, the scattering halo expected from dust distributed uniformly throughout the universe is also shown (solid black). The other black lines show screens at $z = 1$ (dashed) and $z = 0.5$ (dotted) using the Large $p = 4$ dust distribution. The result for a screen of SMC-like dust is also shown (solid grey). When the characteristic scattering angle is smaller (e.g. with higher energy), the halo profile is more centrally focused. This explains why the surface brightness profile for the $z = 1$ (Large dust) screen, despite

having a smaller τ_x, appears brighter than the $z = 0.5$ (Large dust) screen for observation angles $\lesssim 10''$. When the characteristic scattering angle is larger (e.g. with smaller dust grains), the majority of the scattered light is in the wings of the halo profile. Thus the curve from the SMC-like screen appears significantly dimmer than one might expect in relation to the other curves plotted in Figure 4.3.

It is evident from Figure 4.3 that the expected DLA dust column produces a scattering halo that is several orders of magnitude dimmer than what is expected from $\Omega_{\rm dust}^{\rm IGM} \sim 10^{-5}$, particularly within $10''$ of an X-ray point source. Therefore, a *typical* DLA along the line of sight to an X-ray bright quasar would not be identifiable with X-ray scattering unless the total dust density $\Omega_{\rm dust}^{\rm IGM} < 10^{-7} - 10^{-6}$. However, a high-metallicity DLA (or an extreme dust-to-gas ratio) would present a significant dust column density for scattering. The rare DLA with $Z \sim Z_\odot$ (e.g. Fynbo et al. 2011) would have $\tau_x \sim 0.08 - 0.45\ (1 + z_g)^{-2}$, and double-scattering effects will become important. Eleven DLAs with [Zn/H] > -0.5 (roughly correlating with total metallicity) are present in a sample by Prochaska et al. (2007), suggesting $\tau_x \gtrsim 0.02 - 0.14\ (1 + z_g)^{-2}$.

The shape of the halo profile provides a crucial diagnostic for differentiating between a uniformly distributed IGM and a discrete dust source. The uniform IGM case is equivalent to stacking many dust-scattering screens between the source and observer. The more distant screens contribute only to scattering observable at very small angles – close to the point source – giving the radial profile a cusp near the center. For a scattering screen, the halo surface brightness has the same shape as the scattering cross-section (Equation 4.19), which I approximated with a Gaussian function (Equation 1.4). Therefore, the radial

profile of scattered light from a screen is very flat for angles below the characteristic Gaussian width. The turn-over point, at which the brightness profile falls rapidly, is a function of (i) the dust grain size distribution and (ii) the distance between the X-ray point source and dust screen. Dust distributions that are weighted towards smaller grains form broader halos because the differential cross-section allows for larger characteristic scattering angles (Equation 1.5). Wider halos are also observed when the light rays approaching the dusty screen are nearly parallel; in comparison, a screen very close to the X-ray point source must scatter light through larger angles in order to reach the observer.

For a DLA scattering halo to be observable, the dusty region must subtend a large enough angular diameter to be viewed at sizes comparable to the angular width of the scattering cross-section. The angular diameter distance, which describes the physical size of an object viewed at cosmological distances,

$$D_A = \frac{\alpha}{(1+z)} \int_0^z \frac{c\, dz}{H(z)} \tag{4.21}$$

is relatively constant beyond $z \sim 1$, for a fixed observation angle. The light grey vertical lines in Figure 4.3 mark the angular diameter distance for an object at $z = 1$, in 100 kpc steps, from 0.1 to 1 Mpc. Most objects $z \gtrsim 1$ must be larger than 200 kpc for the brightness profile turn-off point to be observed, but DLA systems are tens of kpc large, not hundreds (Pettini 2006). Observable X-ray scattering in the vicinity of quasar absorption systems is likely only if these systems are associated with a nearby galaxy, produce outflows or are a tracer of galactic outflow themselves. If the diffuse distribution of the IGM is sufficiently low, X-ray scattering offers an avenue for exploring the structure around DLAs.

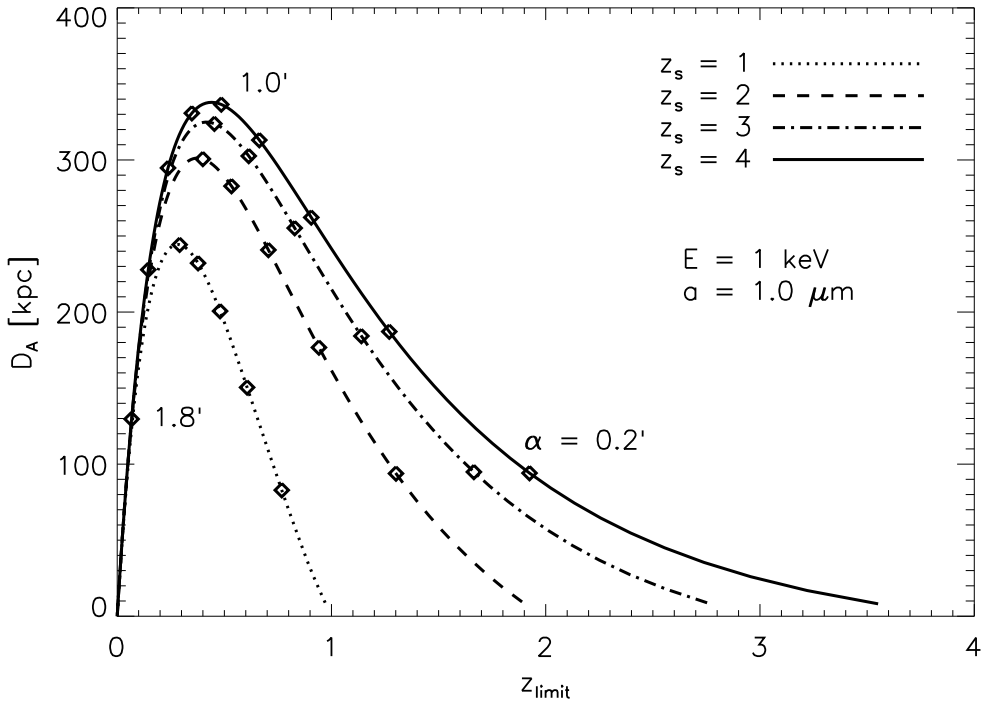

Figure 4.4 The physical radius associated with $z_{\rm limit}$, using a fixed photon energy and grain size. The diamond points mark the observation angle α associated with each $z_{\rm limit}$ in intervals of 0.2′, the values increasing from right to left. For clarity, α points are only plotted up to 1′ on the curves below $z_s = 4$. The results for α and D_A shown here can be scaled by $\sigma_0(\text{arcmin}) \approx 1/(a_{\mu\text{m}} E_{\text{keV}})$.

4.4 Redshift Sensitivity

The ability for a region of dust to scatter light towards an observer depends primarily on the scattering angle and the width the Gaussian distribution in Equation 1.4. I showed with Equation 4.17 that one can imagine all observable scattering is limited to angles $\theta_{\rm eff}$ that fall within a distribution of width $\tilde{\sigma}_0 \equiv \tilde{\sigma}(E_0)$. Most light will scatter within $\theta_{\rm eff} < 2\tilde{\sigma}_0$. Given a particular grain size and energy, for every observation angle α there will be a limiting redshift ($z_{\rm limit}$) beyond which effectively no light will be scattered towards the observer. Smaller observation angles are able to probe regions closer to the X-ray point source, while larger observation angles are sensitive only to regions close to the observer.

For 1 keV photons and 1.0 μm grains, the effective scattering angle is limited by $2\tilde{\sigma}_0 \approx 2'$. Figure 4.4 shows the angular diameter distance D_A for objects as a function of $z_{\rm limit}$ (found by solving $\theta_{\rm eff} = 2\tilde{\sigma}_0$ numerically). The curves border the volume of the IGM that contributes to a scattering halo. Diamond points on each curve mark the observation angle α in 0.2′ sized intervals. To extend the results of Figure 4.4 to other grains sizes and photon energies, the α and D_A values should be scaled by σ_0 in units of arcmin.

The contents of Figure 4.4 give broad insight for the ability of X-ray scattering to probe different regions of the IGM. The contribution to the scattering halo for angles $\alpha > 0.2'$ and a point source at $z_s = 4$ covers a depth $z \lesssim 2$ of a uniformly dusty IGM. An observer who wants to learn more about $z > 2$ dust must be able to measure the halo brightness profile for angles within $\sim 10''$ of the point source center. The maximum for each curve in Figure 4.4 occurs when $\alpha \approx \tilde{\sigma}_0$ (1′). Therefore, the largest detectable extragalactic structures are at $z \sim 0.5$ and have a physical diameter $\sim 500 - 700$ kpc, depending on the redshift of the background point source.

When measuring the width of a scattering halo, there is ambiguity between a large object far away and a small object nearby. From the $z_s = 4$ curve in Figure 4.4, a dusty cloud 200 kpc in radius would create a scattering halo of radius 0.2′ if placed at $z_g = 2$. From Equation 4.21, a 90 kpc cloud at $z_g = 1$ happens to have an angular radius of 0.2′ and would thereby create a scattering halo of comparable size. Knowledge of the object's redshift is required to break the degeneracy between size and distance, making quasars with known absorption systems more favorable candidates for X-ray scattering studies. Due to the nature of small angle scattering, halo light appearing at $\alpha \approx 2\tilde{\sigma}_0$ will always have come

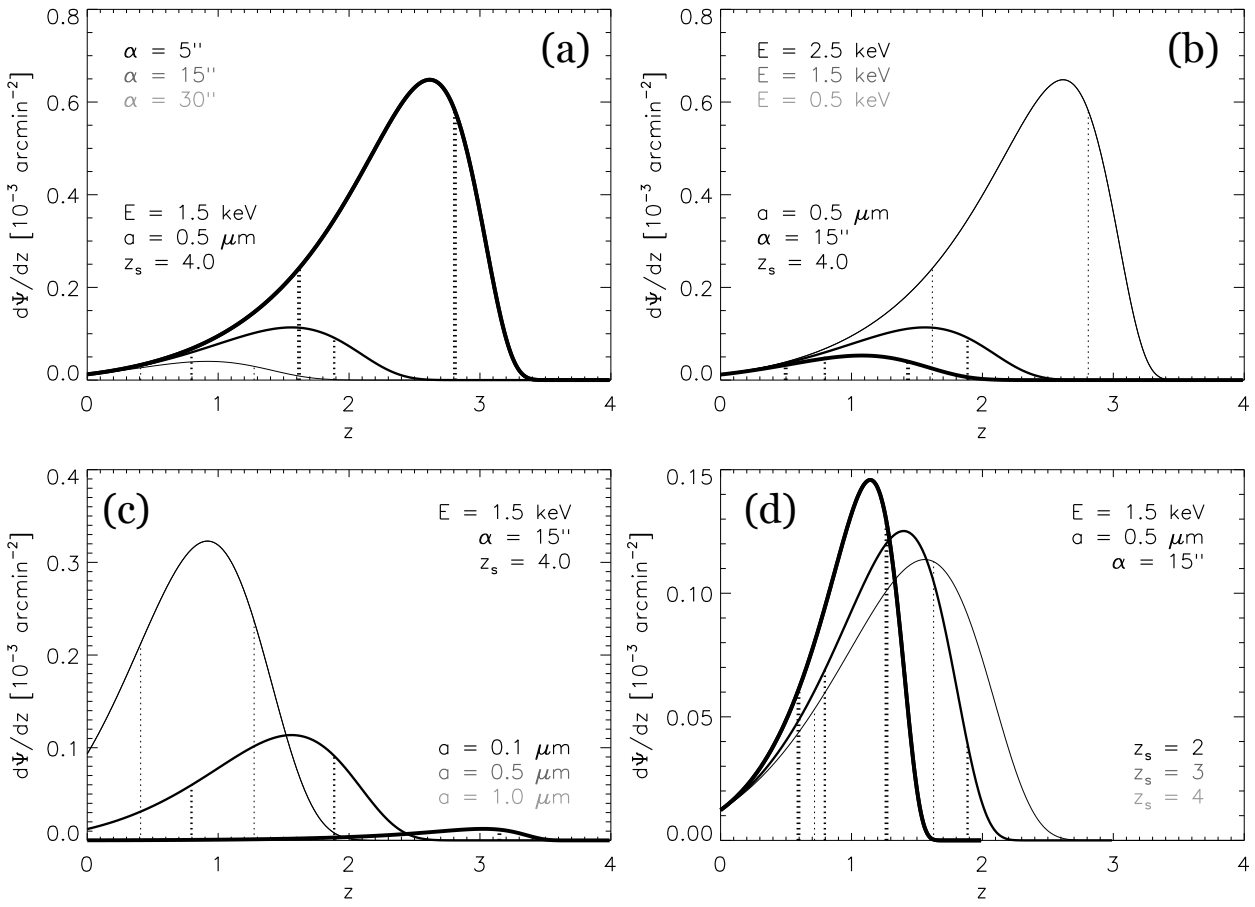

Figure 4.5 The curve $\frac{d}{dz}\left[\frac{d\Psi}{d\Omega}\right]$ as it changes around the case $\alpha = 15''$, $a = 0.5$ μm, $E = 1.5$ keV, and $z_s = 4.0$. The vertical dotted lines mark the central region that encloses 2/3 of the total area under the curve.

from dust close to observer. This fact may help mitigate the effects of foreground dust, which will contribute to the scattering halo several arcminutes from the point source.

Each annulus of an X-ray scattering halo image is sensitive to the interplay of several parameters (a, E, and z). I examine the curve

$$\frac{d}{dz}\left[\frac{d\Psi}{d\Omega}\right] \propto a^6\ \Omega_{\rm dust}^{\rm IGM}\ \frac{(1+z)^2}{x^2\ H(z)}\ \exp\left(\frac{-\theta_{\rm eff}^2}{2\tilde{\sigma}_0^2}\right) \tag{4.22}$$

to gain further insight. For small values of x (i.e. dust very near the point source),

the exponential term becomes very large and the curve asymptotically approaches zero. The effective scattering angle determines where the curve will turn over and thus which region of redshift which will contribute most to the integral. Photons that are able to scatter through larger angles will allow sensitivity that extends to higher redshift gas.

Figure 4.5 shows Equation 4.22 for different combinations of α, a, E, and z_s. I choose $\alpha = 15''$, $E = 1.5$ keV, $a = 0.5$ μm, and $z_s = 4$ as fiducial values, around which each parameter was varied. The curves reach a maximum at intermediate redshift, but are often asymmetric. The vertical dotted lines demarcate the central region for which the area under the curve equals 2/3 of the total integrated brightness at the respective observation angle.

Light that scatters close to the point source must generally go through large scattering angles to be observed. Therefore, scattered light observed at small angular distances from the point source center predominantly traces gas closer to the source (Figure 4.5a). For the same reason – low photon energies, which can scatter through larger angles, will be able to probe gas closer to the point-source (Figure 4.5b). The curves in Figure 4.5b are degenerate with Figure 4.5a because the width of the Gaussian, $\tilde{\sigma} \propto \alpha/E$. Large dust grains, which are more strongly forward scattering than small dust grains, will only contribute observable scattering from regions of low redshift. This is because gas close to the observer receives light rays that are nearly parallel to the line between the observer and point-source, making the required scattering angle for observation lower compared to dust at intermediate distances (Figure 4.5c). Finally, viewing a source at smaller redshift will probe gas closer the observer. However, the shift in region sensitivity

is small; scattering halos around objects at $z = 2 - 4$ are mostly sensitive to dust in the $z = 0.5 - 2$ range (Figure 4.5d). It is interesting that reducing the point source's redshift (z_s) does not dramatically change the redshift range to which the halo image is sensitive. A campaign that uses image stacking to search for an X-ray scattering halo could therefore use broad bins in z.

4.4.1 Constraints on IGM homogeneity

Figure 4.4 can also be used to place constraints on the homogeneity of the IGM. If a scattering halo is asymmetrical on an annulus $\sim$ 1 arcminute in size, the dust distribution must be inhomogeneous on $\sim$ 300 kpc scale. A symmetric scattering halo would thus indicate a population of dust grains that is smoothly distributed. Observation angles around 10″ correspond to spatial homogeneity $\sim 100 - 200$ kpc in diameter. A scattering halo that appears asymmetrical across a 10″ annulus would thus indicate that the dust being probed is confined to the gaseous regions of a galactic halo, potentially part of an outflow.

To illustrate, galactic winds $\sim$ 100 km/s would travel about 100 kpc per Gyr. As a first approximation (and upper limit), the distance traveled by a dust particle that has escaped the potential well of its parent galaxy (at z_2) and is thus not subject to any appreciable force of gravity, is

$$\int_{z_1}^{z_2} \frac{v\, dz}{(1+z)\, H(z)} \tag{4.23}$$

where v is the terminal velocity of the particle. Assuming $v \sim 100$ km/s for particles that have been ejected from a small galaxy at $z = 2$, a dust grain would travel $\sim$ 200 kpc by

$z = 1$.

Note that if a 200 kpc thick shell of ejected dust continued to expand freely, it would be ~ 1 Mpc in radius by $z = 0$ and about 75 times less dense than it was was at $z = 1$. A comparable amount of dust grains uniformly distributed throughout the IGM would become less dense by a factor of 8 between $z = 1$ and $z = 0$. This means that if a uniformly distributed population of intergalactic dust is observed, it is more likely to have been distributed during the epoch $z \gtrsim 3$ than from $z < 2$ galaxy outflows, which dominate the region $R \lesssim 100$ kpc around them.

4.4.2 Constraints on quasar variability

Scattered photons must travel a slightly longer distance than non-scattered photons before reaching the observer. For small angles, this path difference:

$$\Delta\chi \approx \chi_{os}\, \alpha^2\, (1 - x) \tag{4.24}$$

requires knowledge about the distance to the dust grain. Below the value $x = \alpha/2\tilde{\sigma}$, almost no light will be scattered into the observer's line of sight. Substituting this into Equation 4.24 and recognizing that the *maximum* path difference occurs for observation angles $\sim \tilde{\sigma}$, I get

$$\Delta\chi_{\max} \sim 4.5 \text{ kpc} \left(\frac{\chi_{os}}{\text{Gpc}}\right)\left(\frac{E}{\text{keV}}\right)^{-2}\left(\frac{a}{0.1\ \mu\text{m}}\right)^{-2} \tag{4.25}$$

for choices of E and a that give large $\tilde{\sigma}$.

The extra distance traveled by a scattered photon leads to a time delay $\Delta t \sim 10^4$ years,

which is much shorter than the suggested quasar lifetime, $\sim 10^6 - 10^8$ years (Martini 2004). It is therefore unlikely for an X-ray scattering halo to be truncated due to a particular quasar's activity switching "on" recently. However, dramatic variations in a quasar's brightness on $\leq 10^4$ year timescales would become apparent if a scattering halo exhibit radial variation. The region of observable scattering from a short burst of X-ray light takes the shape of an elliptical shell expanding with time. Thereby a ring of increased (or decreased) surface brightness appearing around a quasar would indicate a fluctuation in accretion rate, offering a means to constrain the long-term variability of AGN activity (e.g. Miralda-Escudé 1999).

4.5 Comparison to Petric et al. (2006)

High spatial angular resolution coupled with a focusing power that confines $\sim$ 99% of point-source light to a 2″ (4 pixel) radius makes *Chandra* the best X-ray observatory in operation today for observing scattering halos. The relatively narrow point-source function (PSF) assures that there is enough contrast between the source and background to observe an accumulation of dust-scattered photons a small angular distance away. As illustrated below, the most difficult part about observing scattering halos due to intergalactic dust is obtaining a statistically significant number of photon counts with respect to the models.

Petric et al. (2006) used the non-detection of an X-ray halo image around QSO 1508+5714, a bright quasar $\sim 10^{-13}$ erg/s/cm^2 at $z = 4.3$, to place the limit $\Omega_{\rm dust}^{\rm IGM} < 2 \times 10^{-6}$. They did this by comparing the expected halo brightness from a dust population of 1.0 μm size grains to the brightness of the PSF wings predicted by MARX (a ray-trace simulation)

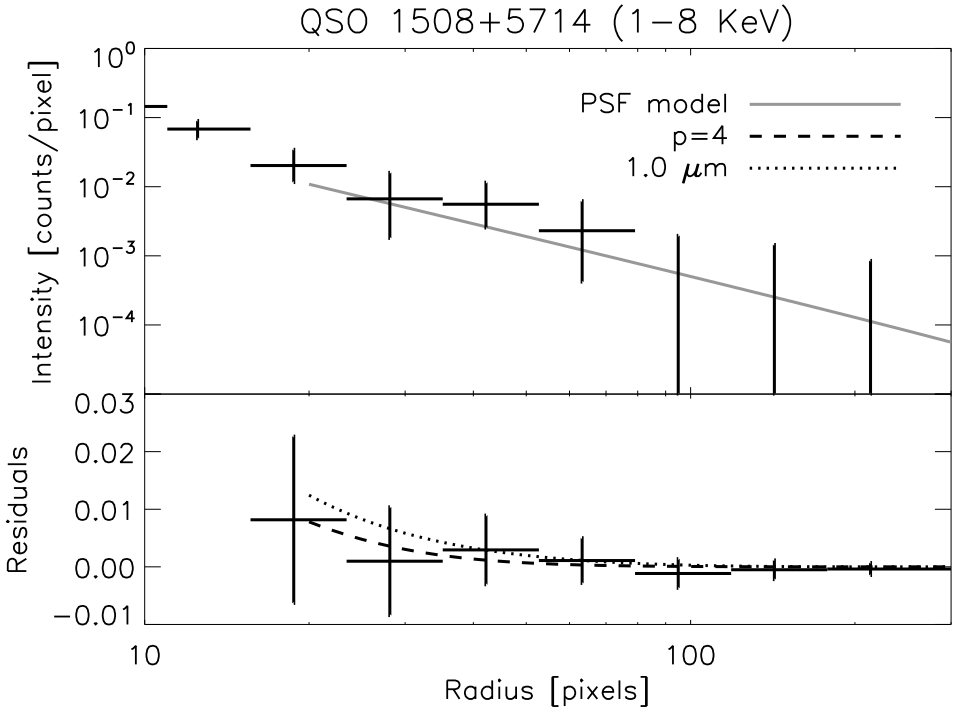

Figure 4.6 (*Top*:) The radial profile for QSO 1508+5714 in the 1-8 keV range, with the model point-spread function in grey. (*Bottom*:) The residual intensity after subtracting the PSF model of Gaetz et al. (2004), compared to the intensity expected from a $p = 4$ power-law distribution of grey dust (dashed line) and 1 μm size grains (dotted line) with total mass density $\Omega_{\rm dust}^{\rm IGM} = 10^{-5}$.

and the wings from a previous *Chandra* observation of 3C 273. The number of scattered photons expected from 1.0 μm dust is several times that expected from a distribution of dust grain sizes, allowing us to relax their constraints.

The reliability of MARX to simulate the *Chandra* PSF wings is uncertain. High energy X-rays are more subject to deviations in scattering by micro-roughness in the high resolution mirror assembly (HRMA) and require smaller grazing incidence angles that are difficult to obtain while testing the HRMA on the ground. In addition, appropriately determining the relative brightness of the PSF wings from objects like 3C 273 is difficult due to pile-up – that is, the tendency of the *Chandra* CCD instrumentation to register an incorrect photon energy or mistake multiple photon events for a cosmic ray – which occurs

Table 4.4. Observed and expected properties for QSO 1508+5714 and its scattering halo

Energy (keV)	$N_{\rm obs}^{\rm src}(<2'')$[a]	$N_{\rm exp}^{\rm sca}(10-500'')$[b]	$N_{\rm bkg}$[c]
0.3 - 1.0	1943	375 (38)[d]	24809
1.0 - 2.0	1915	32	15074
2.0 - 3.0	637	3	12247
3.0 - 4.0	368	1	8479

[a]Number of counts observed within a 2″ radius of point source center.

[b]The total number of scattered counts expected to be observed in the region 10″ – 500″ away from the point source, rounded to the nearest integer.

[c]The estimated number of background counts, extracted from a circular region on the same image, for an area covered by an annulus 10 – 500″ wide.

[d]With a factor of 10 reduction due to absorption.

for bright objects ($\gtrsim 1$ X-ray photon per second). Pile-up causes an obvious depression of counts in the center of 3C 273, prevents the accurate measurement of source flux, and thereby degrades the accuracy of the radial profile within $\sim 10''$, or 20 pixels (Gaetz et al. 2004). Since the radial profile from 3C 273 appears to match QSO 1508+5714 best around 5″ (10 pixels), the extrapolated wing profile is more likely to be an overestimate of the true PSF – perhaps explaining why the intensity from 3C 273 matches the upper limits on the instrumental measurement between 30 – 60″ (Petric et al. 2006, Fig. 2).

I use the PSF calibration model by Gaetz et al. (2004) to gauge the PSF + halo profile that would have resulted from the $p = 4$ dust distribution with density $\Omega_{\rm dust}^{\rm IGM} = 10^{-5}$. A quick examination of QSO 1508+5714 (obsid 2241) using a circular region with a 4 pixel

radius yields approximately 5400 counts in the 0.3-8 keV range. (This is a lower limit to the total number of source counts, as it does not consider counts spread into the PSF.) For several energy bins, Table 4.4 shows the number of point source counts, expected number of halo counts in an annulus $10 - 500''$ centered on the point source, and the number of background counts expected in that same region. The majority of the scattered light will have photon energies < 2 keV. However, for soft X-rays (< 1 keV) and large dust grains, the RG cross-section can overestimate the intensity of scattering by a factor ~ 10 due to absorption by grain material (Smith & Dwek 1998). For this reason, the 375 scattered counts expected in the $10 - 500''$ annular region are likely too large by an order of magnitude. I therefore exclude photon energies below 1 keV from further evaluation. To take advantage of the soft X-ray band, the halo profile must be modeled with Mie scattering.

Figure 4.6 compares the radial brightness profile of QSO 1508+5714 in the 1-8 keV energy band to the PSF and dust models. The magnitude of the error bars show that the observations of Petric et al. (2006) are consistent with $\Omega_{\rm dust}^{\rm IGM} \lesssim 10^{-5}$ for the power-law distribution of dust grains chosen. However, the brightness profile is also consistent with a population of IGM dust composed purely of 1 μm sized grains. By including energies below 1 keV and using the RG cross-section, Petric et al. (2006) were expecting a much brighter X-ray halo. This was an overestimate leading to the limit $\Omega_{\rm dust}^{\rm IGM} < 2 \times 10^{-6}$, which our analysis shows can be relaxed to $\Omega_{\rm dust}^{\rm IGM} \leq 10^{-5}$. This emphasizes the need for a more detailed modeling, incorporating statistics and Mie scattering, to be implemented in the future. An even more important task would be the careful calibration of the *Chandra*

HRMA PSF between 1 and 20″.

4.6 Discussion

X-ray scattering provides a unique view of the cosmic history of star formation, feedback, and the IGM that is complementary to UV, optical, and infrared studies. A summary of the main results are as follows:

(i) If dust is evenly distributed throughout the IGM, with $\Omega_{\rm dust}^{\rm IGM} = 10^{-5}$, the dust-scattered X-ray light will be $\sim 5\%$ ($E_{\rm keV}^{-2}$) of the point source brightness for objects at $z \geq 2$. The intensity of the scattered light is directly proportional to $\Omega_{\rm dust}^{\rm IGM}$.

(ii) Also in the uniform IGM case, point sources at larger values of z trade larger dust column densities for a narrower halo profile, making it slightly more difficult to distinguish scattered light from the point source.

(iii) For high-z point sources, scattered light comes predominantly from intergalactic dust at $z \lesssim 2$. If the majority of IGM dust came from star formation within sub-L* galaxies at $z > 3$, assuming a constant comoving density of dust grains may still be reasonable for point sources at $z = 4$.

(iv) If X-ray light scatters through a dense, dusty clump in intergalactic space, the resulting halo image will have a flatter radial profile compared to the uniformly distributed case. The further away the clump is from the background point-source, the larger the halo image will appear to an observer.

(v) If the dust mass to metallicity ratio is relatively constant, as observed locally, then a typical DLA will have an optical depth to 1 keV X-ray scattering $\sim 1 - 3\%$, proportional

to $(1 + z_g)^{-2}$. This result scales proportionally with metallicity, so DLAs with near-solar abundances may have $\tau_x \gtrsim 5\%$.

(vi) Dusty clumps at $z \gtrsim 1$ would have to be ≥ 200 kpc in size for a halo image to appear at angles larger than 10″ from the point source center. X-ray scattering thus offers the opportunity to test if dusty outflows exist near quasar absorption systems, but the outflow may require column densities of dust that are so far unprecedented. Perhaps an X-ray point source whose line of sight is close to a foreground galaxy can test the ability of large grains to be expelled from L* galaxies.

(vii) A scattering halo that is symmetric on an annulus of radius $\geq 60''$, would indicate that IGM dust is distributed uniformly. A scattering halo that is asymmetric on an annulus of radius 10″ would indicate the the dust distribution is traced mainly by galaxies ($R \lesssim 50$ kpc) and is not distributed very far out in the galactic halo potential or the IGM. Either result would provide clues to galactic and star formation feedback mechanisms.

(viii) The previous constraint of $\Omega_{\rm dust}^{\rm IGM} < 2 \times 10^{-6}$ must be relaxed when considering the absorption of X-ray light below 1 keV. Photons observed at 0.5 keV today will be shifted above 1 keV for $z \gtrsim 1$, but in Section 4.4 I showed that the scattering halo is more sensitive to material at $z \lesssim 2$ and large dust grains at low redshift. Therefore, what would be the dominant contribution to the scattering calculation, X-rays < 1 keV and 1 μm sized grains, is overestimated by Rayleigh-Gans scattering. Deeper observation of high redshift quasars, in conjunction with a more careful calculation involving the Mie scattering solution, is required to place a stronger constraint on the intergalactic dust distribution.

Table 4.5. Systematic offset in magnitude for an intergalactic population of grey graphitic grains

	(**p** = **3**)		(**p** = **4**)	
z	A_V	$A_{1.78}$	A_V	$A_{1.78}$
0.50	0.008	0.007	0.012	0.010
1.00	0.010	0.010	0.017	0.014
2.00	0.012	0.012	0.019	0.017
4.00	0.013	0.013	0.021	0.019

To conclude, I briefly note that the dust models used throughout this paper would create meaningful systematic errors for both optical and infrared extragalactic surveys. Intergalactic dust dims the most distant objects, and if not accounted for, would affect cosmologists' ability to place more stringent constraints on dark energy models. A systematic shift as low as $\delta m \sim 0.02$ would reduce the effectiveness of future supernovae surveys to constrain the dark energy equation of state parameter w (Virey & Ealet 2007). A systematic shift in magnitude roughly correlates as $\delta m \sim -0.5\ \delta w$ and $\delta m \sim -\ \delta\Omega_M$ for $z \lesssim 1$ (e.g. Zhang 2008; Ménard et al. 2010a; Corasaniti 2006). Thus an extinction offset $\sim 1\%$ would create an offset comparable to the error bars sought after in precision cosmology.

A distribution of graphitic grains larger than 0.1 μm is grey even to the reddest filters (0.893 μm and 1.78 μm) to be used in cosmological supernovae surveys (LSST and WFIRST, respectively). I calculate the systematic offset in magnitude for our grey graphitic grain models using $\Omega_{\rm dust}^{\rm IGM} = 10^{-5}$ (Table 4.5).There is little offset between A_V and $A_{1.78}$ – the extinction at 1.78 μm – which is the center of the reddest filter on the WFIRST mission (Green et al. 2011). For supernovae surveys beyond $z > 1$, $\delta m \sim 0.01 - 0.02$ in both the visual and infrared bands. Such small systematic offsets would call for a deep

field survey, rather than wide field survey that increases the precision of the photometric measurements but not their accuracy (Virey & Ealet 2007). Observational searches for X-ray scattering halos due to intergalactic dust would constrain these systematic offsets and help determine the best future course of action for large-scale optical and infrared cosmological surveys.

Finally, I note that the values in Table 4.5 differ by those calculated by Aguirre (1999) for a similar cosmic density of intergalactic dust. For the model $p = 4$ graphite grain distribution, $\kappa_V = 2.4 \times 10^4$ cm^2/g. Using this value with $\Omega_{\rm dust}^{\rm IGM} = 10^{-5}$ in Equation 9 of Aguirre (1999) implies $A_V(z = 0.5) \sim 0.02$. However, Aguirre uses $\Omega_m = 0.2$ and $\Omega_\Lambda = 0$. In that case, the distance (and hence the column density) one would calculate for $z = 0.5$ is larger by a factor of two than that in the currently accepted ΛCDM universe. This brings previous work into agreement with the results shown in Table 4.5.

(This page left intentionally blank.)

Chapter 5

Conclusion

Throughout this work I have shown that X-ray light scattered by intervening dust grains can test for the presence of large grains that are difficult to probe at other wavelengths. *Chandra* provides X-ray imaging resolution that is unsurpassed, making it essential for probing the inner portion of a scattering halo, which is most sensitive to large grains and dusty material near the X-ray source. While Galactic scattering halos are around 10-30% as bright as the point source illuminating the dust, intergalactic scattering halos are just 1-3% as bright. This makes careful accounting of the *Chandra* point spread function (PSF) essential, because a similar fraction (2-5%) of point source light is scattered due to micro-roughness on the mirror surfaces. Unfortunately this task is complicated by the non-linear effect of photon pileup.

Chandra images utilizing the High Energy Transmission Grating (HETG) provide an accurate spectrum from the grating dispersed light, removing mystery surrounding PSF normalization. In Chapter 2 I used three bright sources with dust-free sight lines to

directly measure the pileup fraction, demonstrating that grade migration in HETG images, used to gauge the degree of pileup (Gaetz et al. 2004), is not typically accurate. I derived a universal HETG PSF wing model that fits all objects in the region 5 – 100″ away from the point source center. An accurate description of the PSF can be extended down to 1.5″ by including the PSF core model fit to the least piled object in my study, QSO B1028+511. This model appears to work well for heavily piled sources such as 3C 273. Thus Chapter 2 has laid the ground work for future studies of Milky Way dust, possible with about a dozen HETG imaged scattering halos currently available in the *Chandra* archive.

In Chapter 3 I demonstrated how a single X-ray scattering halo surface brightness profile can be used to measure dust mass, grain size, and spatial distribution along the line of sight. A future study of bright X-ray scattering halos will probe the abundance of large ISM grains necessary for calibration of dust mass, extinction (A_V), reddening (R_V), and distances to X-ray binaries. Searching for large dust grains also gauges the effectiveness of growth and destruction mechanisms in the diffuse ISM, which are still highly uncertain. The high resolution spectrum of Cyg X-3 is littered with emission lines, but objects with smoother spectra will contain photoelectric absorption edges, the signature left by metals in the interstellar medium (ISM). The depth of photoelectric absorption edges directly measures the abundance of gas plus dust phase elements along the line of sight to an X-ray binary (Wilms et al. 2000). A small survey of Galactic objects with deep absorption edges will yield a column density for individual elements (e.g. O, Mg, Si, Fe) and a dust-to-metal mass ratio, directly measuring the depletion of gas phase elements into dust grains without assuming a mix of interstellar metals. This information is useful for

understanding the chemical processes of the diffuse ISM and dust grains.

In Chapter 4 I examined whether X-ray scattering could probe for dust in known intergalactic reservoirs of cold gas – quasar absorption line systems – or from an intergalactic medium (IGM) uniformly suffused with dust. I showed that the $\Omega_{\rm dust}^{\rm IGM} < 2\times10^{-6}$ constraint from Petric et al. (2006) could be relaxed because the Rayleigh Gans approximation is not applicable for grey dust that would affect the photometry of high precision dark energy surveys such as the Wide Field Infrared Survey Telescope (WFIRST, Green et al. 2012) and the DES Supernova Survey (Bernstein et al. 2012). Determining the X-ray scattering cross section of micron-sized dust requires the full Mie scattering solution instead, which can reduce the scattering efficiency by a factor of 10 or more.

I have successfully implemented Mie scattering in a cosmological context using the Bohren and Huffman subroutine, versions of which are publicly available.[1] These results, as well as the prospects for observing extragalactic dust via X-ray scattering, will be visited in Section 5.1. My scattering and extinction code, implemented in python and now publicly available on github, produced a large fraction of the figures in this text. I will provide a summary of the code modules and essential functions in Section 5.2.

5.1 Future Prospects for Observing Intergalactic Dust

Since galaxies do not evolve in a closed box, their metals likely escape into the circumgalactic medium (CGM) or the IGM, depending on the depth of their potential wells (Bouché et al. 2007; Peeples et al. 2014). Dust, accounting for some fraction of the metals, may also

[1]See for example http://www.astro.princeton.edu/~draine/scattering.html

play an essential role in the feedback processes governing galaxy structure and evolution. Dust gives ISM material the opacity necessary to allow radiation pressure driven winds to eject material from a galaxy disk (Murray et al. 2005). Relics of this process may be resting in the furthest reaches of dark matter halos or sitting passively in intergalactic space. Assessing the abundance of extragalactic dust will therefore provide insight for the evolution of the Universe, from the production of metals by star formation to their dissemination into intergalactic space, tracing the mechanisms of galaxy evolution.

The amount of dust and metals predicted from the star formation history of the Universe does not currently match the amount of dust and metals observed thus far. Ménard & Fukugita (2012, hereafter MF12) examine the evolution of dust reservoirs, from strong MgII absorbers at high redshift to the dust found in galaxies today. They predict an excess of dust $\Omega_d \sim 7 \times 10^{-6}$ outside of galaxy disks at the present time.

There is also substantial observational evidence that dust escapes galaxy disks to reside in galaxy halos. A reddening signature from CGM dust has also been found at distances far from galaxy disks. Using over 10^7 objects from the Sloan Digital Sky Survey, Ménard et al. (2010c, hereafter M10) calculated the average quasar color as a function of impact parameter to a foreground galaxy. They found a reddening trend out to distances as large as 1 Mpc from galaxy centers. This led them to conclude that the mass of dust in galactic halos is comparable to that in galaxy disks. Recent work by Peek, Ménard, and Corrales (2014, in prep) repeats the experiment with galaxy-galaxy pairs and comes to a similar conclusion, but finds excess reddening within 150 kpc of a galaxy. Large angle UV scattering from dust directly above the mid-plane of star forming galaxies has also

been observed 10-20 kpc from the disk (Hodges-Kluck & Bregman 2014). Merging the observations with theories of feedback, cosmological simulations that include the effect of pressure driven galactic winds are able to reproduce the results of M10 using a dust-to-metals ratio of 0.29 (Zu et al. 2011), which is consistent with the properties of local interstellar material.

It is interesting that CGM dust produces a reddening signal, as I have strongly emphasized the likely 'grey' nature of dust expelled from galaxies. The small end of a grain size distribution, which leads to a larger color change, is not expected to survive expulsion processes through hot gas (Draine & Salpeter 1979). Several studies have followed the trajectory of individual dust grains subject to the forces of radiation, gravity, and gas drag from galaxy disks to the CGM (Ferrara et al. 1991b; Davies et al. 1998b). They find that only grains with $a \sim 0.1$ μm are accelerated to galactic escape velocities *and* able to survive entrainment through the CGM. However once dust grains are at relative rest with the low-density (10^{-5} cm^{-3}) and hot (10^6 K) environment of the CGM, they can survive $\sim 10^{10}$ (a/0.1 μm) years (Draine 2011). There are several ways in which one can explain the red CGM dust found thus far:

(i) the optical extinction studies described above are probing a limited portion of CGM dust population;

(ii) dust removed from the galaxy disk via feedback mechanisms may be subject to grain shattering by shocks, producing a distribution that is similar to that of the ISM but lacking in large dust grains (Jones et al. 1996); or

(iii) due to the force balance of radiation pressure and gravity, small grains are trapped

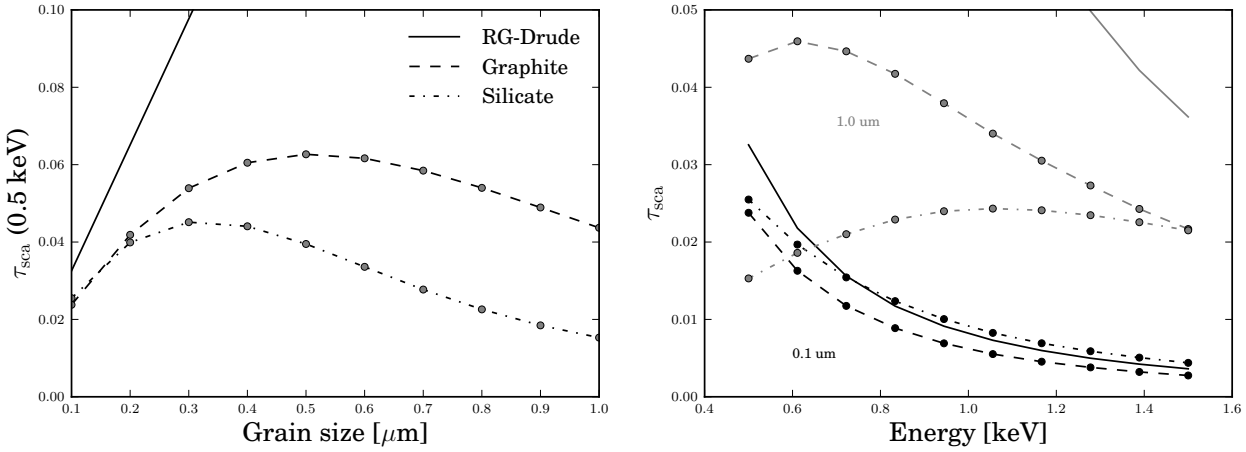

Figure 5.1 The X-ray scattering cross section is plotted for a $z_s = 2$ point source and $\Omega_{\rm dust}^{\rm IGM} = 10^{-5}$. The 0.5 keV Mie scattering cross section for a single sized grain population is shown for graphite and silicate grains. *Right:* The scattering cross-section for 0.1 μm (*dark curves*) and 1.0 μm (*light curves*) is shown as a function of energy. While the RG-Drude approximation is roughly appropriate for small grains and $E < 0.8$ keV, it vastly over predicts the scattering expected from 1 μm sized grains.

in galaxy halos while grains $\gtrsim 0.1$ μm escape to greater distances (Greenberg et al. 1987b; Ferrara et al. 1991b).

Since a significant portion of cosmic dust remains unaccounted for, I return here to calculating the optical depth of the IGM to X-ray scattering. Using $\Omega_{\rm dust}^{\rm IGM} = 10^{-5}$ as an upper limit, Figure 5.1 plots the $\tau_{\rm sca}$ for a variety of grain sizes and energies. The RG-Drude approximation, plotted with solid lines, hugely overestimates the scattering strength of 1 μm dust grains, but is still fairly appropriate if the IGM is suffused with 0.1 μm grains. Regardless, the total optical depth to scattering is expected to be $\sim 1-5\%$, scaling linearly with $(\Omega_{\rm dust}^{\rm IGM}/10^{-5})$.

Using $\Omega_{\rm dust}^{\rm IGM} \approx 3 \times 10^{-6}$ at $z = 0.3$ (MF12), where the dust scattering experiment is more sensitive (Corrales & Paerels 2012), Figure 5.2 plots the 1 keV dust scattering intensity expected around a $z = 2$ quasar relative to the *Chandra* PSF model of Gaetz

et al. (2004). Light from a distant quasar might also interact with dust in the CGM of a foreground galaxy. For a sight line 70-100 kpc from a galaxy disk, M10 found a mass column of dust $\sim 2-3\times10^{-7}$ g cm^{-2}. Figure 5.2 plots the 1 keV scattering halos expected for MRN versus grey dust around a $z = 0.1$ galaxy. In all the cases shown, IGM dust scattered light is still too dim to observe with *Chandra*, which is unsurpassed in focusing power. The chances for detecting intergalactic dust through X-ray scattering appears nonexistent, but may be achieved under very special circumstances.

Active galactic nuclei (AGN), of which quasars are a subset, are known to exhibit 10 – 100% variations in brightness (e.g. Soldi et al. 2014; Lanzuisi et al. 2014). However, these measurements are from month- to year-long timescales; little is known observationally about the duration of a typical AGN phase and the magnitude of long term ($10^3 - 10^9$ year) variability. Because scattered X-rays take a longer path, there is a time delay between the non-scattered point source light and that seen from the scattering halo. Intergalactic scales yield a time delay $\sim 10^4$ years, making them highly sensitive to long term variations in quasar brightness. Observing a quasar that has just recently dimmed by a factor $\gtrsim 1000$ will suppress the PSF brightness, making visible an *X-ray scattering echo* from the AGN's past.

At present, only theory has been able to touch the subject of AGN variability on 10,000 year timescales. Feedback from jets or the energy release from accretion onto the supermassive black hole powering an AGN are sometimes invoked to explain galaxy scaling relations and theories of black hole growth. For applications to IGM dust scattering, I am more concerned with AGN light curves. The mass accretion rate onto a

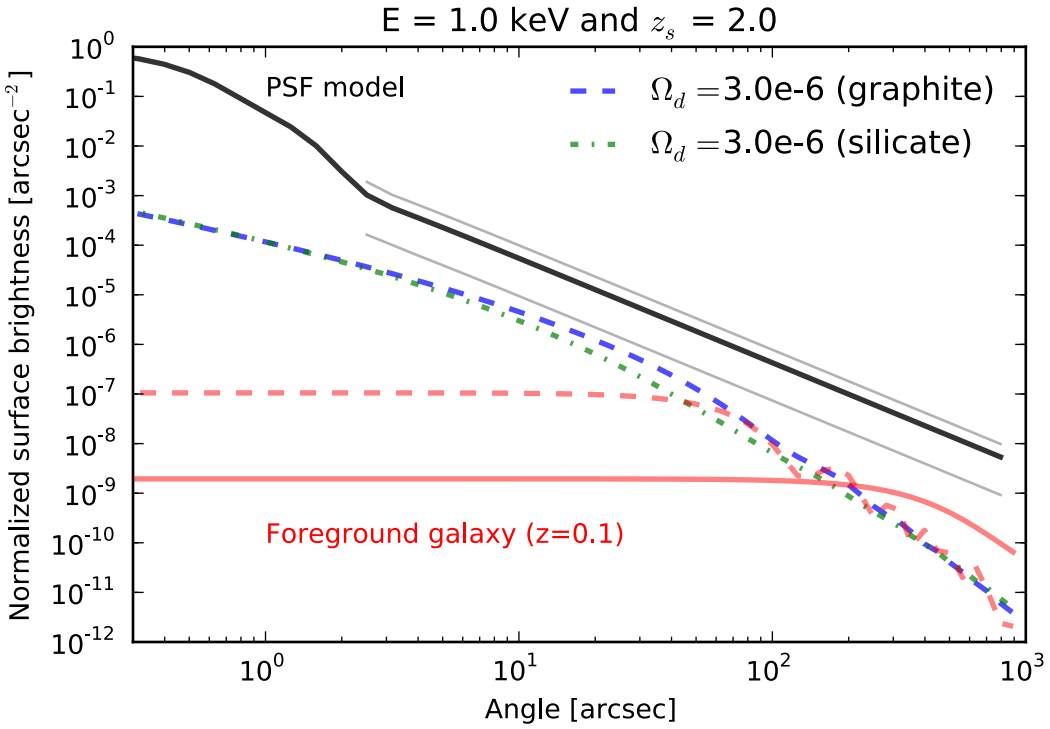

Figure 5.2 The 1 keV intensity for intergalactic scattering halos around a z_s = 2 source is plotted in comparison to the *Chandra* PSF model (Gaetz et al. 2004). The Mie scattering halo from uniformly distributed 1 μm sized IGM dust is shown for silicate (*green dash-dotted curve*) and graphite grains (*blue dashed line*). A dust column consistent with the results of M10 ($M_d = 3 \times 10^{-7}$ g cm^{-2}) around a $z = 0.1$ foreground galaxy is simulated with a screen containing reddening MRN dust (*solid red curve*) or an equal mass of 1 μm sized dust (*dashed red curve*), an upper limit. The approximate uncertainty in the PSF model wings is delineated with light grey lines.

black hole is a proxy for AGN luminosity, assuming some fraction of the gravitational energy released by in-falling material escapes in the form of light. Novak et al. (2011) undertook two-dimensional simulations of AGN accretion and feedback, producing light curves with substantial variation. Their simulation shows that feedback from a burst of activity would cause the AGN accretion rate to fall quickly, but through Rayleigh-Taylor instabilities more gas falls in on Myr timescales to replenish the accretion disk. The power

spectrum obtained from the simulation resembles that of white noise – having no distinct underlying timescale, making it difficult to predict precisely how often a quasar luminosity should take a sudden drop. Regardless, the abrupt and extreme drops in luminosity (Novak et al. 2011, Figure 6), are exactly the kind necessary to produce an X-ray scattering echo.

Figure 5.2 can be used to estimate whether an X-ray scattering echo will be visible above the typical X-ray background. For *Chandra* observations, the 0.5-2 keV background is ~ 0.1 ct/s/chip (CPOG), or $\mathcal{SB}_{\rm bkg} \approx 4\times10^{-7}$ counts per second per square arcsecond. The brightness of an X-ray scattering halo is directly proportional to apparent flux of point source. Using the relation for the halo intensity,

$$I_h(\alpha) = \frac{d\Psi}{d\Omega}(\alpha)\, F_a \tag{5.1}$$

where F_a is the apparent flux of the central point source, how bright must a distant quasar be to illuminate intergalactic dust above typical background levels? The intergalactic dust scattering halo should be easiest to find at observation angles $\alpha \approx 5''$, with $d\Psi_5/d\Omega \sim 10^{-5}$ arcsec^{-2} for IGM dust and $\sim 10^{-7}$ arcsec^{-2} for grey CGM dust. Table 5.1 lists the quasar flux required to illuminate the IGM such that the $\alpha = 5''$ dust scattering halo is brighter than the background,

$$F_{\rm ps} \geq \mathcal{SB}_{\rm bkg} \div \frac{d\Psi_5}{d\Omega} \tag{5.2}$$

Table 5.1. Quasar flux thresholds for creating observable halos

Dust type	**Above background** ct/s	(erg cm^{-2} s^{-1})	**3σ detection in 50 ks** ct/s	(erg cm^{-2} s^{-1})
1 μm IGM grains	0.04	$(\mathbf{3 \times 10^{-13}})$	0.2	$(\sim 10^{-12})$
1 μm CGM grains	4	(3×10^{-11})	20	$(\sim 10^{-10})$

and capable of a 3σ detection within a 5″ region using 50 ks of exposure time ($T_{\rm exp}$),

$$\pi(5'')^2 \, \frac{d\Psi_5}{d\Omega} \, F_{\rm ps} \, T_{\rm exp} \geq 9 \text{ counts} \tag{5.3}$$

The *Chandra* ACIS effective area around 1 keV, 250 cm^2, is used to convert from counts to flux. The HETG zeroth order effective area is a factor of ten lower than grating free ACIS observations, increasing the flux requirements in Table 5.1 by a factor of ten. Combining Equations 5.2 and 5.3, at least 30 ks of exposure time is required to detect *any* halo of minimum surface brightness $\sim \mathcal{SB}_{\rm bkg}$.

Since 10,000 years is short compared to cosmological time scales, properties of the quasar population today should describe the quasar population capable of producing X-ray scattering echoes. I examined sources from the ROSAT All Sky Survey Bright Sources Catalog (RASS BSC, Voges et al. 1999), which has a limiting flux around 5×10^{-13} erg cm^{-2} s^{-1}. All objects in the catalog meet the minimum requirement bolded in Table 5.1. I cross-referenced RASS BSC with the Million Quasars Catalog (Flesch 2014), the results of which are plotted with open circles in Figure 5.3. I also examined objects from the *rassdssagn*[2] catalog (Anderson et al. 2007), which provides depth rather than breadth. Approximately

[2]ROSAT All-Sky Survey and SDSS DR5 Sample of X-Ray Emitting AGN

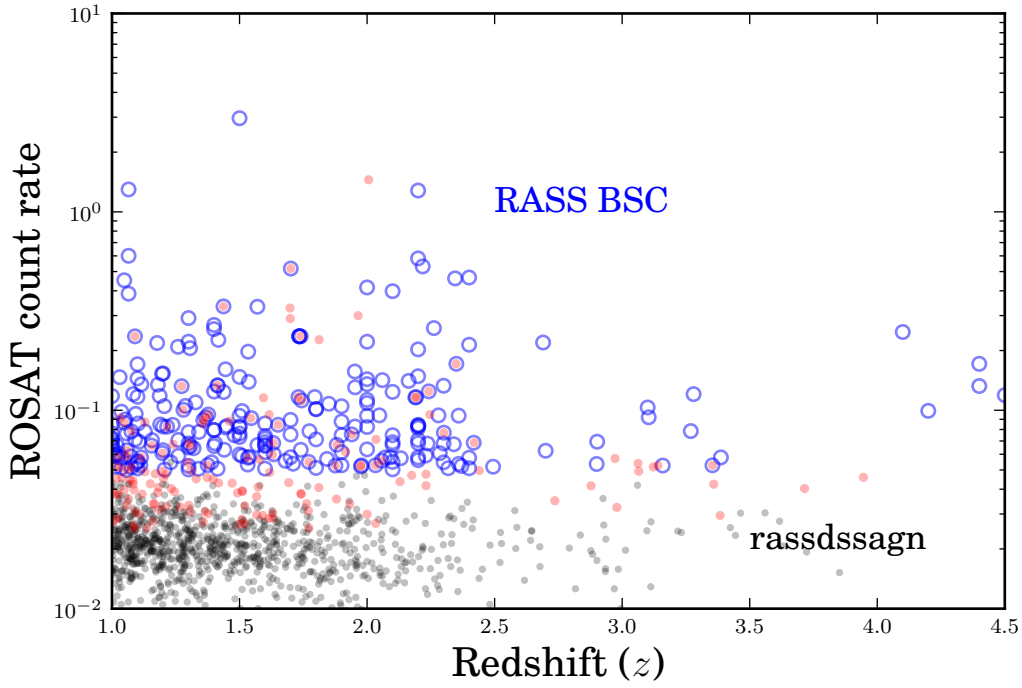

Figure 5.3 The $z > 1$ quasar population as gauged by RASS BSC (*blue open circles*) and *rassdssagn* (*solid circles*) are plotted. The *rassdssagn* objects meeting the flux threshold of 3×10^{-13} erg cm^{-2} s^{-1} are shaded red.

5% of the RASS BSC quasars (248 total) have $z > 1$, but none are sufficient to detect CGM dust. Approximately 15% of the $z > 1$ AGN in *rassdssagn* (156 total) are bright enough to detect IGM dust, but none are sufficient for detecting large CGM dust grains. Overall around 1% of the *total* quasar population, at least 250 objects, are capable of producing X-ray scattering echoes from the diffuse IGM above the level of *Chandra* background.

It is likely that a quasar that has dropped significantly in luminosity will be beyond the threshold of observation, leaving behind a "ghost halo" without a point source. The approximate number of echoes, their observability with respect to other X-ray telescopes, and the potential that one has already been imaged in past surveys will be the subject of future work.

5.2 Dust Scattering Code

The scattering and extinction code used throughout this work is publicly available at **http://github.com/eblur/dust**. It contains modular pieces of code that can easily be switched in or out with different pieces of physics. For example, one can use the same function to calculate the scattering cross-section using either the Rayleigh-Gans or Mie scattering regime. What follows is a rough description of each module, starting from the most basic physics and working up to the higher level calculations. All of the modules require `numpy` as well as a helper module, `constants`. Where indicated, some modules require `scipy.interpolate.interp1d` and other `scipy` math functions.

`cmindex.py`

Every object in this module contains a string describing the model type (`cmtype`) and an `rp` and `ip` that, when given a photon energy as input, return the real and imaginary parts of the complex index of refraction. So far three material types are available: **CmGraphite**, **CmSilicate**, and **CmDrude**. The respective `cmtype` assignments are 'Graphite', 'Silicate', and 'Drude.' The graphite and silicate complex index of refraction for 0.1 μm grain are used, drawn from the tables on Draine's website.[3]

`dust.py`

This module contains objects convenient for describing different grain size distributions. The **Grain** object assumes that all the dust grains have a single size `a` with material density `rho`. **Dustdist** takes an array of grain sizes values (`a`), a power law exponent (`p`), and the material density (`rho`). **Dustspectrum** takes either a **Dustdist** or **Grain** and assigns

[3] http://www.astro.princeton.edu/~draine/dust/dust.diel.html

a mass column `md` and number density `nd` to each `a` value, according to the distribution it was assigned.

In general, **Dustdist** objects are interchangeable with **Grain** objects in other modules that use them. **Dustspectrum** is much more specific and cannot be used as input where a dust distribution type object is expected, and vice versa.

`scatmodels.py`

This module contains objects corresponding to different scattering regimes. Each object must contain a function `Qsca` for calculating scattering cross-sections and `Diff` for calculating the differential scattering cross-section. However some contain additional functions. For example, **RGscat** contains `Char` to calculate the characteristic scattering angle $\tilde{\sigma}$. **Mie** also contains `Qext` to calculate total extinction efficiency and `getQs` as a helper function. The **Mie** module contains a python implementation of the Bohren & Huffman code (*bhmie*, see http://www.astro.princeton.edu/~draine/scattering.html).

The function `Qsca` takes photon energy, grain size, and complex index of refraction as input. The function `Diff` takes angular values in addition to energy, grain size, and complex index of refraction.

Requires: `cmindex`

`sigma_scat.py`

This module contains the bulk of the scattering code, using the various regimes offered in `scatmodels`. The super object **Scatmodel** contains a scattering model object, complex index of refraction object, and strings describing it (`stype` and `ctype`). The remaining objects perform scattering calculations, but are left as objects instead of functions, making

them useful for storing information.

Diffscat stores the differential scattering cross-section `dsig` for a given scattering model `scatm`, energy `E`, single grain size `a`, and angular values `theta` [arcsec]. The object **Sigmascat** stores the scattering efficiency `qsca` and total scattering cross-section `sigma` for any energy `E` and a single grain size `a`, given a scattering model `scatm`. **Sigmaext** does the same, except with the total extinction efficiency `qext`. The objects **Kappascat** and **Kappaext** work similarly, but instead of taking a single grain size they integrate over a **dust.Dustspectrum** object and store `kappa`, the opacity per unit mass column.

This module also contains the helper function `makeScatmodel`, which constructs a **Scatmodel** with the input of a model name ('Mie' or 'RG') and material ('Graphite', 'Silicate' or 'Drude').

Requires: `cmindex`, `dust`, `scatmodels`, `interp1d`

`cosmology.py`

This module contains objects and functions necessary for performing calculations relevant for scattering in a cosmological context. The most important object, **Cosmology**, stores the relevant cosmological parameter values: `h0` in units of km/s/Mpc (75), `m` for Ω_M (0.3), `l` for Ω_Λ (0.7), and `d` for $\Omega_{\rm dust}^{\rm IGM}$ (10^{-5}).

The function `CosmTauX` gives the optical depth to a point source at `z`, given a photon energy, dust distribution, scattering model, and cosmology object. The function `CosmTauScreen` calculates the optical depth of a screen at `zg`, given a photon energy, dust distribution, and scattering model. The helper function `DChi` calculates the distance in co-moving coordinates to an object at `z`.

Requires: `dust`, `sigma_scat`

`halo.py`

This module provides a general framework for storing scattering halos with the **Halo** object. First, the **Halo** should be initialized with an observational energy `E0`, observation angles `alpha` [arcsec], dust distribution `rad` (either a **dust.Dustdist** or **dust.Grain**), and scattering model `scatm`. To calculate the scattering halo, this object should be passed to one of the following functions.

- `UniformIGM` takes a **Halo** object, point source redshift `zs`, and **Cosmology** object `cosm`. It calculates the intensity of scattering from uniformly distributed IGM dust with a constant comoving density (Corrales & Paerels 2012). This function stores relevant information by modifying the **Halo** object properties `intensity` [arcsec^{-2}], optical depth `taux`, dust spectrum `dist`, and halo type `htype`.

- `ScreenIGM` takes a **Halo** object, point source redshift `zs`, redshift of a dusty screen `zg`, mass column for the screen `md`, and a **Cosmology** object `cosm`. It calculates the intensity of scattering from an intergalactic screen of dust, modifying the input **Halo** object's `intensity`, optical depth `taux`, dust spectrum `dist`, and halo type `htype`.

The variable `htype` contained by all **Halo** objects stores supporting information regarding the halo calculation. The **CosmHalo** object introduced in this module is one such example. It contains the `igmtype` string, either 'Uniform' or 'Screen', the relevant **Cosmology**, `zs`, and `zg` values.

Requires: `dust`, `sigma_scat`, `cosmology`

`galhalo.py`

This module is used to calculate scattering halos on Galactic scales using one of the following functions.

- `UniformISM` takes a **Halo** object, hydrogen column `NH`, dust-to-gas mass ratio `d2g`, and calculates the scattering halo from uniformly distributed dust. It stores the resulting **Halo** object's `intensity`, optical depth `taux`, dust spectrum `dist`, and `htype`. This function numerically integrates Equation 1.8 using the trapezoidal method.

- `DiscreteISM` takes a **Halo** object, screen position `xg`, hydrogen column `NH`, and dust-to-gas mass ratio `d2g`. It calculates the scattering halo from an infinitesimally thin screen, modifying the **Halo** object's `intensity`, optical depth `taux`, dust spectrum `dist`, and `htype`. This function numerically integrates Equation 1.8 using the trapezoidal method.

The **GalHalo** object in this module is stored as the **Halo** `htype` whenever scattering is calculated in a Galactic context. It stores `NH`, the screen position `xs`, gas ratio `d2g`, and a string describing the `ismtype` ('Uniform' or 'Screen').

Requires: `dust`, `sigma_scat`, `halo.Halo`, `interp1d`

`halodict.py`

This module contains the **HaloDict** object, which stores halos with their respective energy values as keys. The object is iterable over energy, and can be sliced by specifying a range of energy values in keV.

Requires: `dust`, `sigma_scat`

`analytic.py`

This model computes the scattering halo using the analytic solution for Galactic dust scattering in Section 1.4. The two most important functions do the following.

- `screen_eq` takes a **Halo** object as input and calculates the dust scattering halo from a screen at position `xg`.

- `uniform_eq` takes a **Halo** object as input and calculates the dust scattering halo from uniformly distributed dust.

Requires: `scipy.special`, `dust`, `halo.Halo`, `galhalo`, `halodict`

`model_halo.py`

This module contains specific functions used to simulate the *Chandra* scattering halos in Corrales & Paerels (2013).

- The functions `screen` and `uniform` take a **HaloDict** as input and use `galhalo` functions to numerically integrate the scattering halo.

- The function `simulate_surbri` takes a **HaloDict**, flux values for each energy, effective area, and exposure time in order to compute the surface brightness in units of counts per square pixel.

- The functions `simulate_screen` and `simulate_uniform` use `analytic` functions and `simulate_surbri` to simulate dust scattering halo surface brightness profiles with a few key parameters as input: `a0` and `a1` for minimum and maximum grains sizes, `p` for the power-law slope to the grain size distribution, `NH` for the hydrogen column, `d2g` dust-to-gas mass ratio, and `xg` if using a screen.

Requires: `galhalo`, `halodict`, `analytic`, `interp1d`

`analyze_emcee.py`

This module contains functions specific for analyzing the results of the *emcee* (Foreman-Mackey et al. 2013), which I used to fit the scattering halo of Cygnus X-3 in Chapter 3

Bibliography

Abel, T., Wise, J. H., & Bryan, G. L. 2007, ApJ, 659, L87

Aguirre, A. 1999, ApJ, 525, 583

Anderson, S. F., Margon, B., Voges, W., Plotkin, R. M., Syphers, D., Haggard, D., Collinge, M. J., Meyer, J., Strauss, M. A., Agüeros, M. A., Hall, P. B., Homer, L., Ivezić, Ž., Richards, G. T., Richmond, M. W., Schneider, D. P., Stinson, G., Vanden Berk, D. E., & York, D. G. 2007, AJ, 133, 313

Barsella, B., Ferrini, F., Greenberg, J. M., & Aiello, S. 1989, A&A, 209, 349

Bernstein, J. P., Kessler, R., Kuhlmann, S., Biswas, R., Kovacs, E., Aldering, G., Crane, I., D'Andrea, C. B., Finley, D. A., Frieman, J. A., Hufford, T., Jarvis, M. J., Kim, A. G., Marriner, J., Mukherjee, P., Nichol, R. C., Nugent, P., Parkinson, D., Reis, R. R. R., Sako, M., Spinka, H., & Sullivan, M. 2012, ApJ, 753, 152

Bianchi, S. & Ferrara, A. 2005, MNRAS, 358, 379

Bohlin, R. C., Savage, B. D., & Drake, J. F. 1978, ApJ, 224, 132

Bouché, N., Lehnert, M. D., Aguirre, A., Péroux, C., & Bergeron, J. 2007, MNRAS, 378, 525

Brinkman, A., Parsignault, D., Giacconi, R., Gursky, H., Kellogg, E., Schreier, E., & Tananbaum, H. 1972, IAU Circ., 2446, 1

Bromm, V. & Larson, R. B. 2004, ARA&A, 42, 79

Bromm, V., Yoshida, N., & Hernquist, L. 2003, ApJ, 596, L135

Caffau, E., Bonifacio, P., François, P., Sbordone, L., Monaco, L., Spite, M., Spite, F., Ludwig, H.-G., Cayrel, R., Zaggia, S., Hammer, F., Randich, S., Molaro, P., & Hill, V. 2011, Nature, 477, 67

Corasaniti, P. S. 2006, MNRAS, 372, 191

Corrales, L. & Paerels, F. 2012, ApJ, 751, 93

—. 2013, ArXiv e-prints

Dame, T. M., Hartmann, D., & Thaddeus, P. 2001, ApJ, 547, 792

Davies, J. I., Alton, P., Bianchi, S., & Trewhella, M. 1998a, MNRAS, 300, 1006

—. 1998b, MNRAS, 300, 1006

Davis, J. E. 2001, ApJ, 562, 575

Dickey, J. M. 1983, ApJ, 273, L71

Dijkstra, M. & Loeb, A. 2009, MNRAS, 397, 1976

Draine, B. T. 2003a, ARA&A, 41, 241

—. 2003b, ApJ, 598, 1026

—. 2011, Physics of the Interstellar and Intergalactic Medium, ed. Draine, B. T.

Draine, B. T. & Li, A. 2007, ApJ, 657, 810

Draine, B. T. & Salpeter, E. E. 1979, ApJ, 231, 77

Evans, A., Norwell, G. A., & Bode, M. F. 1985, MNRAS, 213, 1P

Ferrara, A., Ferrini, F., Barsella, B., & Franco, J. 1991a, ApJ, 381, 137

—. 1991b, ApJ, 381, 137

Flesch, E. 2014, http://quasars.org/milliquas.htm

Foreman-Mackey, D., Hogg, D. W., Lang, D., & Goodman, J. 2013, PASP, 125, 306

Fynbo, J. P. U., Ledoux, C., Noterdaeme, P., Christensen, L., Møller, P., Durgapal, A. K., Goldoni, P., Kaper, L., Krogager, J.-K., Laursen, P., Maund, J. R., Milvang-Jensen, B., Okoshi, K., Rasmussen, P. K., Thorsen, T. J., Toft, S., & Zafar, T. 2011, MNRAS, 413, 2481

Gaetz, T. J. 2010, Analysis of the *Chandra* On-Orbit PSF Wings

Gaetz, T. J., Edgar, R. J., Jerius, D. H., Zhao, P., & Smith, R. K. 2004, in Society of Photo-Optical Instrumentation Engineers (SPIE) Conference Series, ed. K. A. Flanagan & O. H. W. Siegmund, Vol. 5165, 411–422

Gierliński, M., Zdziarski, A. A., Poutanen, J., Coppi, P. S., Ebisawa, K., & Johnson, W. N. 1999, MNRAS, 309, 496

Green, J., Schechter, P., Baltay, C., Bean, R., Bennett, D., Brown, R., Conselice, C., Donahue, M., Fan, X., Gaudi, B. S., Hirata, C., Kalirai, J., Lauer, T., Nichol, B., Padmanabhan, N., Perlmutter, S., Rauscher, B., Rhodes, J., Roellig, T., Stern, D., Sumi, T., Tanner, A., Wang, Y., Weinberg, D., Wright, E., Gehrels, N., Sambruna, R., Traub, W., Anderson, J., Cook, K., Garnavich, P., Hillenbrand, L., Ivezic, Z., Kerins, E., Lunine, J., McDonald, P., Penny, M., Phillips, M., Rieke, G., Riess, A., van der Marel, R., Barry, R. K., Cheng, E., Content, D., Cutri, R., Goullioud, R., Grady, K., Helou, G., Jackson, C., Kruk, J., Melton, M., Peddie, C., Rioux, N., & Seiffert, M. 2012, ArXiv e-prints

Green, J., Schechter, P., Baltay, C., Bean, R., Bennett, D., Brown, R., Conselice, C., Donahue, M., Gaudi, S., Lauer, T., Perlmutter, S., Rauscher, B., Rhodes, J., Roellig, T., Stern, D., Sumi, T., Tanner, A., Wang, Y., Wright, E., Gehrels, N., Sambruna, R., & Traub, W. 2011, ArXiv e-prints

Greenberg, J. M., Ferrini, F., Barsella, B., & Aiello, S. 1987a, Nature, 327, 214

—. 1987b, Nature, 327, 214

Güver, T. & Özel, F. 2009, MNRAS, 400, 2050

Hayakawa, S. 1970, Progress of Theoretical Physics, 43, 1224

Heger, A. & Woosley, S. E. 2002, ApJ, 567, 532

Hodges-Kluck, E. & Bregman, J. N. 2014, ApJ, 789, 131

Hosokawa, T., Omukai, K., Yoshida, N., & Yorke, H. W. 2011, Science, 334, 1250

Huenemoerder, D. P., Mitschang, A., Dewey, D., Nowak, M. A., Schulz, N. S., Nichols, J. S., Davis, J. E., Houck, J. C., Marshall, H. L., Noble, M. S., Morgan, D., & Canizares, C. R. 2011, AJ, 141, 129

Inoue, A. K. 2003, PASJ, 55, 901

Inoue, A. K. & Kamaya, H. 2003, MNRAS, 341, L7

Johnson, H. L. 1965, ApJ, 141, 923

Jones, A. P., Tielens, A. G. G. M., & Hollenbach, D. J. 1996, ApJ, 469, 740

Kalberla, P. M. W., Burton, W. B., Hartmann, D., Arnal, E. M., Bajaja, E., Morras, R., & Pöppel, W. G. L. 2005, A&A, 440, 775

Knödlseder, J. 2000, A&A, 360, 539

Knödlseder, J. 2003, in IAU Symposium, Vol. 212, A Massive Star Odyssey: From Main Sequence to Supernova, ed. K. van der Hucht, A. Herrero, & C. Esteban, 505

Konami, S., Matsushita, K., Tsuru, T. G., Gandhi, P., & Tamagawa, T. 2011, ArXiv e-prints

Lanzuisi, G., Ponti, G., Salvato, M., Hasinger, G., Cappelluti, N., Bongiorno, A., Brusa, M., Lusso, E., Nandra, P. K., Merloni, A., Silverman, J., Trump, J., Vignali, C., Comastri, A., Gilli, R., Schramm, M., Steinhardt, C., Sanders, D., Kartaltepe, J., Rosario, D., & Trakhtenbrot, B. 2014, ApJ, 781, 105

Lee, J. C. 2010, Space Sci. Rev., 157, 93

Lee, J. C., Smith, R. K., Canizares, C. R., Costantini, E., de Vries, C., Drake, J., Dwek, E., Edgar, R., Juett, A. M., Li, A., Lisse, C., Paerels, F., Patnaude, D., Ravel, B., Schulz, N. S., Snow, T. P., Valencic, L. A., Wilms, J., & Xiang, J. 2009, in Astronomy, Vol. 2010, astro2010: The Astronomy and Astrophysics Decadal Survey, 178

Ling, Z., Zhang, S. N., & Tang, S. 2009a, ApJ, 695, 1111

Ling, Z., Zhang, S. N., Xiang, J., & Tang, S. 2009b, ApJ, 690, 224

Mao, J., Ling, Z., & Zhang, S.-N. 2014, ApJ, 785, 23

Martin, P. G. 1970, MNRAS, 149, 221

Martini, P. 2004, Coevolution of Black Holes and Galaxies, 169

Mathis, J. S. & Lee, C.-W. 1991, ApJ, 376, 490

Mathis, J. S., Rumpl, W., & Nordsieck, K. H. 1977, ApJ, 217, 425

Mauche, C. W. & Gorenstein, P. 1986, ApJ, 302, 371

McCollough, M. L., Smith, R. K., & Valencic, L. A. 2013, ApJ, 762, 2

Ménard, B. & Fukugita, M. 2012, ApJ, 754, 116

Ménard, B., Kilbinger, M., & Scranton, R. 2010a, MNRAS, 406, 1815

Ménard, B., Nestor, D., Turnshek, D., Quider, A., Richards, G., Chelouche, D., & Rao, S. 2008, MNRAS, 385, 1053

Ménard, B., Scranton, R., Fukugita, M., & Richards, G. 2010b, MNRAS, 405, 1025

—. 2010c, MNRAS, 405, 1025

Ménard, B., Zibetti, S., Nestor, D., & Turnshek, D. 2005, in IAU Colloq. 199: Probing Galaxies through Quasar Absorption Lines, ed. P. Williams, C.-G. Shu, & B. Menard, 86–91

Miralda-Escudé, J. 1999, ApJ, 512, 21

Molster, F. J., Waters, L. B. F. M., & Kemper, F. 2010, in Lecture Notes in Physics, Berlin Springer Verlag, ed. T. Henning, Vol. 815, 143–201

Murray, N., Quataert, E., & Thompson, T. A. 2005, ApJ, 618, 569

Nicolet, B. 1978, A&AS, 34, 1

Novak, G. S., Ostriker, J. P., & Ciotti, L. 2011, ApJ, 737, 26

Ossenkopf, V. & Henning, T. 1994, A&A, 291, 943

Overbeck, J. W. 1965, ApJ, 141, 864

Pagel, B. E. J. 2002, in Astronomical Society of the Pacific Conference Series, Vol. 253, Chemical Enrichment of Intracluster and Intergalactic Medium, ed. R. Fusco-Femiano & F. Matteucci, 489

Peeples, M. S., Werk, J. K., Tumlinson, J., Oppenheimer, B. D., Prochaska, J. X., Katz, N., & Weinberg, D. H. 2014, ApJ, 786, 54

Pei, Y. C. 1992, ApJ, 395, 130

Petric, A., Telis, G. A., Paerels, F., & Helfand, D. J. 2006, ApJ, 651, 41

Pettini, M. 2004, in Cosmochemistry. The melting pot of the elements, ed. C. Esteban, R. García López, A. Herrero, & F. Sánchez , 257–298

Pettini, M. 2006, in The Fabulous Destiny of Galaxies: Bridging Past and Present, ed. V. Le Brun, A. Mazure, S. Arnouts, & D. Burgarella, 319

Predehl, P., Burwitz, V., Paerels, F., & Trümper, J. 2000, A&A, 357, L25

Predehl, P. & Schmitt, J. H. M. M. 1995, A&A, 293, 889

Prochaska, J. X., Wolfe, A. M., Howk, J. C., Gawiser, E., Burles, S. M., & Cooke, J. 2007, ApJS, 171, 29

Rolf, D. P. 1983, Nature, 302, 46

Russeil, D. 2003, A&A, 397, 133

Schlegel, D. J., Finkbeiner, D. P., & Davis, M. 1998, ApJ, 500, 525

Schmidt, G. D., Angel, J. R. P., & Cromwell, R. H. 1976, ApJ, 206, 888

Schneider, R., Ferrara, A., & Salvaterra, R. 2004, MNRAS, 351, 1379

Schneider, R., Omukai, K., Inoue, A. K., & Ferrara, A. 2006, MNRAS, 369, 1437

Smith, R. K. 2008, ApJ, 681, 343

Smith, R. K., Dame, T. M., Costantini, E., & Predehl, P. 2006, ApJ, 648, 452

Smith, R. K. & Dwek, E. 1998, ApJ, 503, 831

Smith, R. K., Edgar, R. J., & Shafer, R. A. 2002, ApJ, 581, 562

Soldi, S., Beckmann, V., Baumgartner, W. H., Ponti, G., Shrader, C. R., Lubiński, P., Krimm, H. A., Mattana, F., & Tueller, J. 2014, A&A, 563, A57

Szostek, A., Zdziarski, A. A., & McCollough, M. L. 2008, MNRAS, 388, 1001

Takahashi, T., Mitsuda, K., Kelley, R., Aharonian, F., Akimoto, F., Allen, S., Anabuki, N., Angelini, L., Arnaud, K., Awaki, H., Bamba, A., Bando, N., Bautz, M., Blandford, R., Boyce, K., Brown, G., Chernyakova, M., Coppi, P., Costantini, E., Cottam, J., Crow, J., de Plaa, J., de Vries, C., den Herder, J.-W., Dipirro, M., Done, C., Dotani, T., Ebisawa, K., Enoto, T., Ezoe, Y., Fabian, A., Fujimoto, R., Fukazawa, Y., Funk, S., Furuzawa,

A., Galeazzi, M., Gandhi, P., Gendreau, K., Gilmore, K., Haba, Y., Hamaguchi, K., Hatsukade, I., Hayashida, K., Hiraga, J., Hirose, K., Hornschemeier, A., Hughes, J., Hwang, U., Iizuka, R., Ishibashi, K., Ishida, M., Ishimura, K., Ishisaki, Y., Isobe, N., Ito, M., Iwata, N., Kaastra, J., Kallman, T., Kamae, T., Katagiri, H., Kataoka, J., Katsuda, S., Kawaharada, M., Kawai, N., Kawasaki, S., Khangaluyan, D., Kilbourne, C., Kinugasa, K., Kitamoto, S., Kitayama, T., Kohmura, T., Kokubun, M., Kosaka, T., Kotani, T., Koyama, K., Kubota, A., Kunieda, H., Laurent, P., Lebrun, F., Limousin, O., Loewenstein, M., Long, K., Madejski, G., Maeda, Y., Makishima, K., Markevitch, M., Matsumoto, H., Matsushita, K., McCammon, D., Miller, J., Mineshige, S., Minesugi, K., Miyazawa, T., Mizuno, T., Mori, K., Mori, H., Mukai, K., Murakami, H., Murakami, T., Mushotzky, R., Nakagawa, Y., Nakagawa, T., Nakajima, H., Nakamori, T., Nakazawa, K., Namba, Y., Nomachi, M., O'Dell, S., Ogawa, H., Ogawa, M., Ogi, K., Ohashi, T., Ohno, M., Ohta, M., Okajima, T., Ota, N., Ozaki, M., Paerels, F., Paltani, S., Parmar, A., Petre, R., Pohl, M., Porter, S., Ramsey, B., Reynolds, C., Sakai, S.-I., Sambruna, R., Sato, G., Sato, Y., Serlemitsos, P., Shida, M., Shimada, T., Shinozaki, K., Shirron, P., Smith, R., Sneiderman, G., Soong, Y., Stawarz, L., Sugita, H., Szymkowiak, A., Tajima, H., Takahashi, H., Takei, Y., Tamagawa, T., Tamura, T., Tamura, K., Tanaka, T., Tanaka, Y., Tanaka, Y., Tashiro, M., Tawara, Y., Terada, Y., Terashima, Y., Tombesi, F., Tomida, H., Tozuka, M., Tsuboi, Y., Tsujimoto, M., Tsunemi, H., Tsuru, T., Uchida, H., Uchiyama, Y., Uchiyama, H., Ueda, Y., Uno, S., Urry, M., Watanabe, S., White, N., Yamada, T., Yamaguchi, H., Yamaoka, K., Yamasaki, N., Yamauchi, M., Yamauchi, S., Yatsu, Y., Yonetoku, D., & Yoshida, A. 2010, in Society of Photo-Optical Instrumentation Engineers (SPIE) Conference Series, Vol. 7732, Society of Photo-Optical Instrumentation Engineers (SPIE) Conference Series

Tiengo, A., Vianello, G., Esposito, P., Mereghetti, S., Giuliani, A., Costantini, E., Israel, G. L., Stella, L., Turolla, R., Zane, S., Rea, N., Götz, D., Bernardini, F., Moretti, A., Romano, P., Ehle, M., & Gehrels, N. 2010, ApJ, 710, 227

Todini, P. & Ferrara, A. 2001, MNRAS, 325, 726

Valencic, L. A. & Smith, R. K. 2008, ApJ, 672, 984

Valencic, L. A., Smith, R. K., Dwek, E., Graessle, D., & Dame, T. M. 2009, ApJ, 692, 502

van de Hulst, H. C. 1957, Light Scattering by Small Particles

Vaughan, S., Willingale, R., Romano, P., Osborne, J. P., Goad, M. R., Beardmore, A. P., Burrows, D. N., Campana, S., Chincarini, G., Covino, S., Moretti, A., O'Brien, P. T., Page, K. L., Supper, M. A., & Tagliaferri, G. 2006, ApJ, 639, 323

Virey, J.-M. & Ealet, A. 2007, A&A, 464, 837

Voges, W., Aschenbach, B., Boller, T., Bräuninger, H., Briel, U., Burkert, W., Dennerl, K., Englhauser, J., Gruber, R., Haberl, F., Hartner, G., Hasinger, G., Kürster, M., Pfeffermann, E., Pietsch, W., Predehl, P., Rosso, C., Schmitt, J. H. M. M., Trümper, J., & Zimmermann, H. U. 1999, A&A, 349, 389

Weingartner, J. C. & Draine, B. T. 2001, ApJ, 548, 296

Whittet, D. C. B. 1992, Dust in the galactic environment

Wilms, J., Allen, A., & McCray, R. 2000, ApJ, 542, 914

Wise, J. H. & Abel, T. 2008, ApJ, 685, 40

Witt, A. N., Smith, R. K., & Dwek, E. 2001, ApJ, 550, L201

Wolfe, A. M., Gawiser, E., & Prochaska, J. X. 2005, ARA&A, 43, 861

Wright, E. L. 1981, ApJ, 250, 1

Xiang, J., Lee, J. C., & Nowak, M. A. 2007, ApJ, 660, 1309

Xiang, J., Lee, J. C., Nowak, M. A., & Wilms, J. 2011, ApJ, 738, 78

Xiang, J., Zhang, S. N., & Yao, Y. 2005, ApJ, 628, 769

Yao, Y., Zhang, S. N., Zhang, X., & Feng, Y. 2003, ApJ, 594, L43

York, D. G., Khare, P., Vanden Berk, D., Kulkarni, V. P., Crotts, A. P. S., Lauroesch, J. T., Richards, G. T., Schneider, D. P., Welty, D. E., Alsayyad, Y., Kumar, A., Lundgren, B., Shanidze, N., Smith, T., Vanlandingham, J., Baugher, B., Hall, P. B., Jenkins, E. B., Menard, B., Rao, S., Tumlinson, J., Turnshek, D., Yip, C.-W., & Brinkmann, J. 2006, MNRAS, 367, 945

Zdziarski, A. A., Misra, R., & Gierliński, M. 2010, MNRAS, 402, 767

Zhang, P. 2008, ApJ, 682, 721

Zu, Y., Weinberg, D. H., Davé, R., Fardal, M., Katz, N., Kereš, D., & Oppenheimer, B. D. 2011, MNRAS, 412, 1059

Zubko, V., Dwek, E., & Arendt, R. G. 2004, ApJS, 152, 211